Oxana Agafonova

A NUMERICAL STUDY OF FOREST INFLUENCES ON THE ATMOSPHERIC BOUNDARY LAYER AND WIND TURBINES

Thesis for the degree of Doctor of Science (Technology) to be presented with due permission for public examination and criticism in the Auditorium 2310 at Lappeenranta University of Technology, Lappeenranta, Finland on the 21st of July, 2017, at noon.

Supervisors   D.Sc., Adj. Prof. Antti Hellsten
              Finnish Meteorological Institute and
              LUT School of Engineering Science
              Lappeenranta University of Technology
              Finland

              D.Sc., Ashvinkumar Chaudhari
              LUT School of Engineering Science
              Lappeenranta University of Technology
              Finland

Reviewers   Ph.D., Assoc. Prof. Johan Meyers
              Faculty of Engineering Science
              Department of Mechanical Engineering
              Katholieke Universiteit Leuven
              Belgium

              Ph.D. Björn Witha
              ForWind - Center for Wind Energy Research
              Carl von Ossietzky Universität Oldenburg
              Germany

Opponent   Ph.D. Antonio Segalini
              Department of Mechanics
              KTH Royal Institute of Technology
              Sweden

Abstract

In the past years, energy consumption in Finland was not fully covered by the energy produced in Finland, and approximately 20% of the total energy consumption was imported. Despite the suitable wind condition, the wind energy production in Finland is very small - only 2.8% of the total demand.

Massive land area (about 72%) in Finland is covered with forest. Therefore, there is a high chance that wind turbines will be installed in forests. It is known that wind behaviour in forests is rather complicated. Therefore, before the arrangement of a wind farm in and above the forest, the investing company has to study the forest influences on the wind-turbine wakes, fatigue and power production.

In the present thesis, Large-Eddy Simulations are carried out using OpenFOAM to investigate the forest-canopy effects on the atmospheric boundary layer and wind turbines. The effects were studied in small (two-turbine) as well as large wind-turbine arrays. For every case, simulations are performed separately for two identical setups, with and without forest. The results of the simulations in the forest case are further compared to the results of the corresponding non-forest case to clearly show the changes in the wake and turbulence structure due to the forest. Moreover, the actual mechanical shaft power produced by each turbine in the small wind-turbine array and by a single turbine in the large array is calculated for the forest and non-forest cases. Aerodynamic efficiency and power losses due to forest are discussed as well. It is found that the loss of actual power due to forest amounts to nearly 20%. The blade angle of attack is studied for cases with and without forest. It is found that a non-optimal angle of attack in the forest case is responsible for the power loss. Therefore, an active pitch control is proposed in order to reduce the loss of actual power in the forest.

Keywords: ABL, ALM, forest, LES, OpenFOAM, pitch control, turbulence, wind flow, wind power, wind turbine wake

Acknowledgements

Oxana Agafonova

July 2017 Lappeenranta,
Finland

Contents

List of publications

Present thesis contains material from the papers listed below.

Publication I
Agafonova, O., Avramenko, A., Chaudhari, A., and Hellsten, A. (2016). The effects of the canopy created velocity inflection in the wake development. *AIP Conference Proceedings*, 1738(1), pp. 480082-1 - 480082-4.

Publication II
Agafonova, O., Avramenko, A., Chaudhari, A., and Hellsten, A. (2016). Effects of the canopy created velocity inflection in the wake development in a large wind turbine array. *Journal of Physics: Conference Series*, 753(3), pp. 032001

O. Agafonova is the principal author and investigator in papers I and II. In both papers, M.Sc. O. Agafonova was the corresponding author, performed all the numerical simulations, and wrote the majority of the text. M.Sc. A. Avramenko helped in the pre- and post-processing of the simulations. D.Sc. A. Chaudhari and D.Sc. A. Hellsten were responsible for the supervising of the work.

Nomenclature

Abbreviations

ABL	Atmospheric Boundary Layer
ADM	Actuator Disk Method
ADM-A	Advanced Actuator Disk Method (by E. Svenning, 2010)
ALM	Actuator Line Method
BEM	Blade Element Momentum Approach
CFD	Computational Fluid Dynamics
CFL	Courant-Friedrichs-Levy number
DNS	Direct Numerical Simulation
EU	European Union
FVM	Finite Volume Method
GW	Giga Watt
IEC	International Electrotechnical Commission
LAD	Leaf-Area Density
LAI	Leaf-Area Index
LES	Large-Eddy Simulation
MW	Mega Watt
NREL	National Renewable Energy Laboratory, United States

OpenFOAM	Open source Field Operation And Manipulation
PDF	Probability Density Function
PISO	Pressure-Implicit with Splitting of Operators
RANS	Reynolds-Averaged Navier-Stokes
RK	Runge-Kutta
RMS	Root Mean Square
SGS	Sub-Grid Scale
SOWFA	Simulator fOr Wind Farm Applications
TKE	Turbulence Kinetic Energy
WSS	Wall Shear Stress
WT	Wind Turbine

Greek Letters

α	Angle of attack
α_f	Local Foliage Density (LAD)
β_t	Domain turning angle (the direction is relative to x)
Δ	Cubic root of the volume
Δt	Time step
$\Delta \dot{m}$	Deficit of mass flow
ΔE	Deficit of energy
ΔP	Deficit of power
$\Delta x, \Delta y, \Delta z$	Grid spacing in x-, y-, z-directions
ϵ	Turbulent energy dissipation
ε	Smearing parameter

η_ε	Regularization kernel
θ	Azimuthal angle (azimuth)
γ	Collective angle
κ	von Kármán constant
λ	Tip-speed ratio
μ	Dynamic viscosity
μ_{eff}	Effective dynamic viscosity
ν	Kinematic molecular viscosity
ν_{sgs}	Kinematic SGS viscosity
ρ	Density
τ	Time-scale for the canopy-drag
τ_w	Wall shear stress
τ_{ij}	SGS stress tensor
ϕ	Flow angle
φ	Local mounting pitch angle
	Design twist angle
ω	Rotor speed
Ω	Angular velocity

Symbols

c	Chord length
C_d^F	Canopy-drag constant
C_k and C_ϵ	Sub-Grid Scale model constants
C_T	Thrust coefficient
C_P	Power coefficient
C_d	Drag coefficient
C_l	Lift coefficient
d	Height of the computational domain, depth of the boundary layer
D	Diameter of wind turbine
DU	Deficit of mean windwise velocity
DI	Excess of windwise turbulence intensity
dx, dy, dz	Grid spacing in x, y, z-directions
E_x	Spectral energy density
f	External body force
F	LAI
Fl	Flatness (kurtosis)
f^F	Forest-canopy sink term (canopy-drag force)
f^T	Aerodynamic (turbine) force
g	Driving force
I	Turbulence Intensity
I^{loc}	Local turbulence Intensity
h	Forest-canopy height
H	Turbine hub-height
k	Turbulent kinetic energy
k_{sgs}	Sub-grid scale turbulent kinetic energy
k_x	Wave number
L	Lift force
L_x, L_y, L_z	Length of computational domain in x, y, z-directions
Lu	Integral length scale
N_x, N_y, N_z	Number of computational cells in x, y, z-directions

$\tilde{p}$	Resolved instantaneous pressure
P_{actual}	Actual mechanical shaft power
P_{avail}	Available wind power
R	Radius of wind turbine
Re	Reynolds number
Re_τ	Frictional Reynolds number
Re_D	Reynolds number based on turbine diameter
Ruu	Windwise correlation function of velocity fluctuations
$\tilde{S}_{ij}$	Strain-rate tensor
Sk	Skewness
t	Time
$\tilde{u}_i$	Resolved instantaneous velocity
u'	Resolved velocity fluctuation
u_τ, u_*, u_{*0}	Frictional velocity
U	Resolved Mean velocity (windwise component)
U_∞	Free-stream velocity
U_h	Hub-height velocity
U_{ref}	Reference mean velocity
$Urms$	Root-mean-square velocity
V	Volume
V_{rel}	Local velocity relative to the rotating blade
x, y, z	Cartesian coordinates, z is the vertical coordinate
r, θ, z	Polar coordinate system, r is the radial, θ - azimuthal and z - axial components
z_0	Roughness length
z_{agl}	Height above ground level

Chapter 1

Introduction

1.1 Motivation

In Finland, development of less energy-consuming technology as well as global warming are increasing, and therefore the need for energy eventually began to decrease slightly. For example, by the end of 2015, electricity consumption in Finland decreased by 3% in comparison to the previous year (2014) and reached 82.5 TWh. Despite that, net import of energy is still very high; it is equal to 19.8% of the total energy consumption. Finland is looking for new sources of energy. Renewable energy would be a good solution to produce energy without polluting the air or exhausting fuel reserves. In the year 2015, renewable energy production was 45% of the total energy production in Finland.
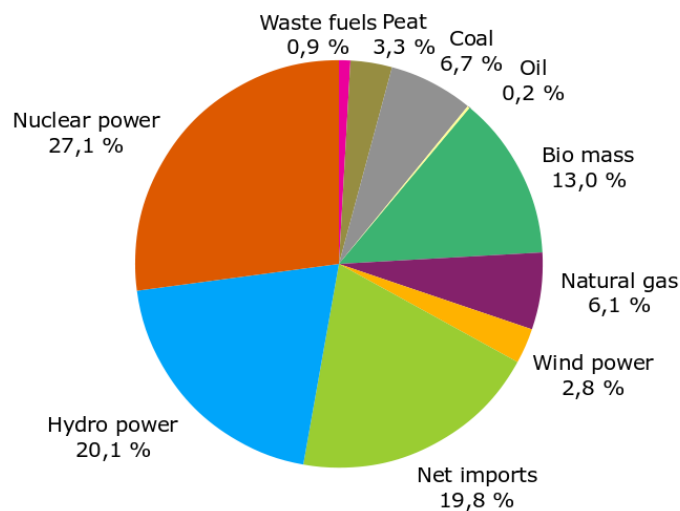
Figure 1.1.1: Electricity supply by energy sources for the year 2015, Finnish Energy Report (2016).

Among other renewable energy sources, wind energy covered 2.8% of the total Finnish electricity consumption in 2015 year, according to Figure 1.1.1 (Finnish Energy Report, 2016). Wind power has been already used for many generations, and the technology is continuously developing. Wind-farm arrangements are challenging in Finland; but at the same time, weather conditions are such that it is almost constantly windy in Finland, especially in areas close to the coast. Nowadays, wind-power capacity in Finland is 1005 MW, which is obtained by approximately 387 wind turbines. Among other goals, the present research work aims at helping to increase wind energy production. The Finnish government set the goal for the wind energy industry to increase their production by 2020. The target is 6 TWh per year, equivalent to 2500 MW. By that time, the wind power can cover approximately 7% of the electricity demand (Ministry of Foreign Affairs of Denmark, 2014).

In Finland, 72% of the land area is covered with forest, and the forest areas often include hills and lakes. There are not many options for where to install wind turbines. On one hand, the wind farm should be located close enough to the cities in order to lower the costs of transfer, maintenance and grid connection. On the other hand, locations far enough from human habitation would be preferable in order to avoid disturbances such as noise and shadow flicker. Thus, the chance that wind turbines will be placed in forest is very high. Wind behaviour in the forest and over the complex terrain is extremely complicated. See Figure 1.1.2.

Therefore, the investing company needs to investigate wind conditions as well as wind turbine wake behaviour in the real wind park site (possibly including forest and complex terrain) before the construction of the wind-farm is started. It can be made using field measurements and/or numerical simulations. Field measurements can be very expensive and time-consuming. On the contrary, numerical simulations can be relatively affordable. However, at first it is necessary to validate numerical simulations (e.g., via a wind-tunnel experiment on a small-scale) in order to perform them further on a real scale. Nevertheless, many wind-energy companies do not yet trust the still developing but very promising Computational Fluid Dynamics (CFD) simulations.

There are certain well-known issues about wind turbines located in the forested area. For example, the Atmospheric Boundary Layer (ABL) wind profile starts recovering above three heights of the forest canopy (Kaimal and Finnigan, 1994), and turbine wake recovers faster downstream above the forest (Odemark and Segalini, 2014). Wind conditions above the forest have strong wind shear and increased turbulence levels, which can lead to increased fatigue and shorter turbine life cycle (Nebenführ and Davidson, 2014). A few wind tunnel studies were performed in order to better analyse how the canopy affects the wind energy production (Odemark and Segalini, 2014; Barlas et al., 2016). Nevertheless, it has never been a subject of deep numerical analysis of turbine wake changes due to the forest-created effects.
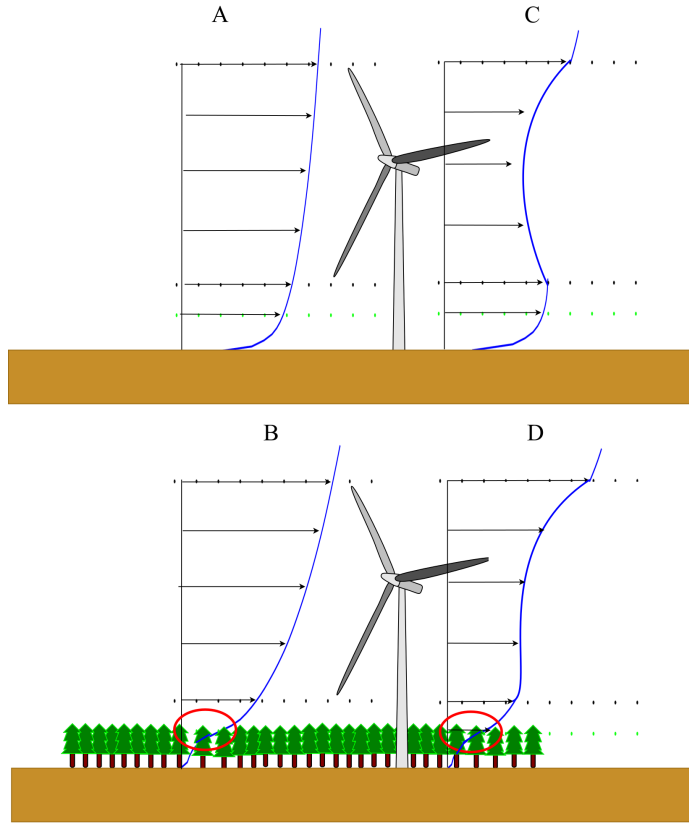
Figure 1.1.2: Wind behaviour in the flat terrain without forest (A); in and above forest (B); behind the wind turbine located in unforested field (C); and above the forest (D).

1.2 Literature review

Turbulence in and above forest canopy has been studied by many field measurements (Allen, 1968; Finnigan, 1979; Baldocchi and Meyers, 1988; Kaimal and Finnigan, 1994; Launiainen et al., 2007; Dupont and Patton, 2012). Many wind tunnel studies are also conducted on forest with respect to wind energy (Raupach et al., 1986; Brunet et al., 1994; Agafonova, 2011; Agafonova et al., 2012; Odemark and Segalini, 2014). Since 1990 it became popular to study the ABL in/above canopy using numerical modelling (Shaw and Schumann, 1992; Kanda and Hino, 1994; Shaw and Patton, 2003; Dupont and Brunet, 2008a, 2009; Agafonova, 2011; Agafonova et al., 2012; Bailey and Stoll, 2013; Nebenführ and Davidson, 2014). Shaw and Schumann (1992) performed several Large Eddy Simulations (LES) in the short computational domain under weakly unstable condition. The height of the computational domain was equal to three forest-canopy heights. The forest was represented by a momentum sink and a heat source, which are included

in the momentum and energy equations, respectively. The Leaf-Area density (LAD) was chosen to represent a deciduous forest with a relatively open trunk space. The similar shape of LAD but with different Leaf-Area Indices (LAI) of 2 and 5, was used in the separate simulations. Obtained mean windwise velocity profiles have similar shape as the measured wind profiles. Moreover, the so-called coupling ratio (the ratio of the wind inside the forest to the wind above the forest) was calculated. The values are approximately 0.16 (in the case with LAI =5) and 0.26 (LAI=2), which correspond to the values listed by Cionco (1979) for coniferous and winter deciduous forests, respectively. The skewness of the windwise velocity component is positive inside and negative above the forest. By contrast, the vertical velocity skewness is negative inside and positive above the forest. It was found that the windwise and vertical velocities are skewed similarly as in the field but with larger magnitude inside the forest. The overestimation of the skewness magnitudes can be due to the very short and shallow computational domain.

The above-mentioned studies were related mostly to forest effects on ABL, but some of them also describe possible effects on the wind energy production and possible fatigue loads without any turbine model present (Nebenführ and Davidson, 2014). Nebenführ and Davidson (2014) performed two LES simulations with and without forest to find the effects of the forest on neutral ABL. The forest canopy was modelled by adding the forest sink term to the momentum equation similarly to Shaw and Schumann (1992). The leaf area density profile was generated using the empirical model of Lalic and Mihailovic (2004) for pine forest. The leaf area index was equal to 4.3. The results of the simulation with the forest were compared with the field measurements (Bergström et al., 2013). The obtained results, such as horizontal wind speed and the vertical shear stress, are in a good agreement with the measurements. However, the crosswind and vertical normal stresses are underestimated but the windwise component is overestimated. The vertical wind shear (or wind shear exponent as a change of wind speed or direction with change of altitude) is found to be 0.19 and 0.52 at the hub-height location of the virtual wind turbine in the cases without and with the forest, respectively. Except for the increased wind shear, the increased turbulence intensity is also induced by the forest. The windwise and vertical components are equal to 19.9% and 11.6% in the forest case, respectively. Moreover, the skewness and flatness were also analysed in cases with and without forest. They show a strong possibility of the existence of discontinuous extreme fluctuations in the flow over the forest.

At the same time, the turbine wake development on the flat and complex terrain without forest canopy has been studied numerically and experimentally. At first, the flow over an isolated wind turbine located on flat terrain was studied experimentally by Vermeer et al. (2003); Chamorro and Porté-Agel (2010), and numerically by Sørensen and Kock (1995); Vermeer et al. (2003); Wu and Porté-Agel (2011) and Yang et al. (2014). Chamorro and Porté-Agel (2010) conducted the experiment with a small wind turbine placed in the boundary-layer flow under neutral and stably stratified conditions. Temperature and instantaneous windwise and vertical velocity components were obtained with hight resolution at different locations behind the wind turbine. The mean and turbulent

characteristics of the flow were calculated. It was found that the wake behind the turbine continues until 20 turbine diameters. The windwise velocity deficit in the wake region has an almost axisymmetric shape, and the maximum deficit is located near the centreline. However, the turbulence intensity does not have axisymmetric behaviour. The maximum values of the turbulence intensity are located in the area above the hub height. A detailed description of the obtained results is given in Wu and Porté-Agel (2011). Moreover, the LES with two different turbine models as ADM and rotating ADM are performed and compared with the experiment by Wu and Porté-Agel (2011). The LES with the rotating ADM accurately predicts the mean and turbulent statistics of the flow. Later on, several turbines in a row were considered (Churchfield et al., 2012c; Yang et al., 2014). Yang et al. (2014) carried out LES with ALM for the flow over a single wind turbine, a turbine array and operational utility-scale wind farm. Three different grid resolutions are considered. The results of the simulation over the single turbine were compared with the wind-tunnel measurements by Chamorro and Porté-Agel (2010). The LES with blade treated as NACA0012 airfoil significantly underpredicts the windwise velocity deficit in the wake region. Better agreement was obtained using flat-plate airfoil properties and applying nacelle and tower models. No significant differences were found between the results obtained on the different grids.

Furthermore, the studies of wind flow were continued on large wind turbine arrays (Chamorro and Porté-Agel, 2011; Wu and Porté-Agel, 2013; Witha et al., 2014; Allaerts and Meyers, 2015; Munters et al., 2016). Munters et al. (2016) proposed so-called shifted periodic boundary conditions as an alternative to normal periodic conditions. They performed several LESs using shifted and non-shifted periodic conditions over a half-channel with a large Reynolds number. The correlation function obtained in the cases with shifted periodic conditions decreases to zero value already when the streamwise length of the domain is equal to $L_x = 2\pi d$, where d is height of the domain. However, in cases with normal periodic conditions, the correlation function almost reaches zero value at $L_x = 6\pi d$ and completely achieves zero only when $L_x \geq 12\pi d$. Thus, the proposed methodology is helpful in providing fully developed turbulent channel flow in a shorter domain and with less computational cost. It was concluded that the coherent turbulent structures obtained by shifted periodic conditions have the same autocorrelation behaviour as the ones observed in much larger domains. Moreover, LES over wind turbine array using inflow conditions from precursor simulations with shifted and non-shifted periodic conditions were carried out. The velocity and power distribution between the turbines in the arrays in the case with shifted precursor simulation is much more uniform than it is in the case with non-shifted precursor periodic conditions.

Later on, papers devoted to the study of turbine wake development in real complex terrains were published by Porté-Agel et al. (2011) and Yang et al. (2014). Then studies related to the effect of surface roughness length z_0 on the wake development were published (Churchfield et al., 2012c; Wu and Porté-Agel, 2012).

Very recently, a couple of studies have been carried out to understand the relation be-

tween forest (or other roughness canopy) and wind energy. Odemark and Segalini (2014) performed a small-scale wind-tunnel investigation of the effects of a high surface boundary layer roughness (canopy) on the outputs of a wind turbine. A small increase (3%) in maximum power output was found in a case with the forest in comparison to the case without forest. At the same time, the standard deviation of the thrust coefficient and the tip-speed ratio was found to increase linearly with increasing turbulence intensity and to increase with decreasing turbine hub height above the forest. Barlas et al. (2016) conducted wind-tunnel measurements of the flow and turbulence characteristics and spectral content downstream a wind turbine under two different boundary-layer inflow conditions (moderately rough and smooth). In the case of high roughness inflow the wake recovers earlier than in the case of smooth roughness inflow because of the high incoming turbulence. It was found to be an advantage in the power production for the downstream turbines, but also a disadvantage in a shortened fatigue-life time because of an earlier failure of the wind turbine parts.

A few LES studies (Agafonova et al., 2016a,b; Schröttle et al., 2016) are found to be devoted to the impact of forest on wind turbine wake. At first, Agafonova et al. (2016a) studied the effects of forest canopy to the wake development of a single wind turbine as well as two wind turbines in tandem. The turbine is modelled by an actuator line model. The simulations were performed on the real scale with and without forest canopy. However, the obtained results in the case of a single turbine without forest were compared to the small-scale wind-tunnel measurements (Chamorro and Porté-Agel (2010)). Most probably, the results affected by the scaling and therefore the magnitude of the velocity is strongly underestimated in the near-wake region. At the same time, the results agree well enough in the far-wake regions. Next, the effects of the forest on the wind turbine wake development were found due to the comparison between the two-wind-turbines cases with and without forest. The wake in the forest case was found to be shorter windwise but wider in the crosswind and vertical directions.

Later, Agafonova et al. (2016b) studied the influence of forest on the wakes and power production of a large wind turbine array. Faster wake recovery was noticed in the large wind turbine array in the forest case than in the non-forest case. The turbulence intensity and wind shear reported in the paper are higher in the forest than in the non-forest case. In the forest case they consist of 26% and 0.53, respectively. Wind power produced in the forest case was found to be rather small in comparison to the unforested case with similar velocity at hub height. However, the power coefficient was found to be approximately 5% larger in the forest than in the non-forest case.

Lately, one LES study about the forest effects on the turbine wake by Schröttle et al. (2016) was found. They discovered wake of a single wind turbine affected by forest. The turbine is modelled by a simple actuator disk model. An earlier wake recovery in the case of forest was also found.

Therefore, based on the lack of the available literature related to the numerical study

of forest effects on the turbine behaviour and on the turbine output, the major question, addressed in the present thesis, is the detailed understanding of forest influence on the real-scale wind fields in which the wind turbines are exposed to.

1.3 Objectives of the thesis

The main objectives of the thesis are:

- to find the effects of the forest on the wind flow at possible turbine locations. This is done via analysing the mean wind flow, turbulence intensity, wind shear and turbulence statistics (length scale, skewness, flatness and so on) with and without forest;

- to find the forest-induced velocity inflection in the far-wake flow, where a downstream turbine could be located. This is studied with the help of power efficiency;

- to find the forest effects on the turbine-generated near-wake flow (using, for example, power prediction and angle of attack). Active pitch control for the turbines located in and/or above the forest is also proposed to get more power production.

The present thesis is focused on the research and development of the numerical methodology further applied for wind-flow simulation above the forest and past wind turbines. LES, LAD approaches and ALM are implemented and coupled in the freely available open-source CFD software OpenFOAM. The proposed methodology can be further used in the simulation of real (large) on-shore wind farms located on a complex terrain. Moreover, the output of the simulation can be helpful in the arrangement of a future wind park, e.g. in the selection of possible wind-park sites and further in the optimal location of wind turbines or in the maintenance of an already existing wind farm. Likewise, already obtained results can be used in order to design the wind turbine which is more suitable for operating in cold-climate weather and in forest.

In order to achieve the goal, the following intermediate objectives were solved:

- adoption of the forest-canopy model and validation with the results obtained by Shaw and Schumann (1992), studying the influence of forest on both mean flow and turbulence without Wind Turbine (WT);

- validation of the turbine model (NREL SOWFA) with the corresponding wind-tunnel experimental data for an isolated WT without forest,

- simulation of the case with two wind turbines in tandem (without forest) and comparison between the results obtained for a single WT and a downwind WT (in 2 WTs case);

- simulation of the flow for two wind turbines with and without forest, comparison between the results, investigating how forest affects the wind turbine wake;

- simulations of the flow in a large wind turbine array (3×2 WTs) with and without forest, comparison between the obtained results, investigating the effects created by forest.

1.4   Structure of the thesis

The present thesis is organised as follows.

In Chapter 2, the governing equations, the numerical methods and schemes and boundary conditions are described.

In Chapter 3, the forest-canopy model is described and validated using the field measurements and results of similar LES with the same model. The effects of the canopy on the ABL are discussed.

In Chapter 4, the existing turbine models are briefly described and qualitatively compared. A model (ALM) that suits better for solving the present research goals is chosen, described in detail and validated via the wind-tunnel experimental data. The results of the simulations for an isolated WT and two WT in tandem are discussed.

In Chapter 5, the forest-canopy and turbine models are combined. The results of the simulations for two wind turbines in tandem as well as a large wind turbine array with and without forest are discussed and compared to each other and other available results of similar cases. An active pitch control is proposed in order to increase power production in forest.

In Chapter 6, the summary of the thesis is given.

Chapter 2

LES modelling

2.1 Governing equations

The governing equations which describe the incompressible fluid motion are Navier-Stokes and continuity equations (in tensor notation):

$$\frac{\partial u_i}{\partial t} + u_j \frac{\partial u_i}{\partial x_j} = -\frac{1}{\rho}\frac{\partial p}{\partial x_i} + \nu \frac{\partial^2}{\partial x_i x_j} u_i + f_i + g_i, \qquad (2.1.1)$$

$$\frac{\partial u_i}{\partial x_i} = 0, \qquad (2.1.2)$$

where u_i are velocity components, x_i are spatial coordinates, t is time, p is pressure, ρ and ν are the fluids density and kinematic viscosity, respectively, f_i is the external body force, and in this context it includes the aerodynamic turbine force f_i^T and forest canopy sink term f_i^F, and g_i (driving force) is the force used to drive the periodic flow (see below for details). Both f_i^T and f_i^F are further defined in Chapter 4 and Chapter 3, respectively. Coriolis force is not considered in the present study because its neglecting in the flow under thermally neutral conditions is not sufficient for the present research question.

In CFD, the discretized governing equations are solved numerically on the computational finite volume (difference) grid. The discretized equations can be directly numerically solved, but in order to obtain a sufficiently accurate solution, the resolution of the computational grid must be sufficiently high to resolve the smallest scales of the turbulent flow. Thus, the main disadvantage of the Direct Numerical Simulations (DNS) is that it requires too much computational time. Reynolds averaging and grid filtering are approaches which reduce the complexity of the problem and therefore the computational time.

A grid filtering approach, based on the assumption that the large scales of turbulence are the most influential and the smallest scales are universal and can be modelled, is called Large Eddy Simulation (LES). Thus, LES directly resolves the turbulent structures larger than the grid size, but at the same time models the turbulent structures smaller than the grid size. LES has been compared with the DNS and Reynolds Averaging Navier-Stokes

(RANS) approaches many times (see Germano et al. (1991); Wilcox (2006); Agafonova et al. (2014a,b); Chaudhari (2014)). It predicts the real-scale wind flow more accurately than RANS and the wind-tunnel-scale wind flow almost as accurately as DNS (according to Germano et al. (1991); Wilcox (2006); Agafonova et al. (2014a,b); Chaudhari (2014)). Moreover, the real-scale time- and space-resolved turbulence wind-flow data, which is the subject of interest in the present thesis, can not be predicted by RANS or DNS. Therefore, the LES approach is chosen to perform the numerical simulations in the present study. The LES equations take the form:

$$\frac{\partial \widetilde{u}_i}{\partial t} + \frac{\partial}{\partial x_j}\left(\widetilde{u}_i\widetilde{u}_j\right) = -\frac{1}{\rho}\frac{\partial \widetilde{p}}{\partial x_i} + \nu\frac{\partial}{\partial x_j}\left(\frac{\partial \widetilde{u}_i}{\partial x_j} + \frac{\partial \widetilde{u}_j}{\partial x_i}\right) - \frac{\partial \tau_{ij}}{\partial x_j} + f_i + g_i, \qquad (2.1.3)$$

$$\frac{\partial \widetilde{u}_i}{\partial x_i} = 0 \qquad (2.1.4)$$

where ($\widetilde{*}$) represents filtered values and τ_{ij} is the sub-grid stress tensor defined as $\tau_{ij} = \widetilde{u_iu_j} - \widetilde{u}_i\widetilde{u}_j$. However, τ cannot be computed directly; therefore a Sub-Grid Scale stress model (SGS) is needed.

2.2   Sub-Grid Scale LES model

The first Sub-Grid Scale (SGS) LES model (Smagorinsky, 1963) is based on applying the local grid spacing as the length scale. Later, the dynamic SGS eddy-viscosity model was proposed by Germano et al. (1991). But the last-mentioned model can have numerical stability problems. However, it could be stabilized using an additional trick (for example, averaging the flow variables in the solution), according to Müller and Davidson (2000) and Nilsen (2014). Therefore, a one-equation eddy-viscosity model is used in the present study. The transport equation for sub-grid kinetic energy ($k_{sgs} = \tau_{ii}/2$) must be solved together with the filtered momentum equation (2.1.1). The transport equation solved in OpenFOAM is (Yoshizawa, 1985; de Villiers, 2006; Nilsen, 2014) :

$$\frac{\partial k_{sgs}}{\partial t} + \frac{\partial \widetilde{u}_j k_{sgs}}{\partial x_j} = -\tau_{ij}\widetilde{S}_{ij} - \epsilon + \frac{\partial}{\partial x_j}\left((\nu + \nu_{sgs})\frac{\partial k_{sgs}}{\partial x_j}\right), \qquad (2.2.1)$$

where $\widetilde{S}_{ij}$ is the strain-rate tensor of the resolved scales, ν_{sgs} represents the eddy viscosity as follows:

$$\nu_{sgs} = C_k k_{sgs}^{1/2}\Delta, \qquad (2.2.2)$$

and ϵ is the turbulent energy dissipation, and it is modelled as:

$$\epsilon = C_\epsilon \frac{k_{sgs}^{3/2}}{\Delta}, \qquad (2.2.3)$$

where $C_k = 0.094$ and $C_\epsilon = 1.048$ are the turbulent kinetic energy and dissipation model constants, respectively, and Δ is the cubic root of the volume of the (local) computational cell.

2.3 Numerical methods

As mentioned in Chapter 1, the filtered governing equations were solved using Open-FOAM (OpenCFD Ltd (ESI Group), 2004-2017; de Villiers, 2006) with the standard PISO (Pressure Implicit with Splitting of Operators, (Issa, 1986)) and RK4Projection (Runge-Kutta 4th-order Projection (Vuorinen et al., 2012)) solvers. The OpenFOAM code written in C++ is based on the finite volume method with co-located numerical grid and standard Gaussian finite volume integration (de Villiers, 2006; Nilsen, 2014). Gauss-integration is a method of volume integral calculation which involves the Gauss theorem, and therefore, transforms a volume integral into a surface integral.
The pisoFoam solver uses the implicit second-order backward in time scheme for the velocity solution.

The RK4ProjectionFoam solver, which was first implemented in OpenFOAM by Vuorinen et al. (2012), uses the fourth order Runge-Kutta time integration scheme. The Runge-Kutta steps are:

- calculation of $\widetilde{u}_i^{*,(n+1)}$ from the momentum equation (2.1.1) for $\widetilde{u}_i^{(n)}$ without the pressure gradient term $\partial \widetilde{p}^{(n+1)}/\partial x_i$;

- solution of the Poisson equation:

$$\frac{\partial}{\partial x_i}\frac{\partial \widetilde{p}^{(n+1)}}{\partial x_i} = \rho/\Delta t\frac{\partial \widetilde{u}_i^{*,(n+1)}}{\partial x_i};\tag{2.3.1}$$

- and then the velocity field $\widetilde{u}_i^*$ is corrected using the pressure gradient $\partial \widetilde{p}^{(n+1)}/\partial x_i$, as result of solution of the Poisson equation (2.3.1), as following:

$$\widetilde{u}_i^{(n+1)} = \widetilde{u}_i^{*,(n+1)} - \Delta t\frac{\partial \widetilde{p}^{(n+1)}}{\partial x_i}, \; n = 0, 1, 2, 3.\tag{2.3.2}$$

The above-mentioned steps must be repeated four times. Earlier, several studies were performed to demonstrate the excellent results for the inviscid Taylor-Green vortex, the 2D lid-driven cavity flow, channel flow and wind flow over Bolund Hill (Vuorinen et al., 2012, 2014; Chaudhari et al., 2014b; Chaudhari, 2014).

In order to compare the implementation of RK4ProjectionFoam with pisoFoam solver in the case with turbine, two simulations with identical setups were performed on an 8 m resolution grid. As one can see from Figure 2.3.1, both solvers give identical results. At the same time, the identical setups were made for the forest case. The results of the simulations in the forest case (presented in Figure 2.3.2) differ, but not significantly. Hence, both solvers were used in the present study.

The convective term was discretized based on Gauss-integration, using the (volumetric) flux of velocity and the advected velocity field being linearly interpolated to the cell faces.
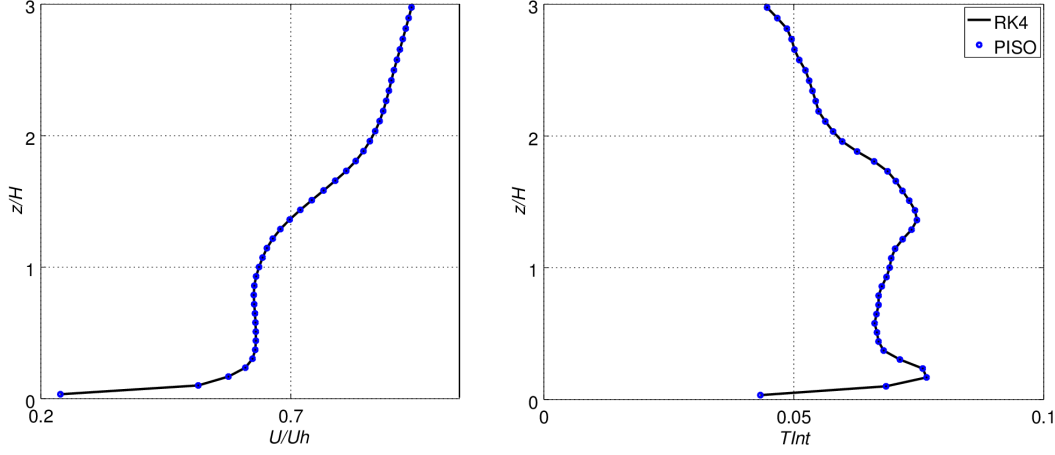
Figure 2.3.1: Normalized mean windwise velocity and turbulence intensity predictions obtained by the RK4ProjectionFoam and pisoFoam for a case with wind turbine and without forest.

Thus, the convection scheme was central differencing which is unbounded and the second-order accurate even on unstructured meshes. In order to ensure stability (when using an unbounded central differencing convection scheme) the Courant-Friedrichs-Lewy (CFL) condition should be satisfied. That is, the maximum Courant number in the entire domain should not exceed one (usually in the range 0.5 - 0.8) (de Villiers, 2006). And thus, the time-step size Δt has to be not greater than the product of $\Delta x / \widetilde{u}_i$ and the chosen Courant number. This rule is applied only for the flow that is undisturbed by the turbine and/or forest. However, in the case with turbine or forest, an additional condition is applied. For details, see Chapter 4 or Chapter 3, respectively. The diffusion term was also discretized using a Gauss-integration based scheme which requires a selection of both an interpolation scheme for the diffusion coefficient and a surface normal gradient scheme (because the diffusion term is bounded on an orthogonal mesh). Therefore for every simulation, the spatial schemes (both convective and diffusion) for the velocity field calculations were second-order accurate.

2.4 Boundary conditions

2.4.1 Inlet-outlet

Two different inlet-outlet conditions were used in the present study. In order to simulate the flow throughout the large wind turbine array, the periodic inlet-outlet was used. In order to perform the simulation with the periodic inlet-outlet conditions, the driving force g should be set to a certain non-zero value. In the present study, in the case of flat terrain without turbine and forest, the flow was driven by a volume force $\vec{g} = (g\cos(\beta_t), g\sin(\beta_t), 0)$, where $g = u_\tau^2/d$, d is the depth of the boundary layer (is equal to
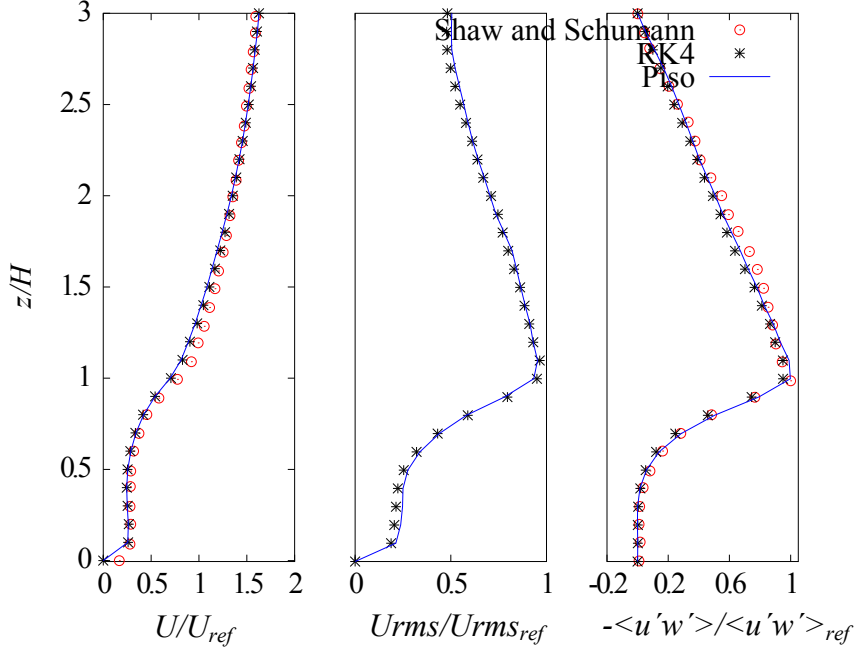
Figure 2.3.2: Normalized mean windwise velocity, root-mean square velocity and vertical Reynolds shear stress predictions obtained by the RK4ProjectionFoam and pisoFoam for a case with forest and without turbine, compared to the study by Shaw and Schumann (1992).

the height of the domain in the present study), u_τ is the frictional velocity, and β_t is the angle between the windwise direction and the x axis.

However, for the flow with a stand-alone turbine or two wind turbines, the so-called mapping technique (or recycling technique (Baba-Ahmadi and Tabor, 2009)) was used. In brief, the computational domain is prolonged upstream by a minimum of seven heights of the domain. In the present study, a distance of $8d$ is used. The (mean) velocity and Turbulence Kinetic Energy (TKE), which are sampled on the recycling plane of minimum three heights of the domain downstream from the inlet plane (see Figure 2.4.1), are copied to the inlet plane at each time step. Additionally, the flow inside the mapping area can be corrected by the specified (mean) bulk velocity (magnitude and direction). The following part of the domain between the recycling plane and area of interest is the so-called buffer zone. The buffer zone has to be no less than $4d$, preferably $5d$, to prevent any upstream influence from the area of interest to be mapped to the inlet. Further details can be found in Baba-Ahmadi and Tabor (2009), and Chaudhari (2014).

2.4.2   ABL rough wall function

The near-wall flow is hard to resolve with all local roughness elements of the real terrain. However, the instantaneous filtered resolved velocity $\widetilde{u}$ can be modelled using the aerodynamic roughness length z_0, as follows, (Monin and Obukhov, 1954):

$$\widetilde{u} = \frac{u_\tau}{\kappa} \ln\left(\frac{z}{z_0}\right),\qquad(2.4.1)$$

where κ=0.41 is the von Kármán constant, and u_τ is the frictional velocity. That is, the kinematic eddy viscosity on the wall $\nu_{sgs,p}$ can be computed as

$$\nu_{sgs,p} = \frac{u_\tau^2}{(\widetilde{u}_p/z_p)} - \nu,\, u_\tau = \frac{\widetilde{u}_p\kappa}{\ln\left(\frac{z_p}{z_0}\right)},\qquad(2.4.2)$$

where $(*)_p$ values correspond to the first interior nodes from the wall. The ABLRough-Wall function implemented in OpenFoam by Chaudhari (2014) is used in the present study. It was found earlier (Chaudhari, 2014) that the ABLRoughWall function gives an accurate prediction of the flow near the wall. Details of the wall function can be found in Chaudhari (2014).

Van Driest damping is used to get the correct behaviour of the turbulent viscosity near the wall. All the necessary boundary conditions used in the simulations are described for every variable in Table 2.4.1.

2.5   Flow initialization

At the beginning, two precursor simulations of the flow on the flat terrain without turbines with and without forest were carried out in the relatively short and shallow domains with coarse grid resolution. First of all, the flow for the precursor simulations were initialized using the logarithmic initial profile (laminar flow). Then the initial turbulence was generated by adding near-wall perturbations (sinusoidal streaks) for a certain frictional Reynolds number using the OpenFoam utility perturbU (de Villiers, 2006). Further, the turbulent inflow internal fields were mapped (using the OpenFoam utility mapped-Fields) from the fully developed pre-generated flow (precursor simulation) to the initial flow fields (with a similar Reynolds number) of the reference simulation. The reference simulation (with or without forest) is the flat-terrain simulation without turbines but with longer and/or higher geometry and/or refined grid than the precursor simulation. Then the resulted flow (the fully developed flow of the reference simulation) was used to be the initial flow for the wind-turbine simulation on the same geometry and grid.
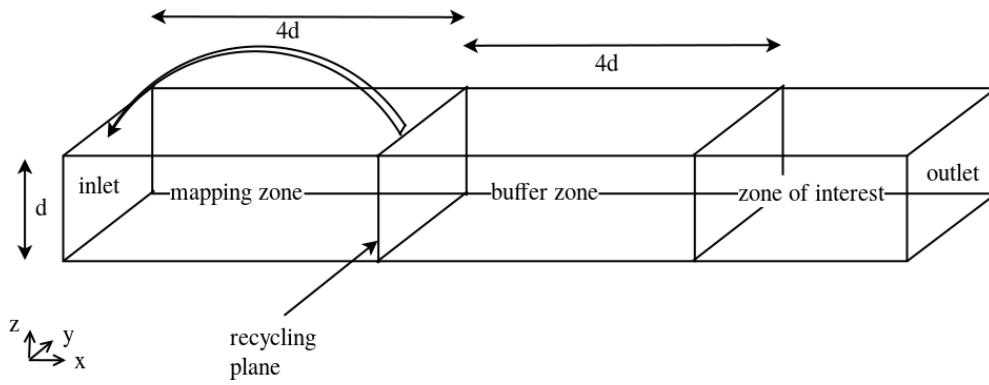
Figure 2.4.1: Schematic picture of the computational domain which shows the mapping technique.

Table 2.4.1: Description of the boundary conditions

	velocity	pressure	TKE
inlet	mapping or periodic	zero gradient	mapping or periodic
outlet	zero gradient	zero	zero gradient
top	symmetry	symmetry	symmetry
bottom	zero, ABLroughWall	zero gradient	zero gradient
sides	periodic	periodic	periodic

Chapter 3

Forest modelling

The canopy-drag model is not directly present in standard OpenFoam solvers (except the porous medium model). Thus, the canopy model implemented in OpenFoam (Agafonova et al., 2016a) is validated in the present study, at first with the existing numerical results from the literature (Shaw and Schumann, 1992). Secondly, the results of the LES with the forest-canopy model are compared to the field data (Bergström et al., 2013) and similar LES (Nebenführ and Davidson, 2014). Next, the ordinary atmospheric boundary layer flow simulations are performed in the computational domains of the different size and different angle of domain rotation (see Chapter 2). The obtained results are compared to the LES study by Munters et al. (2016). Finally, the comparison of the ordinary atmospheric boundary layer flow and atmospheric boundary layer flow in and above the forest canopy is shown in this chapter.

3.1   Validation of the implemented forest-canopy model

In the present study, following Shaw and Schumann (1992), the canopy layer is expressed via vertical distribution of the drag source (f_i^F). However, only the neutrally stratified flow is considered, therefore the heat transport equation is not solved and the heat source from the canopy is not considered. In order to avoid extremely fine grid resolution within the canopy layer, it has been chosen not to resolve the flow between the individual trees, but to treat the canopy as a porous medium with a horizontally uniform area density and a constant drag coefficient ($C_d^{'F}$).

The drag force f^F from equations (2.1.1) and (2.1.2) is a time-dependent force that is equal to the product of the local foliage density α_f (a function of height, known as Leaf Area Density (LAD)), the constant drag coefficient C_d^F and the square of the local velocity, such that the force f_i^F in the x_i direction is given by (Shaw and Schumann, 1992):

$$f_i^F = -\alpha_f C_d^F \, |u| \, \widetilde{u}_i = -\widetilde{u}_i/\tau, \tag{3.1.1}$$

where τ is a time scale for the canopy drag. Therefore, an additional limitation of the time-step size is created by the canopy drag term, $\Delta t < \tau$.

According to Shaw and Schumann (1992) and based on the analysis of micro-meteorological data from a deciduous forest (Shaw et al., 1988), C_d^F is set to 0.15 in the present simulations.
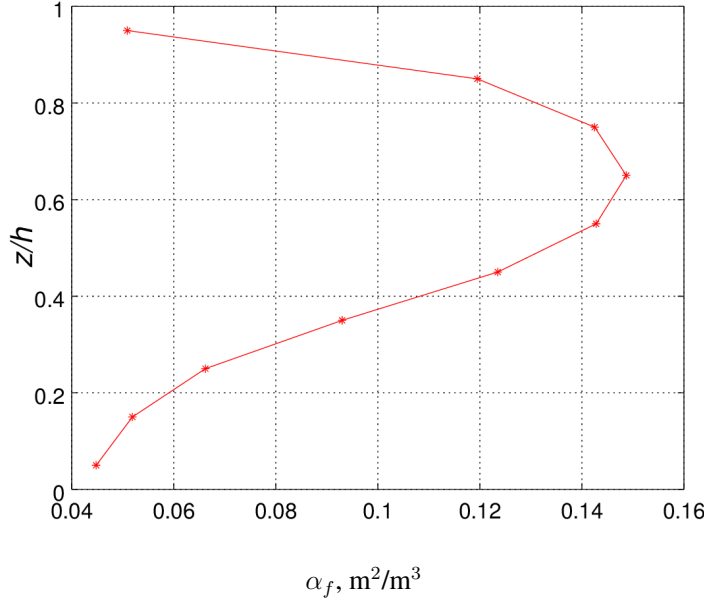
Figure 3.1.1: LAD profile with LAI =2, which corresponds to the pine forest (data from Shaw et al. (1988)).

Leaf Area Index (LAI) is a dimensionless parameter that characterizes how dense the canopy is. LAI (F) is defined as follows:

$$F = \int_0^h \alpha_f dz, \qquad (3.1.2)$$

where h is the canopy height, which is fixed to 20 m (as in Shaw and Schumann (1992)) in the present study. In the present study, the canopy with LAD from Figure 3.1.1 and LAI=2 is considered (as in Shaw and Schumann (1992)).
The computational domain of $3.2d \times 1.6d \times d$ in windwise, crosswind and vertical directions, correspondingly, and identical to that as used in Shaw and Schumann (1992), is considered in the validation simulation. As noted in Shaw and Schumann (1992), the height of the domain, which equals three heights of the canopy layer ($d = 3h$), seems to be enough to see the interaction between the canopy and ABL and to study the forest inflection of the ABL profile. However, it was also mentioned that a larger domain can be better used. Therefore, the larger domains are used in the LES described in the next sections. The computational grid has 2 m resolution in all directions. The driving force g is set to 0.0007 m/s^2 (without turning) in order to perform the periodic flow with a mean

windwise wind speed of 2 m/s. The standard periodic conditions are also used in the crosswind direction. The bottom has a wall-stress condition (the velocity is fixed to zero and simple ABL nuSGS rough wall function is applied (see Chapter 2). The roughness length is equal to 2 cm ($z_0 = 0.02$ m). The top boundary is a symmetric plane (free-slip). In the present study, the neutral stratification condition is used, but the results from Shaw and Schumann (1992) were obtained under the weakly unstable condition. Following Schlegel et al. (2012) and because of the lack of data under the neutral condition, the study by Shaw and Schumann (1992) was chosen for validation of the present canopy-model implementation even though it has different stability conditions.

Figure 3.1.2 top shows windwise velocity (U) averaged in time and horizontal directions and normalized by the velocity (U) averaged in the vertical direction (U_{ref}). As one can see, the present LES prediction of mean windwise velocity is in good agreement with the one obtained by Shaw and Schumann (1992) in general. However, both present LES, obtained by pisoFoam and RK4ProjectionFoam, slightly underestimate the mean windwise velocity above the canopy top in comparison with Shaw and Schumann (1992). The difference in the solution can be due to the different stratification conditions.
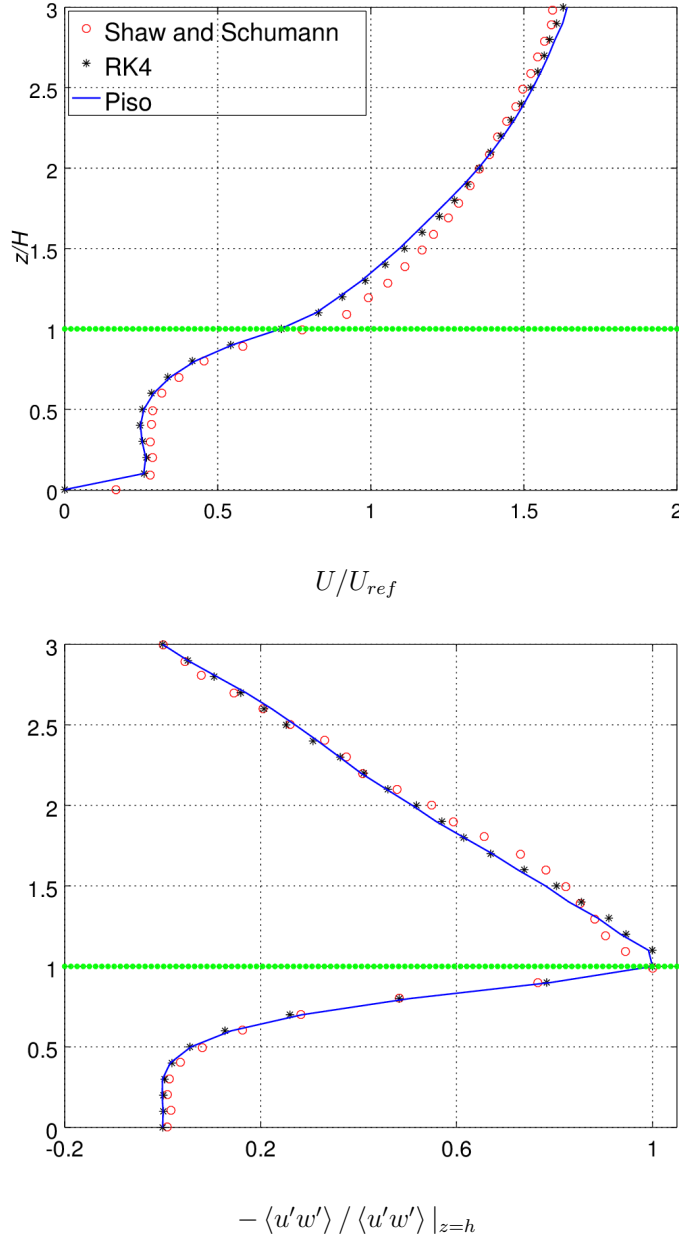
Figure 3.1.2: Validation of the implemented canopy model. Normalized mean windwise velocity and vertical Reynolds shear stress predictions obtained by RK4ProjectionFoam and pisoFoam are compared to the study by Shaw and Schumann (1992). The validation data are digitally extracted from the paper Shaw and Schumann (1992). The green dots represent the canopy top.

The LES prediction of mean vertical Reynolds shear stress ($\langle u'w' \rangle$) normalized by the reference value ($\langle u'w' \rangle |_{z=h}$) taken at $z = h$ is presented in Figure 3.1.2 (bottom). It can be seen from the figure that the present LES is in good agreement with Shaw and Schumann (1992) for the vertical Reynolds shear stress.

3.2 Comparison with the field measurements

The flow with the forest-canopy model was compared by Patton (1991); Schlegel et al. (2012), and Nebenführ and Davidson (2014) to the wind-tunnel data and field measurements, respectively. According to the above mentioned studies, LES with the forest-canopy model gives a good agreement with the measurements.
Following Nebenführ and Davidson (2014), the data reported by Bergström et al. (2013) for Swedish forest was chosen in order to validate the present LES with the forest-canopy model.
The simulation of case F2m4 (see Table 3.2.1) similar to Nebenführ and Davidson (2014) was performed. In addition, the case F2m2 with LAD from Shaw and Schumann (1992) was also simulated in order to see the differences in the flow in and above the forest due to different density of the forest. The driving force g is set to 0.003013 m/s^2 (without turning) in order to perform the periodic flow with a mean windwise wind speed of 10 m/s. A general description of the cases F2m4 and F2m2 as well as the case N8m4 performed by Nebenführ and Davidson (2014) is presented in Table 3.2.1.

Table 3.2.1: Description of the forest cases. Cases that begin with a capital F were performed by the author, and the case that begins with a capital N was performed by Nebenführ and Davidson (2014).

	d, m	$L_x \times L_y \times L_z$	$\beta_t,^o$	$\Delta x, \Delta y$, m	LAI
F2m2	432	$3.75d \times 2.5d \times d$	0	2[*]	2
F2m4	432	$3.75d \times 2.5d \times d$	0	2[*]	4.3
N8m4	400	$4d \times 2d \times d$	0	8[**]	4.3

[*]At the first step, the grid has four meters resolution and consists of $405 \times 270 \times 124$ finite volume cells. However, the region $z \leq 180$ m is refined to two meters in every direction.
[**]The computational domain in this case is divided by $192 \times 96 \times 96$ finite volume cells. The grid size is constant in the windwise and crosswind directions. However, the lowest part of the domain (forest canopy) is covered by the first ten cells (Δz=2 m). The rest of the cells are geometrically stretched in the vertical direction by 1.7%.

Profiles of the LADs, which are used in the cases F2m2 and F2m4, are presented in Figure 3.2.1. Leaf area density with LAI = 4.3 is digitally extracted from Nebenführ and Davidson (2014). For their part, Nebenführ and Davidson (2014) generated LAD from the measured data using the empirical model of Lalic and Mihailovic (2004). As it can be seen from the picture, max(α_f) is more than two times higher in the case F4n2m2 than in the case of F4n2m4. Therefore, one can assume that the behaviour of the wind flow in

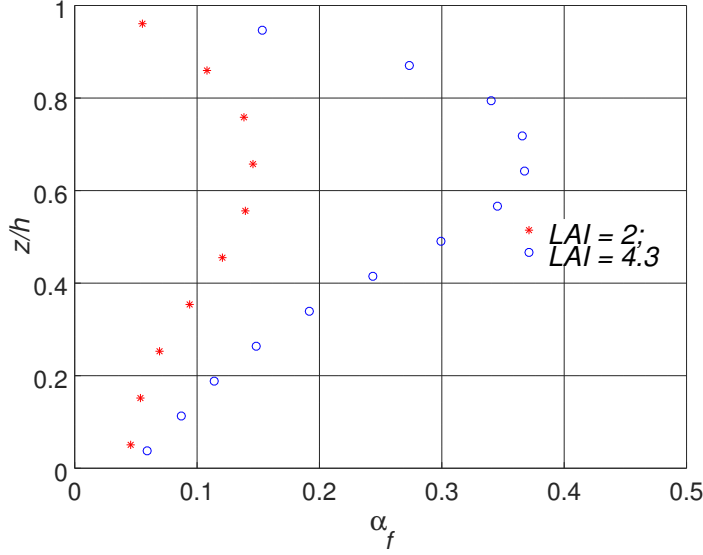and above the forest in these cases will be different.

Figure 3.2.1: LAD profiles with LAI =2 and LAI = 4.3, which correspond to the cases F2m2 and F2m4. LAD with LAI = 4.3 is digitally extracted from Nebenführ and Davidson (2014).

Figure 3.2.2 shows the comparison between the performed LES with the forest-canopy model (case F2m4), similar LES performed by Nebenführ and Davidson (2014) (case N8m4), and field measurements reported by Bergström et al. (2013). It can be seen from Figure 3.2.2 (top) that the horizontal wind velocity $M = \sqrt{U^2 + V^2}$ obtained in the case F2m4 agrees very well with N8m4 inside and about five canopy heights above the canopy ($z < 5h$). Then, above $z > 5h$ profiles have strong disagreement. According to existing field measurements, both profiles of normalized mean horizontal velocity agrees with measurements very close. However, the present study has better agreement than Nebenführ and Davidson (2014) in two highest measured locations ($z = 5h$ and $z = 6h$). This can happen due to different flow configurations. Frictional velocity $u_\tau = \left(\langle u'w' \rangle^2 + \langle v'w' \rangle^2 \right)^{1/4} \big|_{z/h=2}$ estimated from the digitally extracted data from Nebenführ and Davidson (2014) is equal to 0.55. But in the present study, $u_\tau = 1.07$. Non-normalized wind will be studied and compared to the field measurements below in Figure 3.2.4.

The normalized mean vertical Reynolds shear stress for the present LES as well as the LES carried out by Nebenführ and Davidson (2014) are compared with the measurements in Figure 3.2.2 (bottom). A good agreement is found between the present LES and field data for all measured locations except one at $z/h = 2.5$. The obtained value deviates from the measured one by 11.5% at $z/h = 2.5$. Moreover, the present LES has better agree-

ment with measurements than Nebenführ and Davidson (2014). They got good agreement only for three out of six locations.

Figure 3.2.3 shows the normalized mean primary (normal) Reynolds stress profiles for cases F2m2, F2m4, N8m4 and field measurements. All three LES significantly overestimate the maximum values at $z = 1.6h$ and $z = 2.5h$ of the primary windwise component of Reynolds stress tensor estimated from measurements in the field. However, they have better agreement at upper positions. In contrast, both present LES have excellent agreement for the crosswind component at the two lowest positions $z = 1.6h$ and $z = 2.5h$ and underestimate measurements at other positions. It can be seen that the LES with less dense forest (case F2m2) has the closest prediction (of all three simulations) of $\langle v'v' \rangle / u_\tau^2$. The vertical stress is slightly underestimated by the LES of the cases F2m4 and N8m4 (both have LAI = 4.3). Nevertheless, the LES of the case F2m2 again gives the best agreement among all three, and it is very close to the measured data.
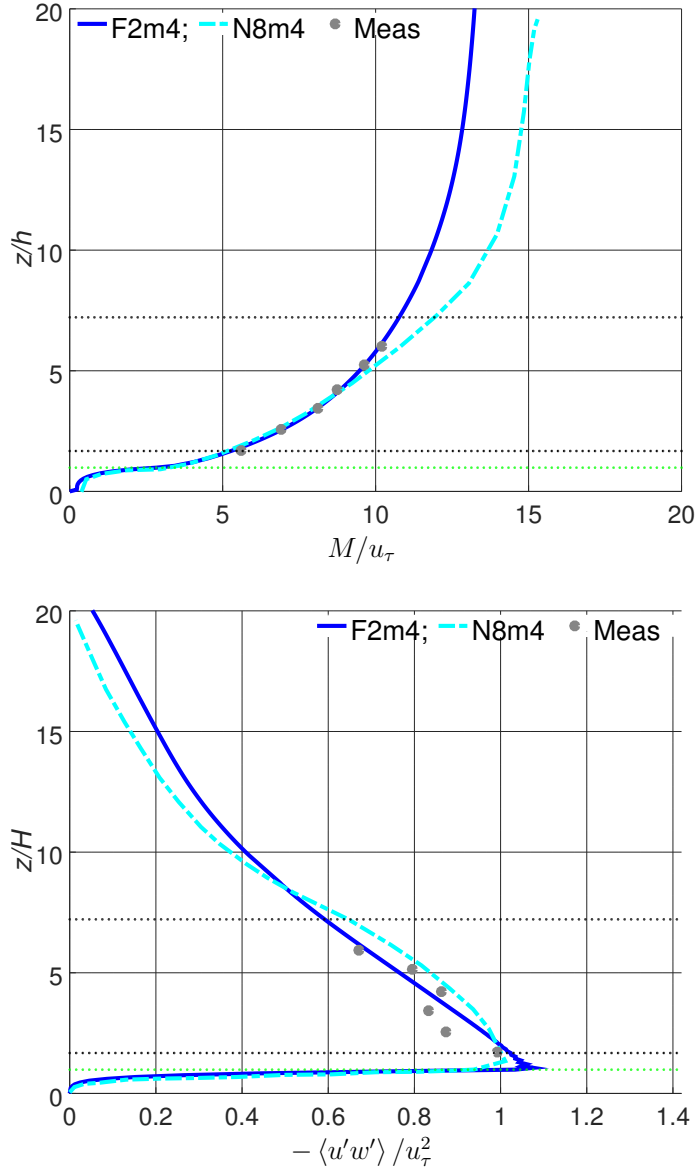
Figure 3.2.2: Normalized mean horizontal velocity M/u_τ (where u_τ is the frictional velocity) (top) and vertical Reynolds shear stress $-\langle u'w' \rangle /u_\tau^2$ (bottom) profiles for cases F4n2m4, N4n2m4 and field measurements (Bergström et al., 2013). The blue solid line corresponds to the present LES case with LAI = 4.3, and the cyan dashed-dotted line corresponds to the case performed by Nebenführ and Davidson (2014). Measurements are plotted by grey dots. The top of the canopy indicated by small green dots and the area of interest is indicated by small black dots.
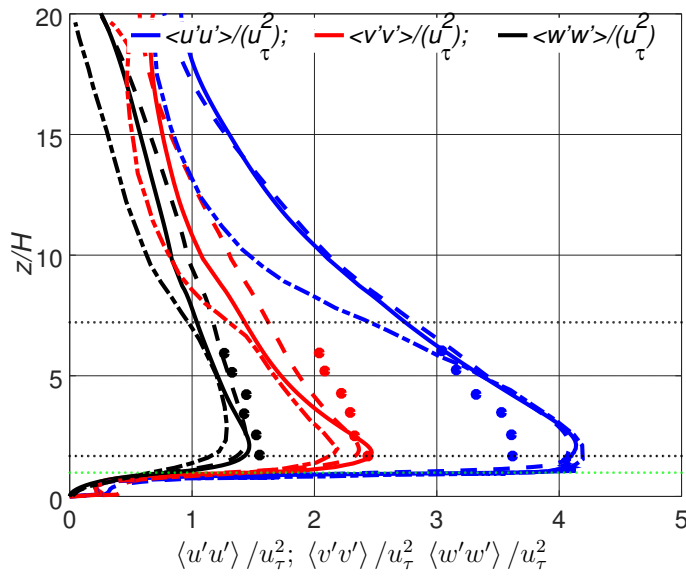
Figure 3.2.3: Normalized mean primary (normal) Reynolds stress profiles for cases F2m2, F2m4, N8m4 and field measurements. Solid lines (blue, red and black) represent the windwise, crosswind and vertical primary stresses, respectively, of the case F2m4. Dashed lines represent the primary stresses of the case F2m2, and dashed-dotted lines for the case N8m4. Measurements are plotted by large dots. The top of the canopy is indicated by small green dots and the area of interest is indicated by small black dots (Bergström et al., 2013).

The non-normalized mean wind speed and turbulence intensity for the cases F2m2 and F2m4 and data from the field are shown in Figure 3.2.4. Both of the velocities and turbulence intensities are in the one-standard deviation intervals which shows the correct choice of the flow properties for both of the present LES. However, the profiles of the case with lower LAI =2 better corresponds to the measurements. The LAD from Shaw and Schumann (1992) seems to be the better model of the Swedish forest from field near Ryningsnäs. Therefore, this LAD profile will be used in all of the following simulations with canopy model in the present study. The mean wind speed inside the smaller density forest (LAI=2) is higher than the wind speed inside the larger density forest (LAI=4.3). From the bottom to the middle of the canopy, the wind speed differs at most on 0.75 m/s. Then at the upper layers of the canopy, the difference almost disappears. At the canopy top ($z/h = 1$), the mean horizontal wind speeds are equal. Next, the velocity in case F2m4 increases more rapidly than the one in case F2m2. In the uppermost position of the domain, the wind speed above the more dense forest is larger but not more than 1 m/s. From this figure, one can conclude that the wind shear in the case of the larger LAD should be slightly larger.

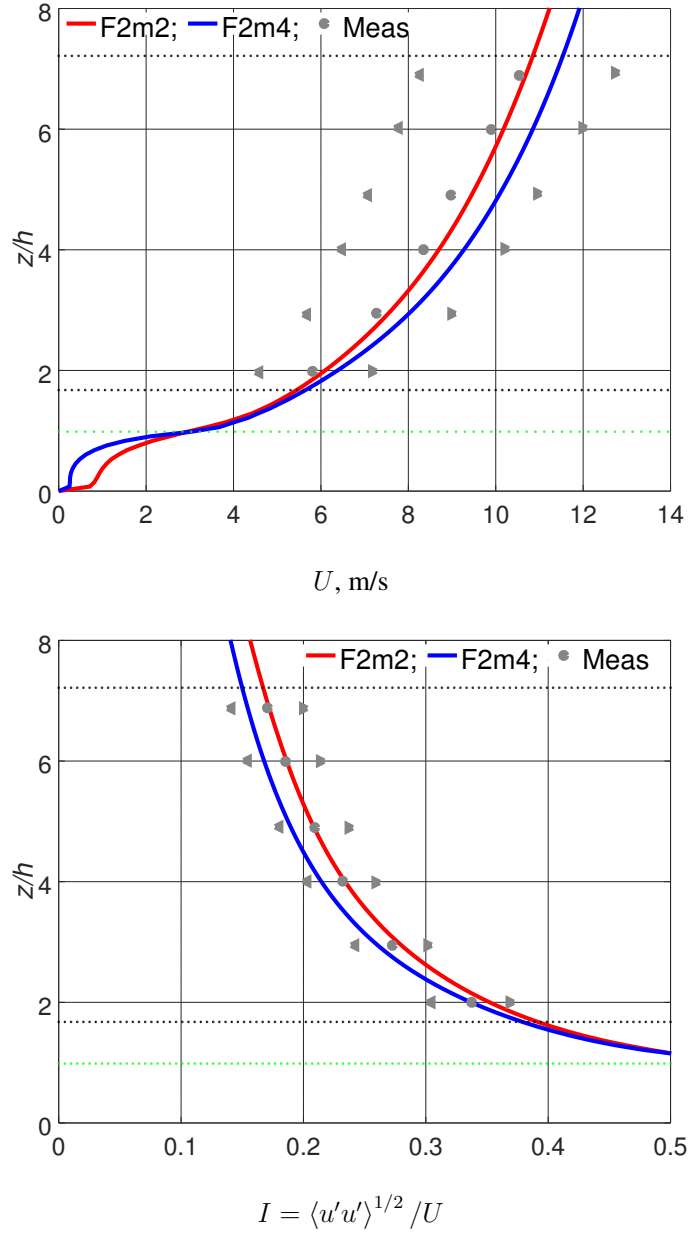Figure 3.2.4: Non-normalized mean windwise velocity U (top) and turbulence intensity $I = \langle u'u' \rangle^{1/2} /U$ (bottom). Measured mean values are plotted by large grey dots. Large grey triangles indicate one standard deviation interval.

3.3   Ordinary atmospheric boundary-layer flow

Several LES were performed in order to find the effects of domain size on ordinary atmo-
spheric boundary-layer flow without forest-canopy model. A general description of the
cases performed in the present study, as well as the cases performed by Munters et al.
(2016) and used for comparison, can be found in Table 3.3.1. The driving force g is set to
5.3e-05 $\mathrm{m/s}^2$ in order to perform the periodic flow with a mean windwise wind speed of
2 m/s.

Table 3.3.1: Description of the half-channel flow cases. The cases that begin with a
capital C were performed by the author, and the cases that begin with M were performed
by Munters et al. (2016).

	d, m	$L_x \times L_y \times L_z$	$N_x \times N_y \times N_z$	$\beta_t,^o$	$\Delta x = \Delta y$, m
C4n	180	$4d \times 2d \times d$	$360 \times 180 \times 90$	0	2
M4n	*	$\pi d \times 2\pi d \times d$	$128 \times 256 \times 128$	0	
C12n	180	$12d \times 6d \times d$	$1080 \times 540 \times 90$	0	2
C12t	180	$12d \times 6d \times d$	$1080 \times 540 \times 90$	5	2
M12n		$4\pi d \times 2\pi d \times d$	$512 \times 256 \times 128$	0	
M12t		$4\pi d \times 2\pi d \times d$	$512 \times 256 \times 128$	2.5	

* Munters et al. (2016) used dimensionless d and Δx.

Munters et al. (2016) proposed so-called shifted periodic conditions to get rid of the ef-
fects created by running a periodic simulation in a too-short computational domain in the
windwise and crosswind directions. The idea of the shifted periodic conditions is to copy
the solution from the outlet not directly to the inlet plane of the domain but shifted in
the crosswind direction on a shifting distance d_s. The proposed method is able to avoid
non-physically long coherent structures already produced by normal periodic conditions
in a relatively short computational domain ($2\pi d \times 2\pi d \times d$, where d is the height of the
domain). Similarly to Munters et al. (2016), two slightly different periodic LES were car-
ried out in the computational domain of the size $12d \times 6d \times d$. The first simulation C12n
was performed by using the driving force approach where driving force $\vec{g} = (g, 0, 0)$ was
directed in the x direction only. That is, the flow was driven in the windwise direction. In
the second LES C12t, the computational domain was slightly rotated around the vertical
axis. Thus, the driving force $\vec{g} = (g \cos(\beta_t), g \sin(\beta_t), 0)$, where the angle $\beta_t = 5^o$. Using
turning in combination with classic periodic condition is equal to copying the solution
from the outlet to the inlet plane, but shifted in the crosswind direction relative to the pre-
vious inlet. This approach, with $\beta_t = 5^o$ (described in detail in Figure 3.3.1) is found to be
very similar to Munters et al. (2016) using shifting distance $d_s = d$. However, the turned
computational domain has to be turned back during the postprocessing on the angle -5°.
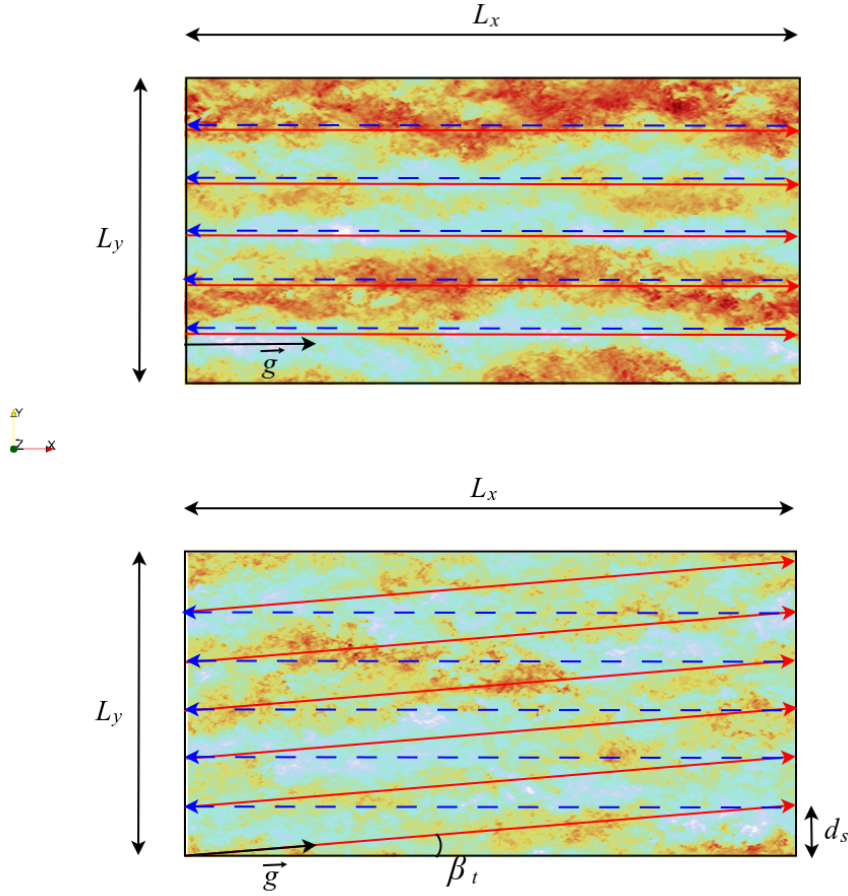The postprocessing is described in Figure 3.3.2.

Figure 3.3.1: Visualization of the periodic flow without the turning (top) and with the turning (bottom) . The flow direction is indicated by red solid arrows. The direction of (periodicity) copying the solution from outlet to the inlet plane is shown by blue dashed arrows. The driving force $\vec{g}$ is the black arrow.
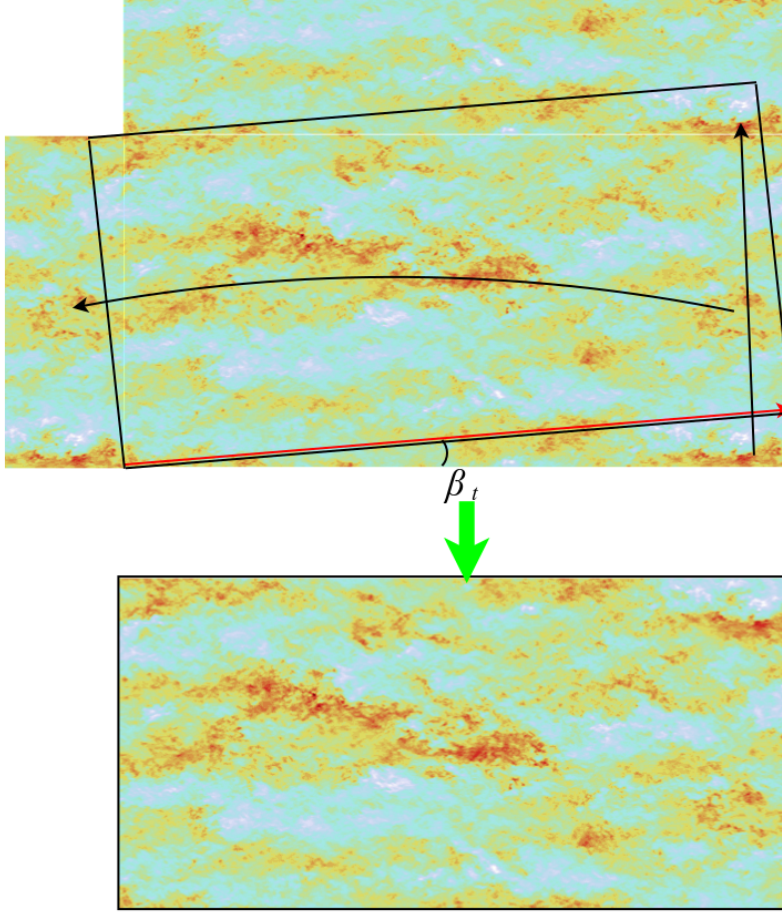
Figure 3.3.2: Schematic description of the turned case postprocessing. The black arrows indicate replication of the obtained solution to the left and above of the solution due to periodicity. White rectangle (in top picture) is the cross-section of the computational domain. Black rectangle (in both pictures) represents the cross-section of the analysis domain.

In order to illustrate the crosswind inhomogeneities (in other words, how much maximum and minimum of the time-averaged velocity deviates from the mean) in the present LES and to compare the present LES with Munters et al. (2016), the normalized peak-to-trough variation Δ is used. Δ is defined as follows (Munters et al., 2016):

$$\Delta(z) = \max_{x} \left[\frac{1}{\langle U(x,y,z) \rangle |_{x,y}} \left(\max_{y}(U(x,y,z)) - \min_{y}(U(x,y,z)) \right) \right], \qquad (3.3.1)$$

where U is time-averaged windwise velocity and $\langle U(x,y,z) \rangle |_{x,y}$ is horizontal space av-

erage of U. Figure 3.3.3 shows peak-to-trough crosswind inhomogeneity factor Δ for the normal cases (C4n, M4n, C12n , M12n), with turned by 5° domain (C12t) and shifted periodic conditions (M12t). It can be seen that the results of the present LES correspond to the results of a similar LES performed by Munters et al. (2016). As an exception, case C4n can be considered which computational domain size differs from M4n more than in the other cases. That is, $L_x = 4d$ and $L_y = 2d$ in case C4n in spite of $L_x = \pi d$ and $L_y = 2\pi d$ in the case M4n. Δ from case C4n is smaller (on average by 3-4%) than the one from case M4n at $z > 0.35h$. This can be due to the slightly larger length of domain L_x. At the same time, most probably because of the smaller width of domain L_y, Δ in case of C4n is larger by 4% at $z < 0.35h$. Otherwise, Δ in case of C12n is smaller by 0.5% than the one obtained by Munters et al. (2016), which can happen due to the larger time-averaging interval in case C12n. The very small value of $0.4 < \Delta < 3$ in the cases with a large length of the domain ($L_x \geq 12d$) and turning/shifting indicates that in these cases the flow is homogeneous in the crosswind direction, and the length of the domain $L_x = 12d$ in combination with turning/shifting is more than enough.
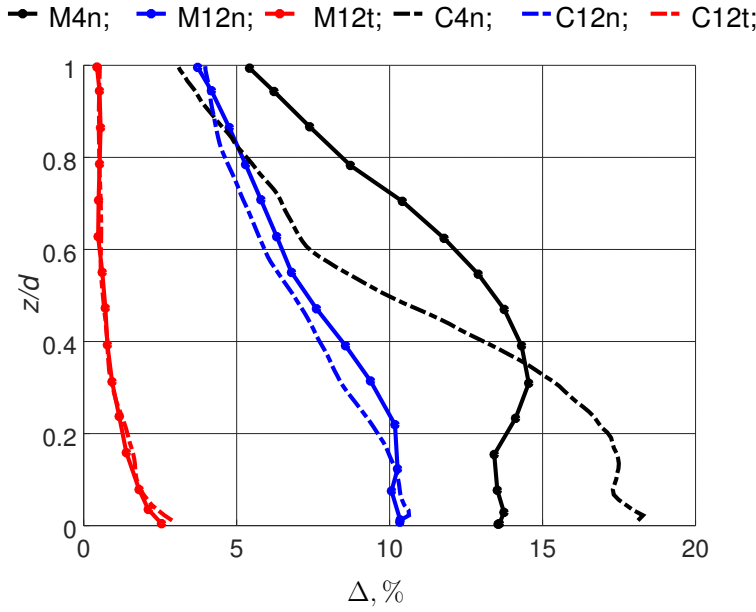
Figure 3.3.3: Peak-to-trough crosswind inhomogeneity factor Δ

Let us consider the autocorrelation function of velocity fluctuations. Autocorrelation function indicates how much turbulence fluctuation at $\vec{x} + \vec{r}$ follows the one at $\vec{x}$.
The autocorrelation function, for example, for the windwise component is represented as follows:

$$Ruu(\vec{r}, z) = \frac{\frac{1}{TL_xL_y} \int_x \int_y \int_t u'(\vec{x})u'(\vec{x} + \vec{r})dtdydx}{\langle u'u' \rangle}, \qquad (3.3.2)$$

where T, L_x and L_y are the total integration time, length in windwise and crosswind

directions, respectively. If $\vec{r} = (r_x, 0)$, then $Ruu(r_x, z) = Ruu_x$.

The windwise autocorrelation function Ruu_x is presented in Figure 3.3.4 at a certain vertical location ($z/d = 0.1$) for cases C4n, C12n, C12t, M4n, M12n and M12t. The value of Ruu_x at $r_x = 0$ is equal to 1. Then, theoretically, the (auto)correlation function has to decrease to 0 when r_x is large, which indicates that the length of the domain is large enough. In the present C4n as well as M4n (Munters et al., 2016) simulations, Ruu_x stays quite large ($Ruu_x = 0.33$ and $Ruu_x = 0.36$, correspondingly) at large r_x, as shown in Figure 3.3.4. In case of the slightly shorter domain (the M4n case) the correlation function at large r_x gives values slightly higher than in the reported C4n case. This follows the theory. Next, in case of the three to four times longer domain (C12n and M12n) than the case considered above, the autocorrelation drops to a much lower value, that is, $Ruu_x = 0.12$. However, the domain length of 12 heights of domain is still not long enough. According to Munters et al. (2016), the windwise autocorrelation decreased to zero when the domain length was equal to approximately 38 domain heights ($12\pi d$). However, 38 domain heights ($L_x = 12\pi d$) is not yet long enough to prevent the "locking effect" (Munters et al., 2016). The "locking effect" is the presence of crosswind inhomogeneities in contour plots of fully developed and long-time averaged windwise velocity at a fixed vertical location. The "locking effect" (the presence of white and red stripes) can be seen in Figure 3.3.5 for the C12n case. Finally, Fang and Porté-Agel (2015) simulated the case in a significantly large domain with a size of $100d \times 13d \times d$ (or $32\pi d \times 4\pi d \times d$). They reported that Ruu_x drops below zero at $r_x/d = 10$ in that case. Similar achievement was obtained by Munters et al. (2016) in the M12t case as well as in the present C12t case. In both cases, M12t (see Figure 7 from Munters et al. (2016)) and C12t (see Figure 3.3.5), the crosswind inhomogeneities (red-white stripes from Figure 3.3.5) are not found.
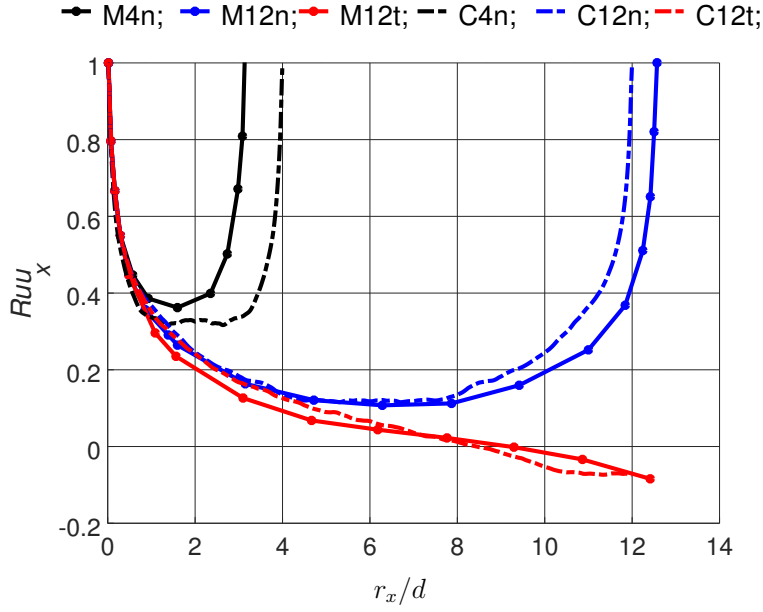
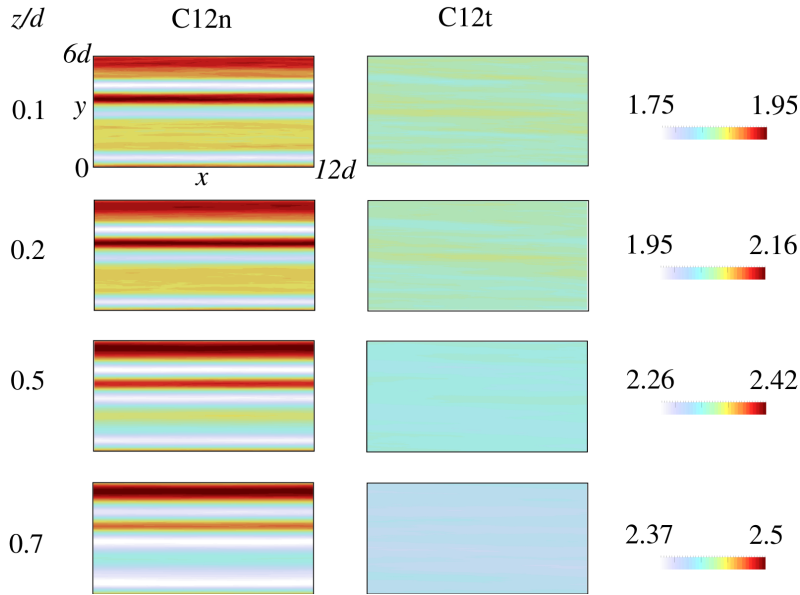Figure 3.3.4: One-dimensional windwise autocorrelations $Ruu_x(x)$ at $z/d = 0.1$ plane

Figure 3.3.5: Contour plots of time-averaged windwise velocity U at different vertical locations ($z/d = 0.1, z/d = 0.2, z/d = 0.5$ and $z/d = 0.7$) for cases C12n and C12t, which are described in Table 3.3.1.

3.4   Atmospheric boundary-layer flow over the forest

Several LES were performed in order to find the effects of the domain size and grid resolution on the atmospheric boundary-layer flow with the forest-canopy model. The cases performed in the present study are described in Table 3.4.1. The driving force g is set to 0.0007 m/s^2 (without turning) in order to drive the periodic flow with mean windwise wind speed of 2.5-3 m/s.

Table 3.4.1: Description of the cases with the forest. Forest represented by forest canopy with LAD from Shaw and Schumann (1992) (see Figure 3.4.1).

	d, m	$L_x \times L_y \times L_z$	$N_x \times N_y \times N_z$	$\beta_t,^o$	$\Delta x (= \Delta y)$, m
F4n2m	180	$4d \times 2d \times d$	$360 \times 180 \times 90$	0	2
F12n2m	180	$12d \times 6d \times d$	$1080 \times 540 \times 90$	0	2
F12n4m	180	$12d \times 6d \times d$	$540 \times 270 \times 45$	0	4
F12t2m	180	$12d \times 6d \times d$	$1080 \times 540 \times 90$	5	2

Figure 3.4.2 shows a comparison of mean windwise velocities between cases F4n2m, F12n2m, F12n4m and F12t2m. As concluded above, the length of the domain $L_x = 4d$ is significantly less than necessary to avoid the "locking effect". This may be the reason that the mean windwise wind speed obtained in case F4n2m differs from the one obtained in case F12n2m by approximately 4% (see Table 3.4.2). The fact that the length of the domain $L_x = 12d$ without rotation (turning) is not yet enough does not affect the velocity in case F12n2m. It maximally deviates by 0.5% from the F12t2m value. However, the turbulence intensity relative error between the turned and non-turned cases is 2.5% (see Table 3.4.2). The relative error between the mean windwise velocity in the case with coarse grid (F12n4m) and refined grid (F12n2m, both non-tilted) is 9% at maximum inside the forest and 4.5% high above it ($z = 8h$).

Table 3.4.2: The relative error for mean windwise velocity and turbulence intensity between different cases and the reference case (F12t2m)

	F4n2m	F12n4m	F12t2m
U	4%	4.5%*(9%)	0.45%
k	24%	15%(17%)	2.5%

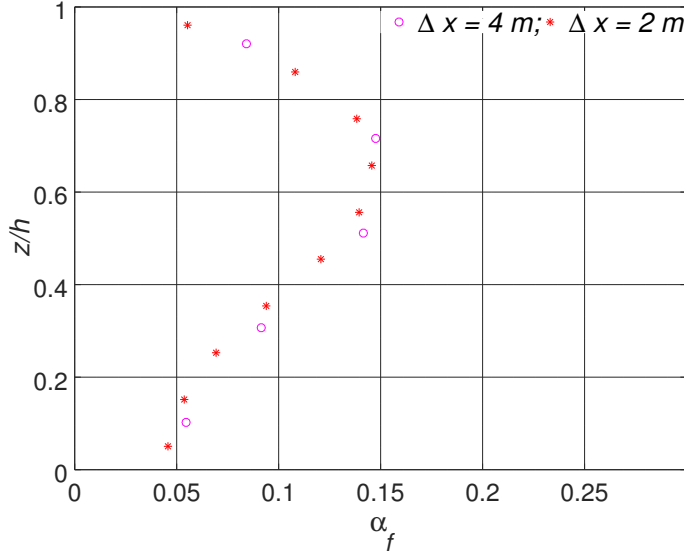* The maximum deviation occurs high above the forest. The value inside the forest is given in brackets.

Figure 3.4.1: LAD profiles with LAI =2 (Shaw and Schumann, 1992) which were used in cases F12n2m, F12t2m and F12n4m.

3.5 Forest effects on the wind flow (lower ABL) over an infinite flat terrain

In order to study the forest effects on the wind flow (lower ABL) over an infinite flat terrain, two LES (with and without forest) were performed. (See the description of cases F12t and C12t).

3.5.1 Description of the cases

The cases are described below and in Table 3.5.1. The feature of these cases is that the height of the computational domain is very small ($d = 9h$=180 m). From the one side of view, the results of the simulations may be spoiled by the upper boundary condition. From the other side, the importance of the length of the domain in the windwise direction, horizontal turning of the domain and fine (2 m resolution) grid was shown above. Ideally, the LES should be performed in the high and long computational domain on the fine grid. However, performing the simulations in the above-mentioned conditions is very time-consuming. (See the detail of the "ideal case" in Table 3.5.1.) Thus, that short domain is preferred to study the forest effects on the wind flow over infinite long flat terrain. In these circumstances, it seems to be less harmful to neglect the upper boundary condition effect on the flow, and especially it should not be very harmful to the lower ABL. Partially, the results of the low-height domain cases $d = 180$ m but long in the windwise direction are compared to the cases (F4d22h/C4d22h, $d = 432$) carried out in the high but
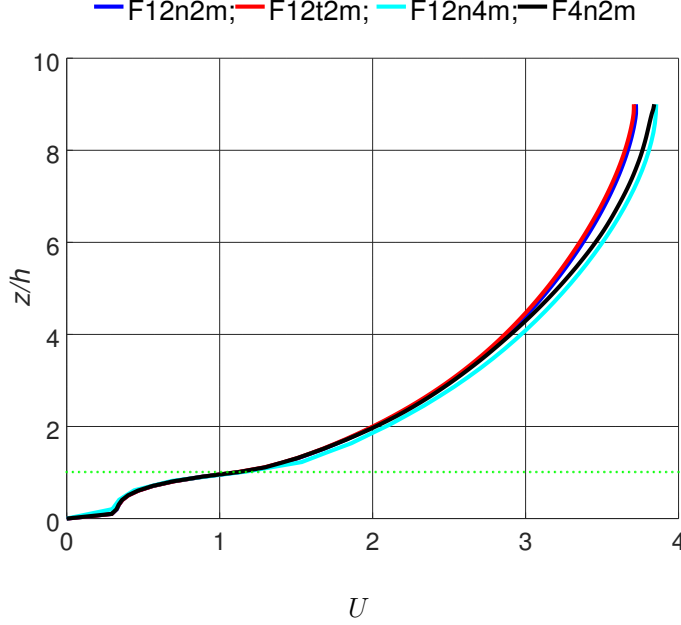
Figure 3.4.2: Mean windwise velocities in the cases F4n2m, F12n2m, F12n4m and F12t2m.

short computational domain.

Non-forest case: The computational domain is extended to 12 and 6 times the height of the domain d ($12d \times 6d \times d$) in the windwise and crosswind directions, respectively. The height of the domain is equal to $d = 180$ m. The corresponding case C12t (or C12t2m is called in the present subsection) is given above and described in the Table 3.3.1. The computational grid has 2 m resolution in all directions. An imaginary turbine with the hub-height $H = 4.5h = 90$ m and rotor diameter $D = 108$ m is considered here and below to highlight the zone of interest ($H - D/2 < z < H + D/2$). The domain is slightly rotated ($\beta_t = 5^o$) around the vertical axis. The standard periodic boundary conditions are used in the windwise and crosswind directions, accordingly. The bottom boundary has a wall-stress boundary condition, that is, zero velocity and the simple ABL nuSGS rough-wall function are applied. The roughness height is equal to 2 cm ($z_0 = 0.02$ m). The top boundary has a symmetric plane (or free-slip) condition. The driving force g is set to 0.000053 $\mathrm{m/s}^2$ in order to drive the periodic flow with a mean windwise wind speed of 2.5 m/s (actual mean wind speed at $z = H = 4.5h \ U_h$ = 2.34 m/s).

Forest case: The forest case is identical to the non-forest one, except that the terrain is covered by a uniform forest canopy. The forest height (h) is taken to be 20 m, following Shaw and Schumann (1992). Thus, the domain height is nine canopy heights ($d/h = 9$). The canopy model, based on the leaf-area-density approach from Shaw and Schumann

(1992) (see above), is used for modelling the forest. The LAD profile is shown in Figure 3.4.1 (or 3.1.1) taken from Shaw and Schumann (1992) for pine forest. The forest drag coefficient C_d is set to 0.15, similarly to Shaw and Schumann (1992). The corresponding case F12t2m is given above and described in Table 3.2.1. The driving force $g = 0.0007$ m/s^2 in order to perform the periodic flow with the similar mean windwise wind speed at the hub height of the imaginary wind turbine as in the case of C12t2m (actually, $U_h = 3.01$ m/s).

Table 3.5.1: Description of the cases with and without forest and different domain height. Forest represented by forest canopy with LAD from Shaw and Schumann (1992) (see Figure 3.4.1).

	F12d9h/C12d9h	F4d22h/C4d22h	"ideal" case
d, m	180	432	432
d/h	9	22	22
$L_x \times L_y \times L_z$	$12d \times 6d \times d$	$4d \times 2d \times d$	$12d \times 6d \times d$
$N_x \times N_y \times N_z$	$1080 \times 540 \times 90$	$405 \times 270 \times 124^*$	$2592 \times 1296 \times 216$
$\beta_t, ^o$	5	0	5
$\Delta x (= \Delta y)$, m	2	2	2
$N_{cells}^{tot}, \times 10^6$	52.5	56.4	725.6

*At the beginning, the grid had a four-meters resolution and consisted of $405 \times 270 \times 124$. However, the grid from the region $z \leq 180$ m was refined to two meters in every direction.

3.5.2 Mean flow, turbulence intensity, and Reynolds shear stress

Figure 3.5.1 shows the results obtained in F12d9h/C12d9h compared to the F4d22h/C4d22h cases. As one can see, the mean windwise velocity in the low-height domain cases has excellent agreement with the one in the high-domain cases. Indeed, there is a tiny effect (less than 2.4% at z/H=2) of the upper boundary on the mean windwise velocity normalized by the velocity at hub height in both the non-forest and forest cases. However, large differences between the turbulence intensities and vertical shear stresses exist. The results of the low-height domain cases are underestimated in both the cases (forest/non-forest). Thus, the relative difference between the forest and non-forest cases and the forest influence on the flow are very similar for the cases with low and high computational domains. For example, the turbulence intensity at hub height in the forest case is more than double that in the non-forest case. And the normalized vertical shear stress at $z/H = 1$ in the forest case is about eight times larger than the one in the non-forest case in both shallow and high cases. Thus, the normalized windwise velocity, turbulence intensity and vertical Reynolds shear stress and the other results of the low-height case (for example, the autocorrelation function and integral length scale) are considered below in more detail.

Figure 3.5.2 shows the LES-predicted mean windwise velocity normalized by the velocity at the hub height, turbulence intensity and vertical Reynolds shear stress normalized by the square of the velocity at the hub height. The difference in the shape of the mean (windwise) wind speed between the non-forest and forest cases is clearly seen in Figure 3.5.2 (top). The global wind shear is calculated across the rotor area of the imaginary turbine as follows

$$\alpha = \frac{H}{U_h} \left(\frac{U_{tip}^{up} - U_{tip}^{low}}{z_{tip}^{up} - z_{tip}^{low}} \right). \tag{3.5.1}$$

The wind shear calculated for non-forest and forest cases in the present work are $\alpha = 0.14$ and $\alpha = 0.48$, respectively. The values of the wind shear fitted from the velocity profiles by Nebenführ and Davidson (2014) are slightly higher and equal to $\alpha = 0.19$ for the non-forest and $\alpha = 0.52$ for the forest case.

The windwise turbulence intensity

$$I = I_u = \frac{\langle u'u' \rangle^{1/2}}{U|_{z=H}} \tag{3.5.2}$$

is presented in Figure 3.5.2 (middle). The turbulence intensity from the forest case is two times higher than in the case without forest. The field measurements by Bergström et al. (2013) give the range of turbulence intensity $18\% < I < 25\%$ at $z = 4.5h$ above the forest. The study by Nebenführ and Davidson (2014) gives the values of windwise and vertical turbulence intensities at hub-height of the virtual turbine of $I = I_u = 19.9\%$ and $I_w = 11.6\%$, respectively, (or $I_{uw} = \sqrt{I_u^2 + I_w^2} = 23\%$) in the forest case and $I = 8.6\%$ and $I_w = 4.8\%$ (or $I_{uw} = 9.8\%$) in the non-forest case. However, the values of windwise and vertical turbulence intensities predicted by the present LES are $I = 17\%$ and $I_w = 10.5\%$, respectively, (or $I_{uw} = 20\%$) in the forest case and $I = 6.9\%$ and $I_w = 3.6\%$ (or $I_{uw} = 7.8\%$) in the non-forest case.

The vertical shear stress normalized by the squared velocity at hub-height is presented in Figure 3.5.2 (bottom). The maximum value of $-\langle u'w' \rangle /U^2|_{z=H}$ in the case of forest is about 7-8 times higher in comparison to the non-forest case. However, a smaller increase (only two times higher than without forest) was found by Nebenführ and Davidson (2014). The difference in the results of Nebenführ and Davidson (2014) can be due to the different forest parameters (LAI = 2 in the present work but LAI=4.3 in the study (Nebenführ and Davidson, 2014)), different grid resolution (4 m in the present LES and 8 m in the work by Nebenführ and Davidson (2014), the presence of the Coriolis force in Nebenführ and Davidson (2014)) and different normalization. The mean windwise velocity at hub-height $U_h = 2.34$ m/s in the non-forest case and $U_h = 3.01$ m/s in the forest case are used in the present study and geostrophic velocity $u_g = 10$ m/s is used by Nebenführ and Davidson (2014) in both cases. At most, the difference (especially in the normalized vertical Reynolds shear stress) is because of the different flow conditions. That is, in the present study the frictional velocity (u_τ) calculated at $z = 2h$ in the forest and non-forest cases are 0.31 and 0.085 (the ratio is 3.65), respectively. However, the values estimated from Nebenführ and Davidson (2014) are 0.556 and 0.39 (ratio is 1.44), respectively, for the non-forest and forest cases. Moreover, Figure 3.2.3 shows that the present LES prediction

(case F2m4) for $-\left\langle u'w' \right\rangle /u_\tau^2$ compares well to Nebenführ and Davidson (2014)) and the field measurements (Bergström et al., 2013).

The maximum values of wind shear and turbulence intensity, given by international safety standards in 2005 (IEC, 2005) for the strongest turbine class, are $\alpha = 0.2$ and $I = I_u = 16\%$, respectively. The given values are much less than those predicted by LES in the forest case. The increased turbulence and high wind shear can be harmful for the turbines which are designed according to IEC (2005). Thus, the placement of the turbines (which are not designed for the above-mentioned forest wind conditions) in a forest-covered terrain may lead to the shortened turbine life cycle.
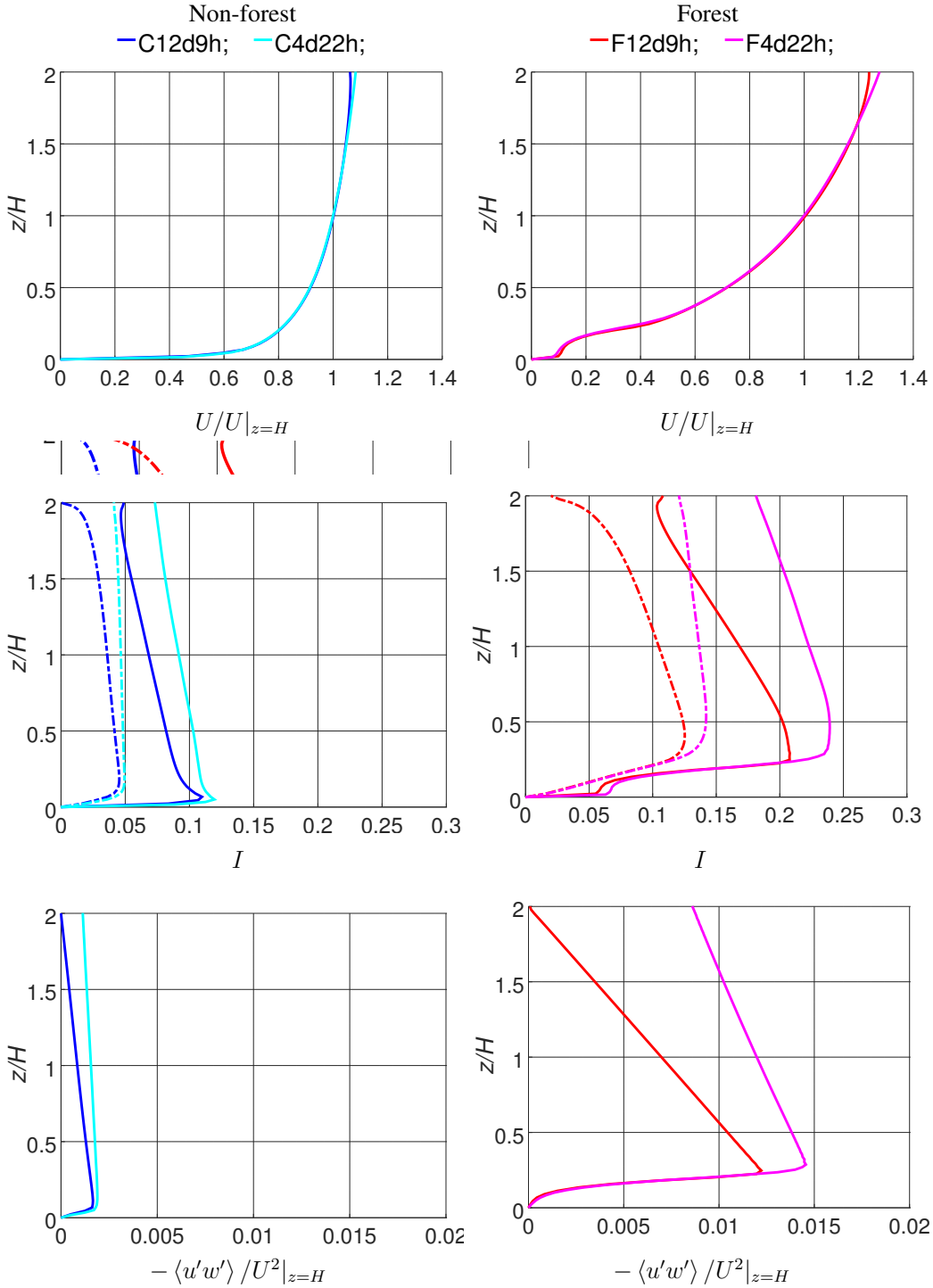
Figure 3.5.1: The LES prediction for the normalized mean windwise velocity ($U/U|_{z=H}$), turbulence intensity components (windwise and vertical) and vertical Reynolds shear stress for the cases with and without forest and different height of the domain ($d = 180$ m and $d = 432$ m).
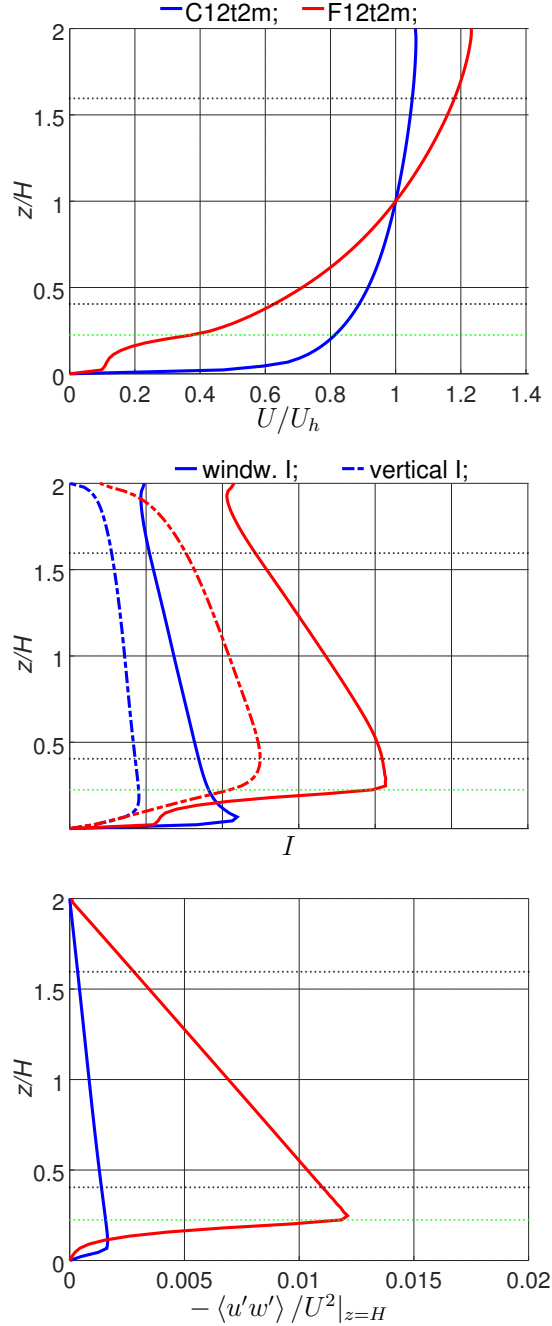
Figure 3.5.2: Normalized mean windwise velocity $U/U|_{z=H}$ (where H is the hub height of the virtual turbine) (top), windwise turbulence intensity $I = I_u = \langle u'u' \rangle^{1/2} / U|_{z=H}$, vertical turbulence intensity $I_w = \langle w'w' \rangle^{1/2} / U|_{z=H}$ (middle) and vertical Reynolds shear stress $- \langle u'w' \rangle / U^2|_{z=H}$ (bottom). Black dots denote the zone of interest (upper/lower tip positions of the turbine blades) and green is the top of the canopy.

3.5.3   Further turbulence statistics

Let us consider the autocorrelation function of velocity fluctuations, for example, for the windwise velocity component u:

$$Ruu(\vec{r}, z) = \frac{\frac{1}{TL_xL_y} \int_x \int_y \int_t u'(\vec{x})u'(\vec{x} + \vec{r})dtdydx}{\langle u'u' \rangle}, \qquad (3.5.3)$$

where $\vec{r}$ is the displacement vector between two correlated values of u', that is at, positions $\vec{x}$ and $\vec{x} + \vec{r}$. T, L_x and L_y are the total integration time, lengths in the windwise and crosswind directions, respectively. If $\vec{x} = (x, 0, 0)$ and $\vec{r} = (r_x, 0, 0)$ then $Ruu(r_x, z) = Ruu_x$. The windwise autocorrelation function Ruu_x is presented in Figure 3.5.3 at certain vertical locations ($z = h/2$=10 m, $z = 1.3h \approx$26 m, $z = H - R$=36 m, $z = H - R/2 \approx$64 m, $z = H$=90 m, $z = H + R/2 \approx$118 m and $z = H + R$=144 m) for non-forest (top) and forest (bottom) cases. The autocorrelation function indicates how closely turbulence fluctuation at $\vec{x} + \vec{r}$ follows the one at $\vec{x}$. The value of Ruu_x at $r_x = 0$ is equal to 1. Then theoretically, the autocorrelation function has to decrease to 0 when r_x is large, which indicates that the length of the domain is large enough. Using the turned domain approach in a rather large domain ($12d \times 6d \times d$) leads to correlations that go close to zero at large r_x as expected (see Figure 3.5.3). The similar flat terrain simulations with and without forest in the shorter domain were also performed. In the case of the shorter domain ($4d \times 2d \times d$), Ruu_x stays quite large at large r_x. As it was previously concluded, the length of the domain $L_x = 4d$ is too short, and $L_x = 12d$ in combination with the turned domain approach is sufficiently long to avoid the "locking effect".
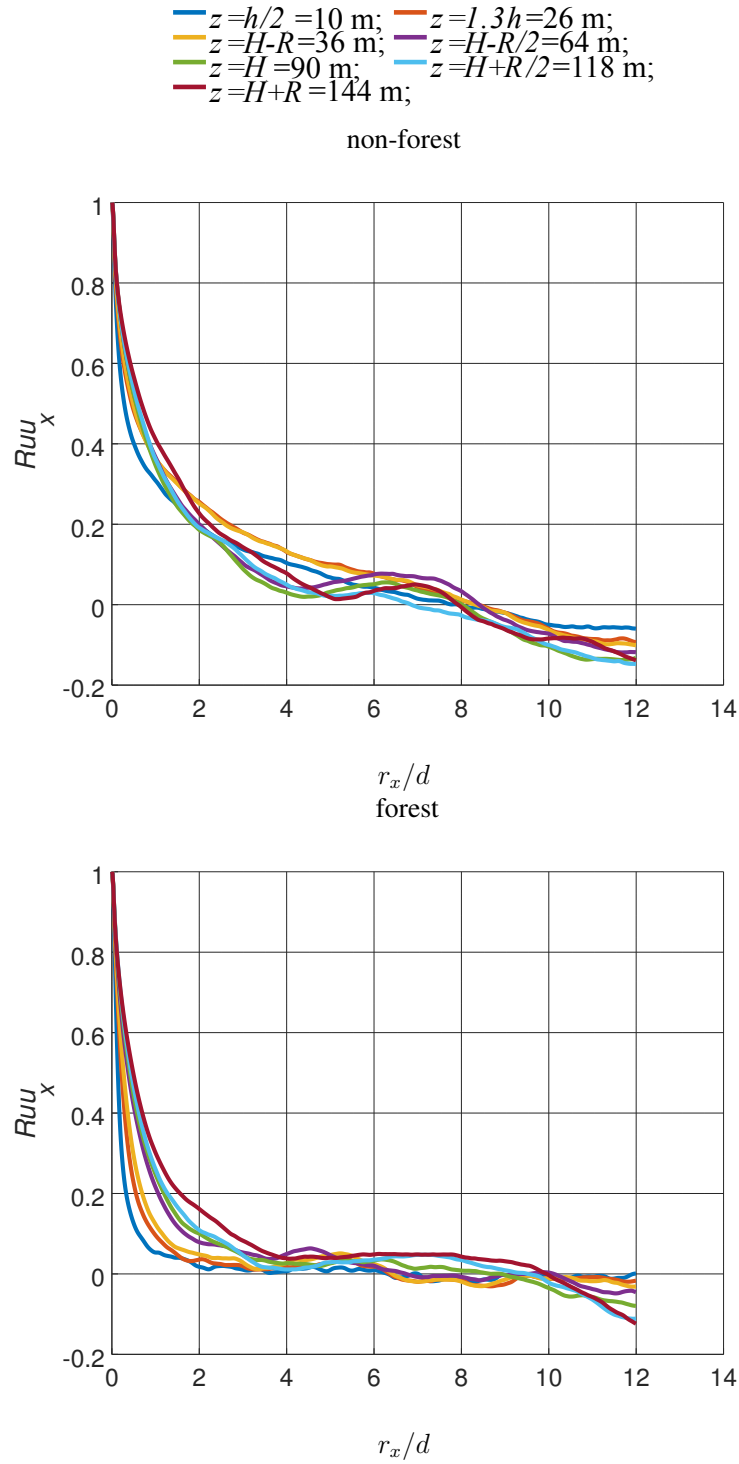
Figure 3.5.3: Correlation function Ruu_x calculated for the non-forest case and the forest case at different vertical locations.

From the figure (non-forest case), one can see that the lines are grouped differently: one group is when 10 m $\leq z \leq$ 36 m, and the other is when 36 m$< z <$ 144 m. The two groups have different line curvature values, while the curves of one group have similar curvature values. All curves cross zero and then stay negative. The maximum negative value of Ruu_x = -0.15. However, all correlations of windwise velocity fluctuations for the forest case are well-organised in the ascending order. Moreover, the profiles of Ruu_x have curvature similar to each other in the forest case. The curves inside and slightly above the forest (when 10 m $\leq z \leq$ 36 m) are mostly near the zero. However, the correlation function decreases much faster in the forest case than in the non-forest case.

Using the correlation function of windwise velocity fluctuation, the windwise integral length scale (Lu_x or simply just Lu) is defined as follows:

$$Lu = Lu_x(z) = \int_0^\infty Ruu(z, x)dx. \qquad (3.5.4)$$

Two different methods of the integral length scale calculation were considered. First of all, the direct integration of the correlation function (see equation above) was used. This approach has a drawback related to the fact that the present Ruu_x decrease to the negative values at large r_x. Thus, it is known in advance that the integral length scale calculated in this way is underestimated. The second way of calculating Lu is to use a threshold value for Ruu_x, for example 0.1. Then, values of $Lu(z)$ are given by the intersection point of $Ruu_x(z)$ and the threshold value for every z. This method is very sensitive to the choice of the threshold value. Both methods show a similar behaviour of Lu with respect to each other. The difference is only in the size of the length scale. It is mentioned above that in the direct integration method, the length scale is underestimated. Thus, it was decided to integrate only the positive part of Ruu_x (that is, until autocorrelations cross zero the first time) in the present study.

Figure 3.5.4 shows the windwise integral length scale for the cases without and with forest. Similarly to the behaviour of the autocorrelation function, without presence of forest the values of Lu at first ($z/H < 0.5$) increase and then decrease ($0.5 < z/H < 1.5$) and increase again ($z/H > 1.5$) with an increase in the vertical coordinate. In the case of forest, $Lu = 0.55D = 2.97h$ at the canopy top, which is close to the wind-tunnel value of $Lu = 2.8h$ from Shaw et al. (1995). Then Lu increases with the increase in the vertical coordinate up to $Lu = 2.1D$ at $z = 1.8H = 162$ m. Above $z = 1.8H$, the length scale decreases in both cases. However, it may be unphysical because of the influence of the top boundary. In both cases, turbulence structures at the turbine hub height are larger than the diameter $D = 108$ m of the virtual turbine ($Lu = 1.4D$ and $Lu = 1.9$ in the forest and non-forest cases, respectively).

Figure 3.5.4 (right) shows the comparison of the LES-predicted length scale and the lines taken from Counihan (1975). Lu from the forest case corresponds to the strongly rough to rough conditions and Lu from the non-forest case corresponds to the slightly rough condition below a certain height ($z < 60$ m). However, the results of the simulations are

not supposed to directly follow the empirical law, e.g. because the empirical law may have been calibrated for different types of roughness. Thus, the obtained deviation seems to be reasonable.

As forest makes the integral length scale smaller, it is clear that for a given mean wind speed, the time scale of the dominant turbulent structures also becomes smaller, and thus the dominant aerodynamic loads on the blades not only increase in magnitude but also occur at higher frequencies. This may shorten the fatigue life of the turbine. The ratio between the integral length scale at the lower and upper tip $Lu|_{z/H=1.6}/Lu|_{z/H=0.4}$ is approximately 2 in the forest case. However, in the case without forest, the ratio is close to one ($Lu|_{z/H=1.6}/Lu|_{z/H=0.4}$=0.8). This indicates that the turbulence structures in the forest case are very different across the rotor disk. Therefore, the frequency of the loads also varies over the rotor area.
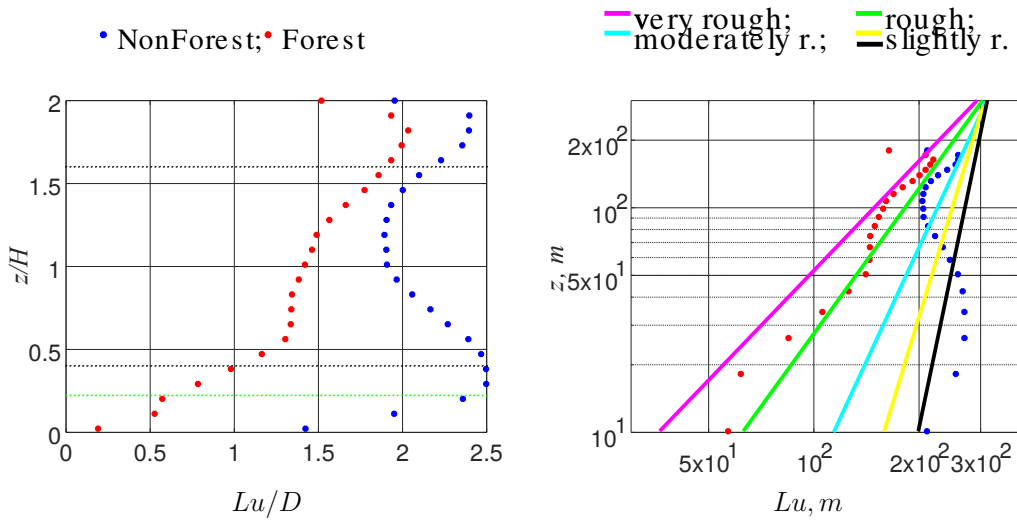

Figure 3.5.4: Calculated vertical distribution of the windwise integral length scale Lu for non-forest and forest cases compared to the empirical data (Counihan, 1975), which are represented by lines. The pink colour corresponds to strongly (very) rough, green to rough, cyan to moderately, and yellow and black to slightly rough conditions.

One-dimensional spectra for the cases with and without forest are seen in Figure 3.5.5. The velocity spectra from the non-forest case show a slope of -1 over the region $10^{-3} < k_x < 10^{-1}$; then they scale with the expected slope of -5/3 at a small region $k_x < 3 \cdot 10^{-1}$ and finally decay with k_x^{-5}. The very first curve (corresponds to the energy spectrum taken at $z = h/2$) has a slightly different slope. Following the turbulence intensity, the values of the energy spectrum E_x decrease with the increase in the vertical location in the case without forest. The maximum value of the energy spectra $E_x = 6 \cdot 10^3$ is reached above the ground at $h/2 < z \leq H - R$ and at the very low wave number k_x (where $k_x = 2\pi[-n_x/2 : n_x/2 - 1]/L_x$; n_x is the number of nodes in the windwise di-

rection and L_x is the length of the domain).

Similarly to non-forest case, in the case of forest E_x has a less steep slope (-1) at $10^{-3} < k_x < 3 \times 10^{-2}$ and steeper slope at $k_x > 5 \times 10^{-1}$ than -5/3 and decreases with increasing the vertical location above the forest ($z > h/2$). However, in the forest case, E_x better scales with -5/3 ($3 \times 10^{-2} < k_x < 5 \times 10^{-1}$). The more rounded shape of the spectra at the middle wave numbers in the forest case suggests that a significant part of the energy at low wave numbers is moved to the middle range by the effect of forest. The line inside the forest has a different curvature and does not scale with -1 and scales with -5/3 slope only on a short region ($4 \times 10^{-2} < k_x < 10^{-1}$). The maximum value of energy spectra $E_x = 3 \times 10^4$ in the forest case is obviously higher than it is without the forest. $E_x = 3 \times 10^4$ is reached at $z = H, z = H - R/2, z = H - R$ and $z = 1/3h$ and at low wave number k_x. That is five times higher than in the non-forest case. The maximum value inside the forest is smaller than the ones obtained above the forest because the turbulence inside the canopy is damped by the forest. The reason why the present one-dimensional energy spectra do not follow -5/3 slope but decay with -5 slope is probably that they decay because of high numerical dissipation.

Let us consider the higher order statistics of turbulence, the skewness Sk and flatness Fl. The skewness Sk_{u_i} of any instantaneous velocity component u_i is calculated in each layer using spatial averaging, as follows:

$$Sk_{u_i} = \frac{\langle u_i'^3 \rangle}{\langle u_i'^2 \rangle^{3/2}}.$$ (3.5.5)

The flatness Fl_{u_i} of any velocity component u_i is calculated in each layer using spatial averaging, as follows:

$$Fl_{u_i} = \frac{\langle u_i'^4 \rangle}{\langle u_i'^2 \rangle^2}.$$ (3.5.6)

Figure 3.5.6 shows the skewness for the forest and non-forest cases and the corresponding reference data from Nebenführ and Davidson (2014). It could be seen from the figure that the obtained skewness of windwise velocity Sk_u is negative but small ($Sk_u > -0.45$) almost everywhere (except the first two points) in the case without forest. This is contrary to the reference data (Nebenführ and Davidson, 2014), which shows positive Sk_u everywhere. However, the obtained skewness of vertical velocity component Sk_w is negative inside the forest (minimum value $Sk_w = -0.3$) and then continuously increases and becomes positive above $z = 0.7h$.
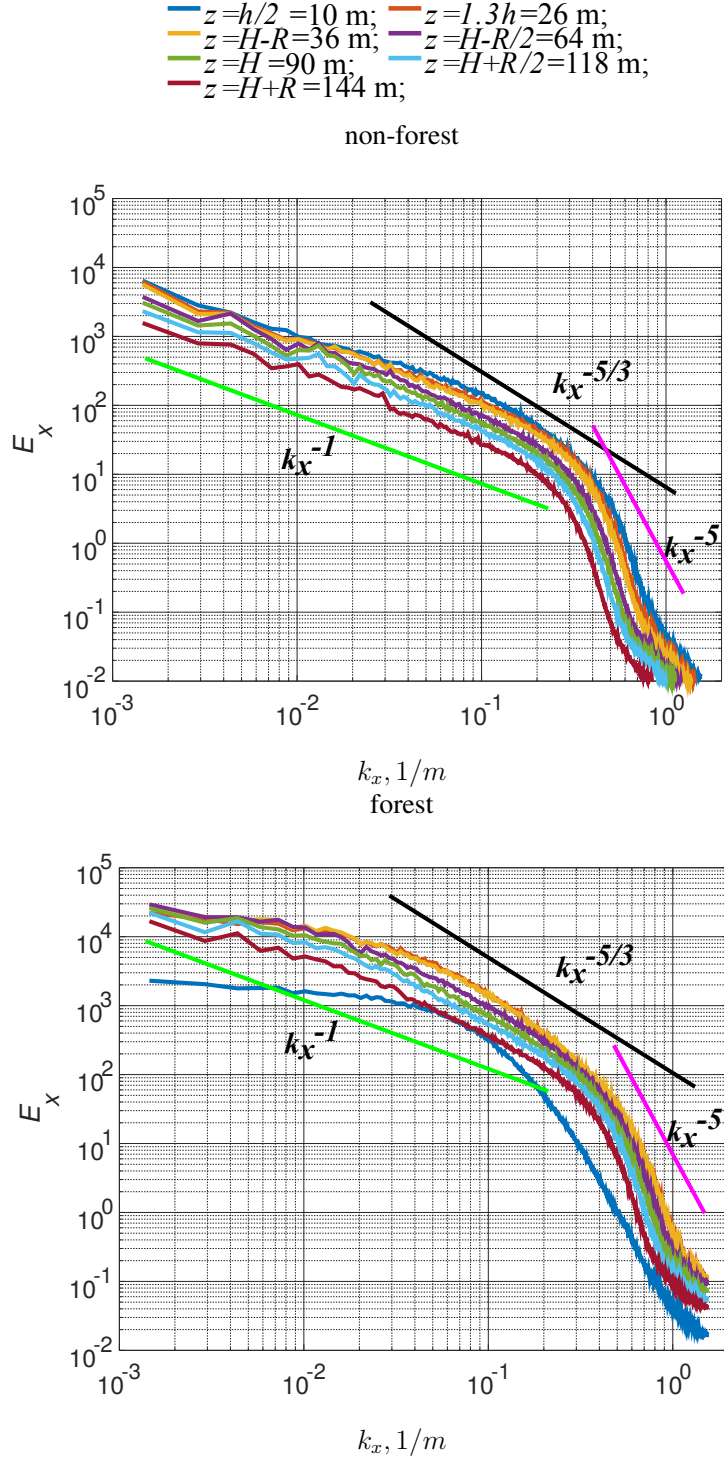
Figure 3.5.5: One-dimensional spectra (E_x) calculated for non-forest and forest cases at different vertical locations. Green, black and magenta colours denote the k_x^{-1}, $k_x^{-5/3}$ and k_x^{-5} lines, respectively.

However, the skewness Sk_u in the forest case is positive inside the forest and becomes slightly negative above the canopy top ($z > 2h$). The reference data (Nebenführ and Davidson, 2014) have a similar behaviour, but the skewness becomes negative higher above the canopy top ($z = 5h$). The difference can be due to the different grid resolution. The reference case has 8 m, 8 m and from 2 m to 5 m resolution in the x, y and z directions, respectively, but the present case has uniform 2 m resolution in all directions. At the same time, the maximum value of the Sk_u in the present case with the forest ($Sk_u = 0.71$) differs from the one from the reference case ($Sk_u = 0.9$). In contrast to Sk_u, the skewness of vertical velocity component (Sk_w) starts with a negative value of about $Sk_w = -0.6$ inside the forest and then increases to a positive value of $Sk_w = 0.1$ at two heights of the forest.

Figure 3.5.7 represents the flatness distribution of windwise and vertical velocity components and reference data (Nebenführ and Davidson, 2014) for the windwise component for both non-forest and forest cases. It can be seen from Figure 3.5.7 for the non-forest case that the profile of Fl_u has small variations around its mean value (approximate 2.7). However, the reference profile of flatness Fl_u has a larger deviation around its average. The other component of velocity is distributed around a value of about 3. It is known that the flatness of the Gaussian distribution is equal to 3. In the forest case, Fl_u has a maximum value of 3.6 at position $z = 0.8h$ and an average of about 3. In the reference study, a similar behaviour is also observed. Reference Fl_u has a peak at $z = 0.9h$, but the value of the peak is equal to 4.2. The stronger peak in the reference case can be due to different densities of the forest. This observation qualitatively agrees with the other numerical studies, for example in Dupont and Brunet (2008b), the wind tunnel experiment (Raupach et al., 1986) and field measurements by Dupont and Patton (2012).

In addition to the Sk and Fl for cases F12d9h2/C12d9h2 (LAI=2), the skewness and flatness are calculated also for the cases with a higher domain F4d22h4/C4d22h4 (LAI=4.3) in order to see how the upper boundary condition and the different LAD affect the skewness and flatness. As one can see from the figures, the values are indeed affected by the upper boundary. However, the differences appear mostly at heights $z > 3 - 4h$. The magnitudes of the skewness and flatness are overestimated above $z > 3 - 4h$ in the case of the smaller domain height. The peaks in the Sk_u and Fl_u are the same for the shallow and high domains and seem to be not affected by the different leaf-area density of the forest. Moreover, Sk_u and Fl_u are far from the reference values (Nebenführ and Davidson, 2014). The main difference between the cases and the reference is the grid size. In the present study, $\Delta x = \Delta y = \Delta z = 2$ m, while Nebenführ and Davidson (2014) performed LES at an approximately 8 m resolution grid. Thus, the flatness and skewness of the velocity seem to be sensitive to the height of the domain mostly at the upper part of the domain and highly sensitive to the grid resolution everywhere in the domain.

Figure 3.5.6: Skewness Sk_u and Sk_w of windwise and vertical components of instantaneous velocity, respectively, calculated for the non-forest and forest cases compared with the reference results. Blue colour denotes the reference data (Nebenführ and Davidson, 2014).
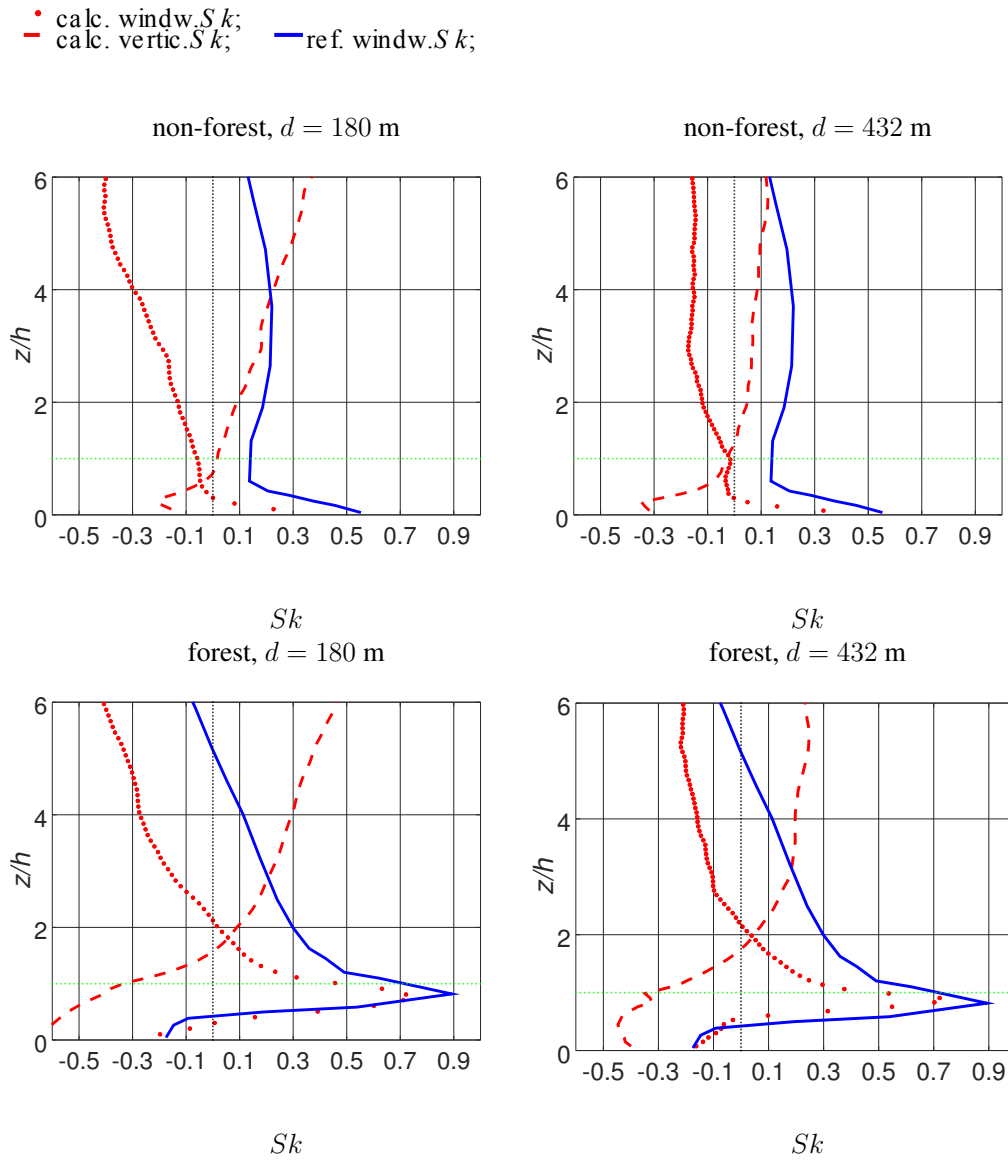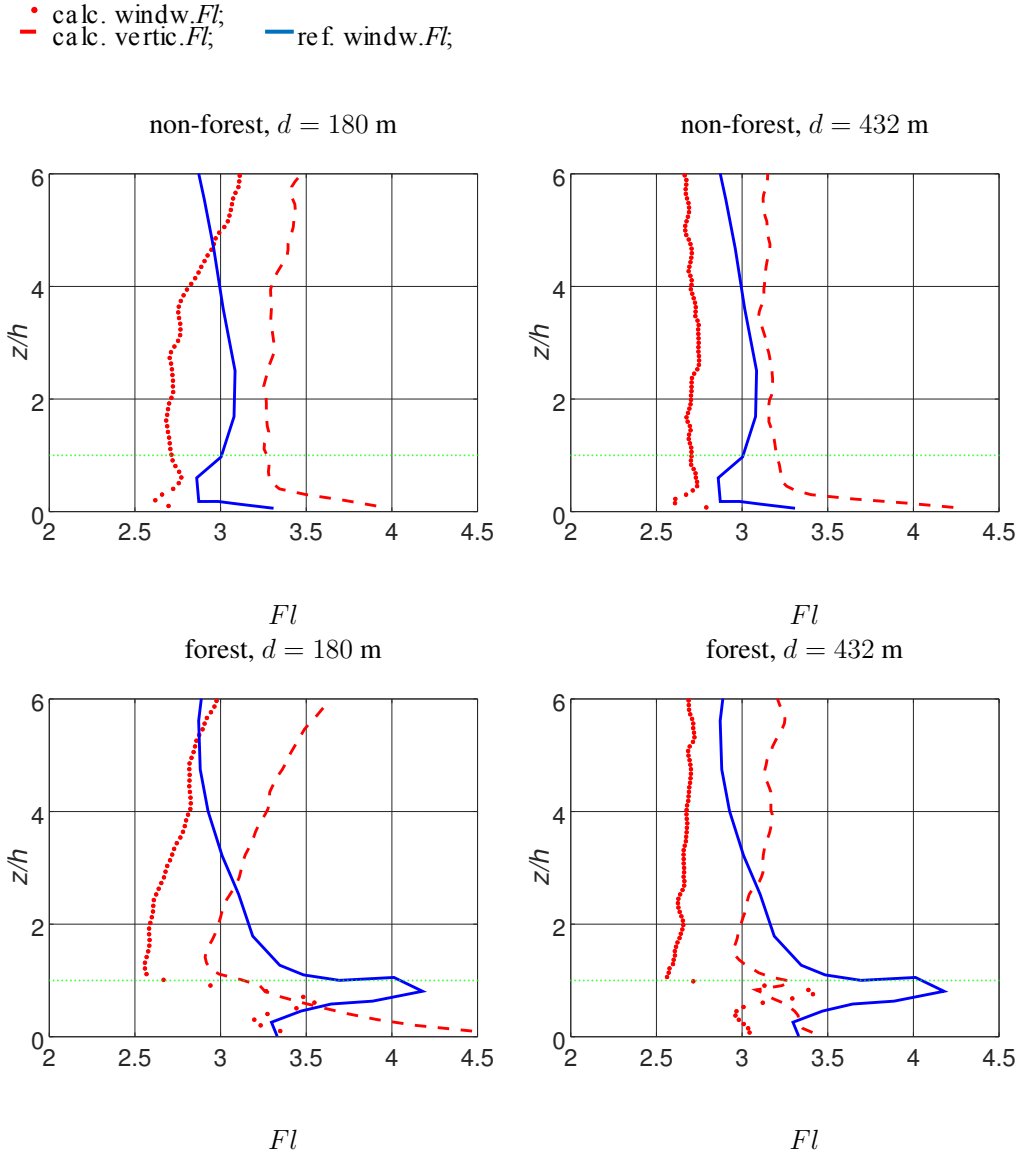
Figure 3.5.7: Flatness Fl_u and Fl_w of windwise and vertical components of instantaneous velocity, respectively, calculated for the non-forest and forest cases compared with the reference data. Blue colour denotes the reference data (Nebenführ and Davidson, 2014).

Chapter 4

Turbine modelling

4.1 Introduction

Since the computational capacity of modern computers is increasing, the number of different numerical methods to model wind turbines is also increasing. Every approach has its positive and negative sides and own application area. For example, CFD with full rotor geometry resolves the full rotor blade boundary layer. Thus, it captures detailed tip and root vortices near the blade.

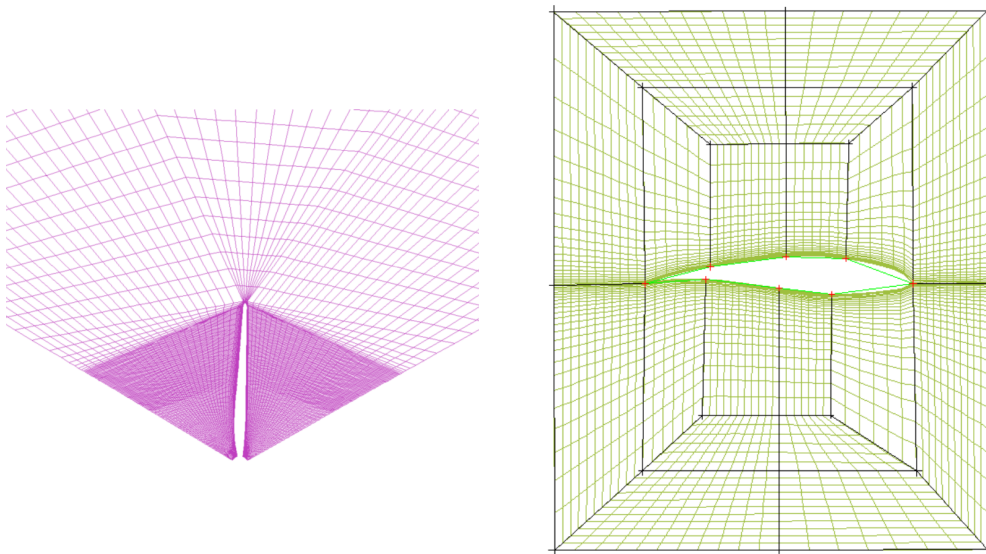Figure 4.1.1: Cut plane of computational grid along rotor axis (left) and around an airfoil (right) (Perfiliev et al., 2013).

At the same time, it only solves the local flow field around the blade and does not solve the far-wake flow and does not consider terrain-to-wake interaction. Moreover, the use of this method is computationally extremely expensive because of the very fine grid-resolution

requirement in the boundary-layer region. According to Jin (2013), one simulation can take 33 600 CPU hours. An example of a 3D boundary layer grid for one blade taken from Perfiliev et al. (2013) is shown in Figure 4.1.1.

4.2 Actuator Disk Approach

In the above-mentioned study, computations are performed over only one blade and then the full solution is obtained by merging 120° rotationally periodic solutions of one blade. Therefore, this approach is good to use in a small scale, such as, in tasks related to the search for an optimal turbine (blade) design (Perfilev, 2013). On the other side, there are methods based on adding extra body force to the momentum equation. The force calculated from the aerodynamic load is distributed between the turbine-blade or rotor-disk cells. The method called the Actuator Disk Model (ADM) can be used in 2D/3D steady simulations. It requires a better grid resolution in the disk area because the load is calculated directly in the disk cells. The body force is distributed uniformly in the simple ADM (Calaf et al., 2010). In the present work, the advanced ADM (ADM-A) was tested. ADM-A was developed and implemented in OpenFOAM® by Svenning (2010). In the advanced approach, the body force is a function of the radial coordinate. To calculate the body force in ADM-A, it is necessary to know the incoming wind velocity relative to the blades and to estimate thrust and torque (power) or thrust and power coefficients (C_T, C_P) (Svenning, 2010). The results obtained by running RANS with ADM-A are presented below in Figures 4.2.1 and 4.2.2.
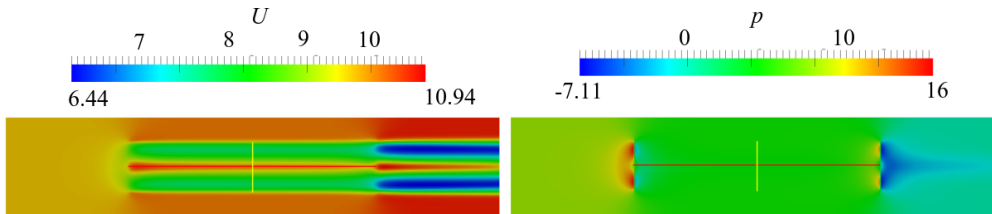
Figure 4.2.1: Side view of mean velocity magnitude (left) and pressure (right) for the case with two turbines installed in $5D$ distance between them simulated by RANS and the ADM-A approach.

One example of using RANS with ADM-A in a real wind park (for topography, see Figure 4.2.3) is presented in Figure 4.2.4. In this simulation, only two isolated wind turbines from the north side of the highway (shown in Figure 4.2.3) are considered. The dominant wind direction in this site, which is coming from the lake side (shown in Figure 4.2.3), is considered. As presented in Figure 4.2.4, in this wind direction, the downwind turbine is located not in the wake of the upwind turbine but about 15· aside from the wake, gains the velocity accelerated by the first turbine, and therefore produces more energy. The actuator disk approach seems to be a good and fast choice for optimization problems at a larger

Figure 4.2.2: RANS prediction for mean windwise, crosswind and vertical velocity (top), body force calculated by ADM-A in the area swept by the blades (bottom).

scale. For instance, it can be helpful for optimizing wind-turbine locations in a large wind farm.
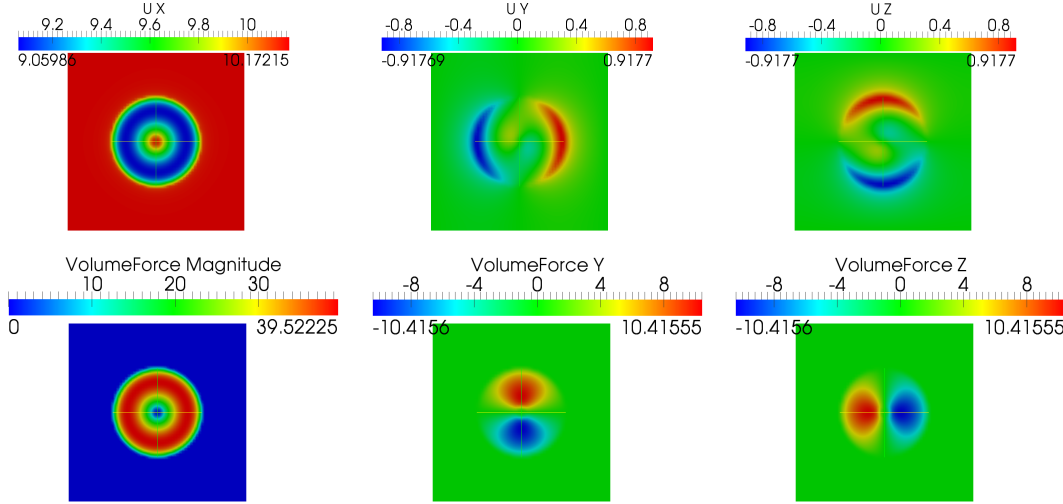
4.3 Actuator Line Approach

In tasks, where the details provided by explicit blade-resolving simulation are not necessary, but a model more detailed than ADM is needed, the best choice so far is the Actuator Line Method (ALM) (Sørensen and Shen, 2002; Troldborg et al., 2007, 2008; Jin, 2013). The ALM is thought to be more suitable for 3D unsteady CFD than the simple ADM. Several studies were performed recently to compare the methods like the standard ADM, rotating ADM (not the same as the ADM-A by Svenning (2010)) and ALM, Porté-Agel et al. (2011); Witha et al. (2014). They conclude that the standard ADM predicts the near-wake wind speed slightly less accurately than the ALM. Assuming that the ADM-A is also less accurate in wake-velocity deficit prediction in the near wake and taking into account the fact that the ADM is not able to resolve the wind flow around the blades, the ALM is chosen for modelling wind turbine in the present research work. Moreover, the possibility to study the forest effects on the fatigue of the blades and angle of attack is given by the output of the ALM . The detailed description of the ALM used in the simulations to be presented in the thesis, is specified below. The OpenFOAM® implementation of ALM, made by NREL (SOWFA, Churchfield et al. (2012a,b)), is found to be accurate (Churchfield et al., 2012b; Panjwani et al., 2014; Martinez-Tossas et al., 2015) and fast enough. Therefore, the results presented in this study are obtained using SOWFA.
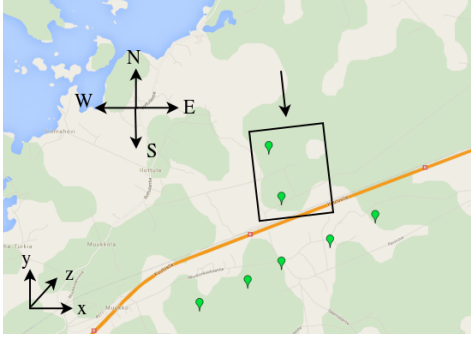
Figure 4.2.3: Local map of wind-park site (located in Finland) studied by ADM-A
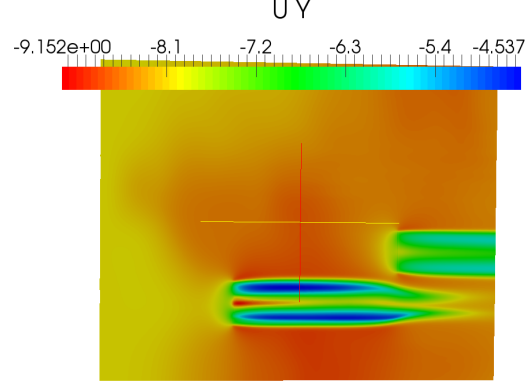
Figure 4.2.4: RANS prediction (using ADM-A) of wind velocity for two isolated wind turbines from Figure 4.2.3

In the ALM, local aerodynamic forces $f_a^{\theta,z}$ are calculated in points along the virtual actuator lines using the Blade Element Momentum approach (BEM, Froude (1878); Troldborg et al. (2008); Perfilev (2013); Abedi (2013)) combined with tabulated two-dimensional airfoil characteristics, such as lift and drag coefficients ($C_l(\alpha, Re)$ and $C_d(\alpha, Re)$, respectively), chord length ($c(r)$), twist ($\psi(r)$) and pitch (φ) angles. $Re = U_{ref}c/\nu$ is the Reynolds number based on chord length, r is the radial coordinate. A cross-section of the blade at radius r in the (θ, z) plane is presented in Figure 4.3.1, where θ is the azimuthal angle. Figure 4.3.1 shows the angular velocity Ω, velocity components in the axial and azimuthal directions, V_z and V_θ, respectively, and force vectors: lift (L) and drag (D). The local velocity relative to the rotating blade (V_{rel}) is determined from the Figure 4.3.1 as

$$V_{rel} = \left(V_z^2 + (\Omega r - V_\theta)^2\right)^{1/2} \tag{4.3.1}$$

Thus, the angle between V_{rel} and the rotor plane (the flow angle, ϕ) is equal to:

$$\phi = \tan^{-1}\left(\frac{V_z}{\Omega r - V_\theta}\right). \tag{4.3.2}$$

The local angle of attack is given by $\alpha = \phi - \gamma$, where γ denotes the collective angle (or local pitch) which is the sum of the mounting pitch (φ) and the design twist ($\psi(r)$) angles. Thus, the lift and drag forces can be found using the angle of attack and the relative velocity as:

$$L = \frac{1}{2}\rho V_{rel}^2 cC_l, \tag{4.3.3}$$

$$D = \frac{1}{2}\rho V_{rel}^2 cC_d. \tag{4.3.4}$$

Therefore, the local axial (f_a^z) and azimuthal (f_a^θ) to the rotor plane aerodynamic forces are calculated as projections of the lift and the drag forces onto the normal and tangential
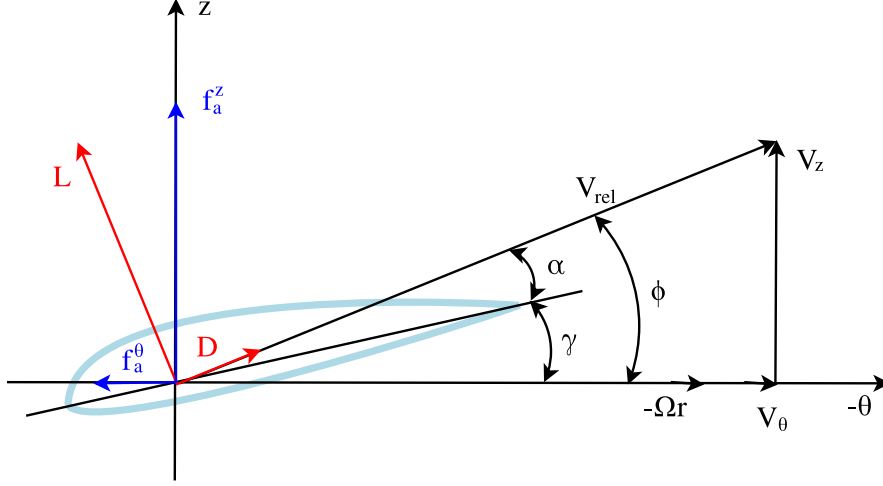
Figure 4.3.1: Airfoil which shows definition of velocity and force vectors (Sørensen and Shen, 2002; Troldborg et al., 2007)

directions:

$$f_a^z = L\cos(\phi) + D\sin(\phi), \tag{4.3.5}$$

$$f_a^\theta = L\sin(\phi) - D\cos(\phi). \tag{4.3.6}$$

The calculated aerodynamic forces f_a then have to be distributed (smeared) into the grid cells (f_T) surrounding each point using 3D Gaussian distribution by taking the convolution of the computed local force, f_a, and a regularization kernel η_ε (Jin, 2013; Sørensen and Shen, 2002; Troldborg et al., 2007, 2008):

$$f_T = f_a \otimes \eta_\varepsilon, \ \eta_\varepsilon(d) = \frac{1}{\varepsilon^2 \pi^{3/2}} \exp\left[-\left(\frac{d}{\varepsilon}\right)^2\right] \tag{4.3.7}$$

where $d = |x - x_i|$ is the distance between cell-centred grid points x and the actuator line points x_i and ε is a parameter which is used to adjust the concentration of the regularized load.

In other words, in order to smear the forces, the following steps can be performed (see Figure 4.3.2):

- define ε;

- for all blades, for all line points x_i do:

- find the sphere $S(x_i, r(\varepsilon))$ with a radius which is a function of ε surrounding the line point x_i, r is chosen in such a way that the regularization kernel $\eta_\varepsilon(d)|_{d=r}$ becomes very small $\left(\exp\left[-(r/\varepsilon)^2\right] = 0.001 \text{ in the present study}\right)$,
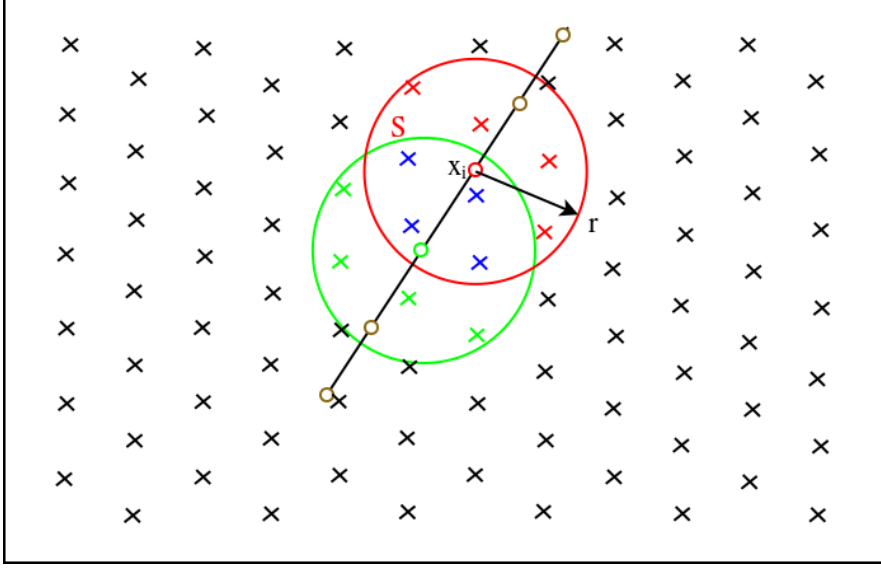
Figure 4.3.2: Sketch of the smearing algorithm. Green colour represents the points x which belongs to the sphere $S(x_{i-1}, r)$, red represents the points belonging to the current sphere $S(x_i, r)$ and blue represents the points where smearing is applied two times.

- find the grid cells x which belongs to the sphere S,

- apply the correction $f_T = f_a \eta_\varepsilon$.

The purpose of this smearing is to distribute the forces and do it in such a way to avoid numerical instability. Such smearing is not present in the ADM-A. The main advantage of the ALM in comparison with the standard and advanced actuator disk approaches is that the blade aerodynamics is taken into account by BEM. The influence of the parameter ε will be studied below.

The turbine source term obtained by the actuator line method also creates a restriction on time-step size by the tip-speed ratio of the rotor. The movement of the blade tip during one time step should not exceed one grid spacing; then the minimum number of time steps per rotor revolution (according to Troldborg et al. (2008)) should be greater than $2\pi R/\Delta x$. Therefore, the Courant number is limited to the maximum value of 0.25 for every simulation considered in the present study.

An example of the results calculated by LES with the ALM are presented below in Figures 4.3.3, 4.3.4 and 4.3.5. Details of the simulation can be seen in Section 4.5. It can be seen from Figure 4.3.3 (left) that the ALM gives a quite detailed structure of the wake.

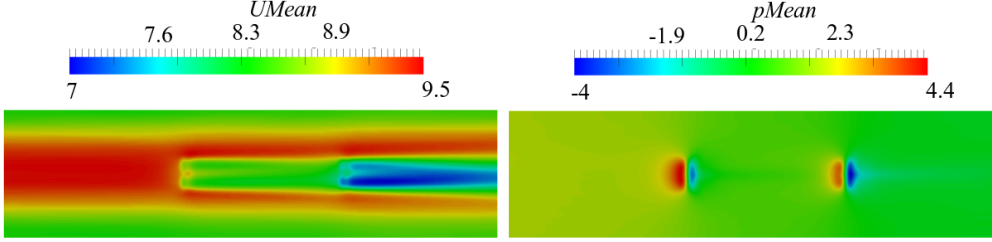Figure 4.3.3: Top view of mean velocity magnitude (left) and pressure (right) for the case with two turbines installed in $5D$ distance between them at $z = 90$ m.
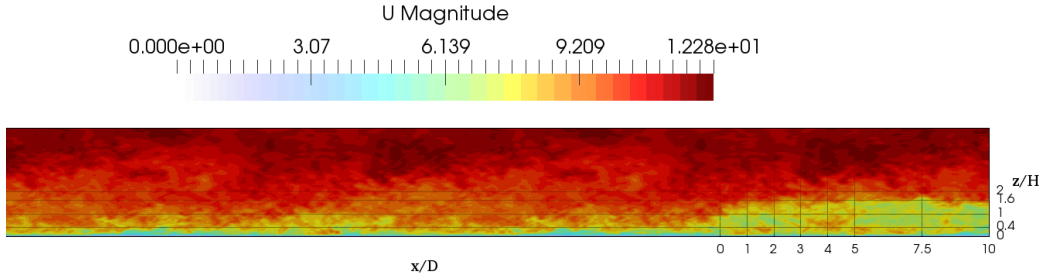
Figure 4.3.4: Side view of instantaneous velocity magnitude for the case with two turbines installed in $5D$ distance between them at $y = 0$ m.

4.4 ALM: Validation

At first, the ALM is validated by simulating the flow past a single wind turbine. The corresponding wind-tunnel experiment is described by Chamorro and Porté-Agel (2009). The miniature turbine uses a three-blade GWS/EP-6030×3 model airplane propeller as rotor (see Figure 4.4.1) and is connected to a small generator to control the turbine rotation. The wind turbine with the hub height $H = 0.125$ m and the rotor diameter $D = 0.15$ m from Chamorro and Porté-Agel (2009) was modelled in the simulations. The computational domain has a length of 9.15 meters, a width of 0.9 meters and a height of 0.45 m. That is, $L_z = d = 3D, L_y = 2d = 6D$ and $L_x = 20.33d = 61D$, of which the first $10.33d$ is used for mapping the flow (see Chapter 2), the next $6.67d$ is a buffer zone and the rest of the domain ($3.33d = 10D$) is the area of interest, that is, where the turbine and the wake produced by the turbine are located. The tip-speed ratio $\lambda = \Omega D/(2U_h)$ is about 4.0. The inflow velocity profile is taken according to the inflow velocity from the experiment. The inflow velocity at hub height is 2.9 m/s.

The airfoil Reynolds number ($Re = V_{rel}c/\nu$), where V_{rel} is the relative velocity and c is chord length, varies between $4 \cdot 10^3$ and $7 \cdot 10^3$ along the radial position. The computational grid is uniform in all directions ($\Delta x = \Delta y = \Delta z$) and created using the "blockMesh" utility in OpenFOAM®. The grid resolution for different cases is described in Table 4.4.1. The airfoil properties from the experiment are not known. The Reynolds number in the
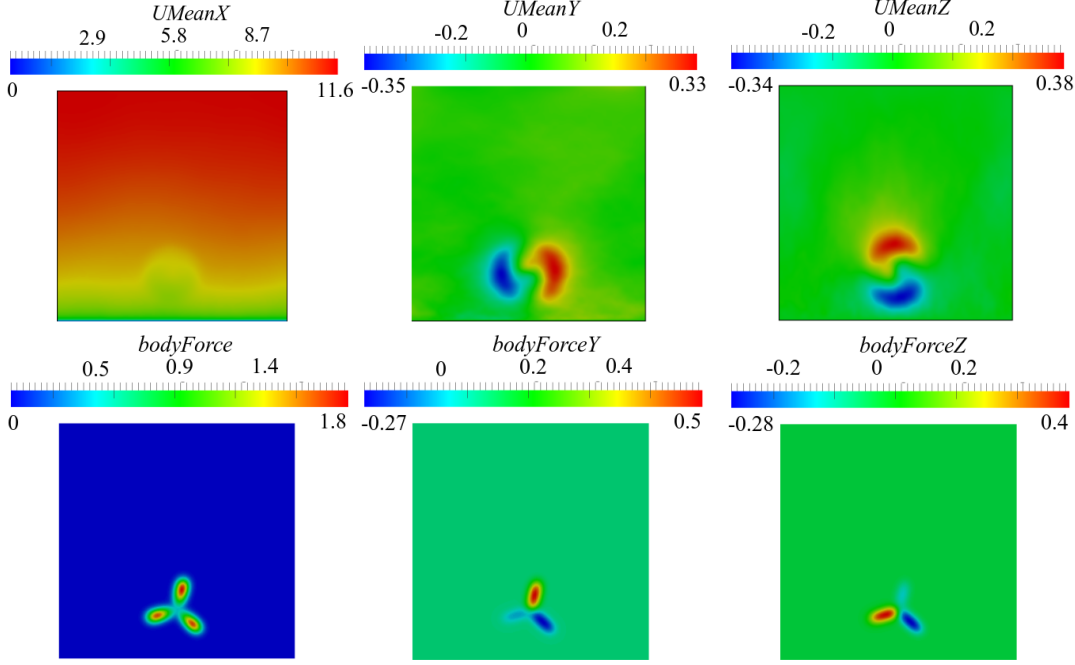
Figure 4.3.5: LES prediction for mean windwise, crosswind and vertical velocity (top), body force calculated by ALM in the swept area of the blades (bottom).

measurements by Sunada et al. (1997) was 4000 which is approximately equal to the one in the wind-tunnel study of Chamorro and Porté-Agel (2009). Because of the lack of airfoil lift and drag coefficient data available at such a low Reynolds number, the flat-plate data from Sunada et al. (1997) is also used in the present study, following Wu and Porté-Agel (2011); Yang et al. (2014). The chord length and twist angle of the blade at different radial locations of the turbine blade are taken from Wu and Porté-Agel (2011). The so-called nacelle model from Wu and Porté-Agel (2011) is applied. However, it is found from Figure 4.4.1 that the airfoil upper surface is curved, which means that airfoil has a variable thickness. Often these propellers' airfoils are also slightly cambered; thus the airfoil cannot be of the flat-plate type in reality. Since the real propeller probably has different lift and drag coefficients from flat-plate, one should not expect an excellent agreement with the experiment as such. The very first simulation with the assumptions of flat-plate airfoil data from Sunada et al. (1997) and the chord length and twist angle from Wu and Porté-Agel (2011) did not give good agreement with the experiment as expected. More specifically, the thrust coefficient

$$C_T = \frac{T_{actual}}{1/2\pi R^2 U_h^2},\tag{4.4.1}$$

where C_T is the thrust calculated by the ALM, was surprisingly low: $C_T = 0.35$. A typical value of $C_T = 0.6$ for the real-scale turbines, but it is uncertain how good this assumption

is for the modelled miniature wind turbine. The variation in different parameters, such as the grid resolution and the smearing coefficient ε, did not change the thrust significantly. Next, the angle of attack α was considered and found to be too low to give the above-estimated thrust with aerodynamic data of flat-plate. Finally, the variation of the mounting pitch angle φ allowed to get the estimated actual thrust. The appropriate mounting pitch is found to be $\varphi = -10^o$.

Therefore, this wind-tunnel experiment, especially because of the lack of wind turbine data, can not be a real validation case. However, other authors have used it for validation (Wu and Porté-Agel, 2011; Yang et al., 2014). In the present study, it is seen as a combination of calibration and validation rather than pure validation. On the other hand, SOWFA's ALM was already validated, for example, by (Churchfield et al., 2012c; Panjwani et al., 2014; Martinez-Tossas et al., 2015).

Figure 4.4.1: Side view of GWS/EP-6030$\times$3 propeller used to represent a turbine rotor in the wind-tunnel experiment.
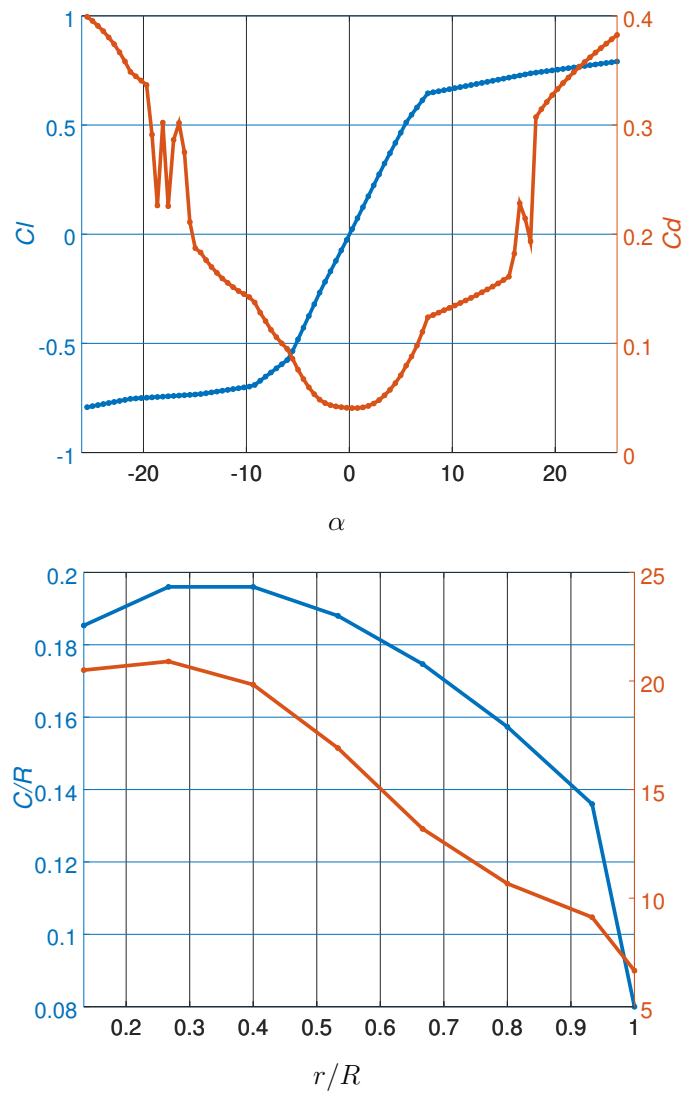
Figure 4.4.2: Lift and drag coefficients (Sunada et al., 1997) for the flat-plate airfoil (top) and the chord length and twist angle (bottom) of the miniature wind turbine (Wu and Port´e-Agel, 2011).

Table 4.4.1: Description of the cases with one wind turbine, which are compared to the experimental data.

	Δx, m	$D/\Delta x$	ε
T1n4m1	0.0056	27	Δx
T1n4m1	0.0056	27	Δx
T1n4m2	0.0056	27	$2\Delta x$
T1n4m4	0.0056	27	$4\Delta x$
T1n2m4	0.0028*	54	$4\Delta x$
T1n8m4	0.0112	13.5	$4\Delta x$

*At the first step, the grid has 0.0056 m resolution and consists of $1646 \times 161 \times 93$ finite volume cells. However, the region $-D \leq x \leq 10D, -D \leq y \leq D$ and $z \leq 2D$ m is refined to 0.0028 meters in every direction. Thus, 54 cells per rotor diameter in $-D \leq x \leq 10D$.

First of all, the obtained results are quantitatively compared with the experimental data. The LES prediction for different grid resolution and different smearing parameter ε and experimental data for normalized mean windwise velocity U/U_h deficit (DU) at $x/D = 2$ and $x/D = 10$ are presented in Figure 4.4.3, where the deficit of the normalized mean windwise velocity DU is defined as:

$$DU = \frac{U^{inflow} - U^{wake}}{U^{inflow}} \qquad (4.4.2)$$

First, it can be seen from Figure 4.4.3 (left) that in almost all cases (except the case T1n4m4) the obtained velocity deficit is far from the measured at $x = 2D$. The cases T1n4m1 and T1n2m4 have the worst results. Their rough wake shape also differs from the smooth experimental shape. Perhaps, the case with refined grid (T1n2m4) has poor agreement because of the improper choice of ε. Second, the velocity deficits calculated on the same grid of 0.0056 m resolution and with different ε ($= \Delta x,\ 2\Delta x$ and $4dx$) have three different shapes of the wake and different maximum values at hub height. The case with the largest ε gives a longer wake in the windwise direction. An excellent agreement is obtained in the T1n4m4 at $x = 2D$. The relative error is less than 1% (see Table 4.4.2). In cases of an insufficiently large ε, arbitrary loads at discrete grid cells may occur when distributing the forces calculated in the line points onto the flow field as body forces. Next, LES in the case T1n8m4 underestimates DU by 24.2% in comparison to the experimental data. Low grid resolution (the very coarse grid, Δx=0.0112 m) and thus the numerical error can be the cause of the width of the wake in vertical direction (see Figure 4.4.3 (left)).

At last, no one of the performed cases has good agreement with the experiment in the region under the lower tip ($z < H - R$) at $x = 2D$, most probably because no tower model is used in the present study. However, Yang et al. (2014) also got the wake overestimation in that area even though they have used a tower model.

Figure 4.4.3 (right) shows the mean windwise velocity deficit at $x/D = 10$. The LES in the case T1n4m1 underpredicts the velocity by 1.8%. However, the LES overpredicts

the velocity from the experiment in the cases T1n4m2, T1n8m4 and T1n4m4 by 0.9%, 2.8% and 5.2%, respectively. The velocity deficit in the case of T1n2m4 (refined grid) also underpredicts the velocity (by 1.3%), but the wake's shape in this case is closer to the experimental one.

It is worth to notice that the inflow velocity is underestimated by the LES in all the cases because of the error during the digitalization of the experimental data from Chamorro and Porté-Agel (2009). The error of digitalization is approximately 1%.

The LES in the case T1n4m4 has good agreement with the experiment. The maximum relative error in that case consists of 5.1%-5.2% for the positions: $x = 5D$, $x = 7D$ and $x = 10D$. In the other two positions, LES follows very closely the experimental data. Some overestimation of U can naturally happen in this case because of the coarse grid resolution and the absence of a tip/root correction. That is, the real tip-root losses are not considered by the present ALM and this study.

Figure 4.4.3: LES prediction for different grid resolution and different smearing coefficient ε vs experimental data (Chamorro and Porté-Agel, 2009) for normalized mean-velocity deficit (DU) at positions $x = 2D$ and $x = 10D$. The experimental data are digitally extracted from Chamorro and Porté-Agel (2009).

Figure 4.4.4 shows the mean windwise velocity deficit $\Delta U = (U_h - U^{wake}(x, 0, H))/U_h$ and turbulence intensity excess $\Delta I = (I^{inflow}(x, 0, H) - I^{wake}(x, 0, H))/I^{inflow}(x, 0, H)$ at $z = H$ as a function of the longitudinal coordinate (x), where turbulence intensity is defined as follows:

$$I = \frac{\langle u'u' \rangle^{1/2}}{U_h}. \tag{4.4.3}$$

The left figure shows that the LES in the case T1n4m4 very well agrees at the positions

$x = 2D$ and $x = 3D$. The relative errors in that case are 0.2% and 2.6%, respectively. However, the LES in the case T1n4m2 has the best agreement with the experiment at positions $5 \leq x \leq 10$. The relative error in that case is less than 3% (for three out of five positions). The results of the cases T1n4m1 and T1n2m4 have the worst agreement with the experimental data at almost every position. In the case of $\Delta x = 0.0056$ m T1n4m1, the disagreement can be because of too small $\varepsilon = \Delta x$. In the case of $\Delta x = 0.0028$ m T1n2m4 the disagreement can be also because of too small $\varepsilon = 4\Delta x$. It seems that ε should be greater than $4\Delta x$ in case of 0.0028 m resolution.

One can see from Figure 4.4.4 (right) that the results of the case T1n4m4 for the turbulence intensity deficit are not the best. However, the relative error for turbulence intensity in comparison to experimental data is relatively small (less than 6% for three out of five positions; see Table 4.4.3). The worst agreement is at the inflow plane and $x = 2D$ and equals 10.7% and 19%, respectively. It may be because the LES can not develop the same inflow turbulence as in the wind tunnel because of their specifics. The difference between the inflow in the simulation and the wind-tunnel experiment may also be due to the numerical disturbances from the turbines which come upstream to the mapping plane. The buffer zone length in $20D$ is long enough to prevent upstream disturbances from the wind turbine in mean wind speed but may not be enough for the turbulence intensity. The coarse grid can also be a reason for the difference in the turbulent intensity.
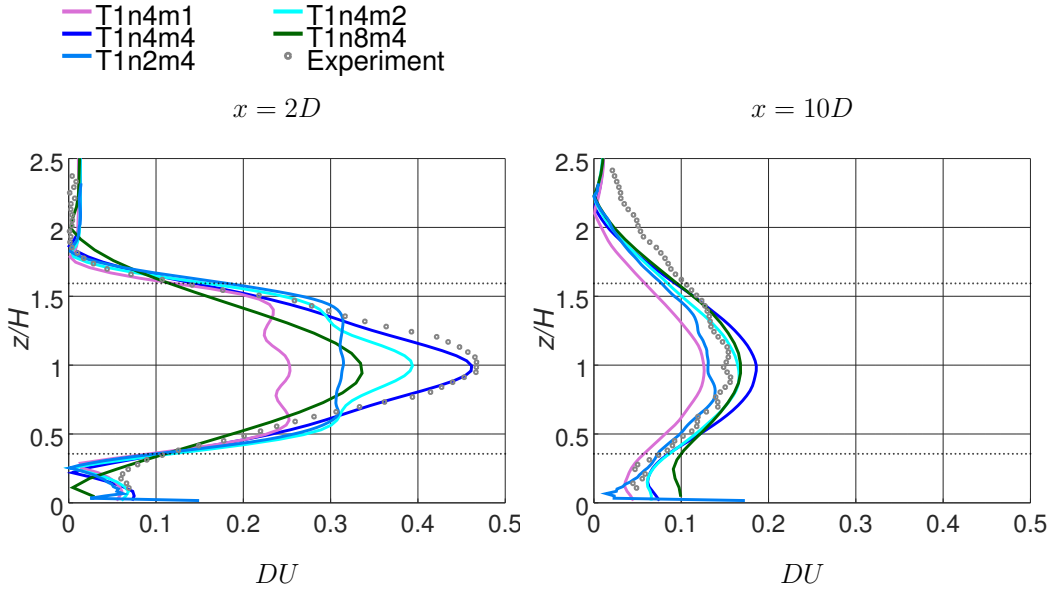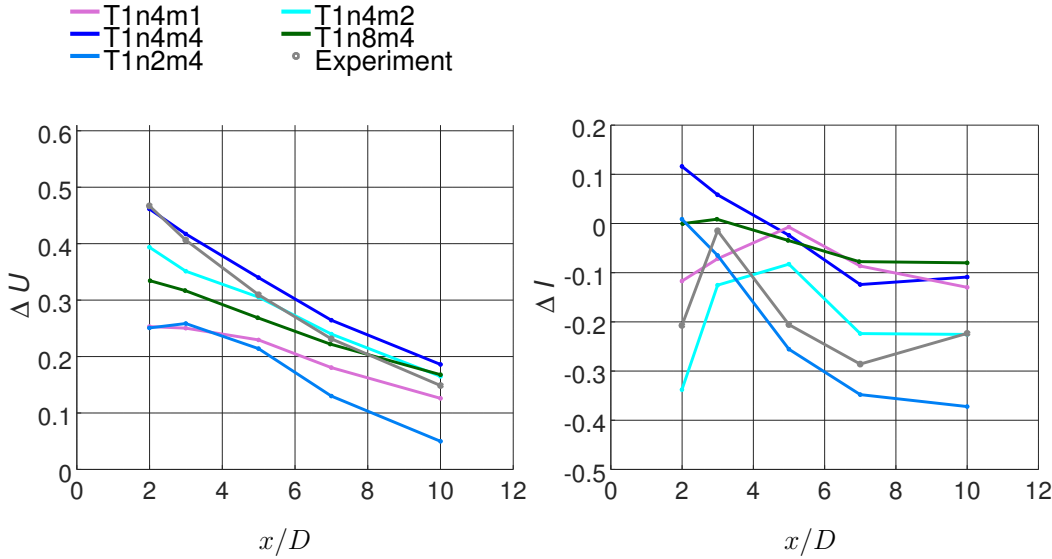

Figure 4.4.4: LES prediction for different grid resolution and different smearing coefficient ε vs experimental data (Chamorro and Porté-Agel, 2009) for velocity deficit ($\Delta U = (U_h - U^{wake}(x, 0, H))/U_h$) and turbulence intensity excess ($\Delta I = (I^{inflow}(x, 0, H) - I^{wake}(x, 0, H))/I^{inflow}(x, 0, H)$) at the hub height.

Table 4.4.2 shows the relative numerical error $(U^{LES} - U^{exp})/U^{exp}$ for time-averaged windwise velocity calculated on three different grids (very coarse, coarse and refined)

and using the smearing parameter ε of dx, $2dx$ and $4dx$. As seen from Table 4.4.2, the 0.0056 m resolution grid with $\varepsilon = 4dx$ gives the best prediction. It also has relatively good agreement for turbulence intensity (except the inflow and $x = 2D$, see Table 4.4.3). Therefore, overall the case T1n4m4 has the most accurate results. The results of this case are described below.

Table 4.4.2: Relative error for different U prediction at $z = H$.

	2D	3D	5D	7D	10D	Inflow
T1n4m1	39.0%	25.2%	10.7%	5.8%	1.8%	-0.81%
T1n4m2	12.8%	8.4%	-0.2%	-1.9%	-2.7%	-0.81%
T1n4m4	0.2%	-2.6%	-5.2 %	-5.1%	-5.2%	-0.81%
T1n2m4	27.6%	13.3%	3.3%	2.7%	1.3%	-0.81%
T1n8m4	23.9%	14.1%	5.0%	0.4%	-3.0%	-0.81%

Table 4.4.3: Relative error for different I prediction at $z = H$.

	2D	3D	5D	7D	10D	Inflow
T1n4m1	-7.9%	5.2%	-16.8%	-15.9%	-8.0%	-0.4%
T1n4m2	5.9%	6.0%	-14.2%	-9.0%	-4.2%	-4.4%
T1n4m4	-19.0%	2.7 %	-6.0%	-3.2%	0.3%	10.7%
T1n2m4	-21.0%	1.0%	0.2%	0.9%	7.9%	-3.8%
T1n8m4	-17.9%	-3.1%	-14.9%	-16.9%	-12.5%	-0.9%

As one can see from Figures 4.4.5, the present LES prediction of mean windwise velocity has an excellent agreement at the inlet and behind $2D - 3D$ downstream wind turbine. As shown in Table 4.4.4, it slightly differs ($\leq 5.2\%$) from the experimental data at positions $x = 5D$, $7D$ and $10D$ at the turbine hub height ($z = H$). At those positions, the wake is overestimated by LES. However, the obtained results have a better quality than the results published in Yang et al. (2014) for a flat-plate airfoil. The solution could be improved by using a different airfoil type (for example, a cambered one), applying extra tower model and tip-root corrections. Also, Figure 4.4.3 (left) suggests that the wind profile shape and wake strength could be possibly reached by applying the tower model (to have closer agreement near the lower tip), using an appropriate smearing coefficient (ε close to $4dx$ but perhaps slightly smaller to avoid the overestimation of the wake in the far-wake region) and a different grid resolution. In the present work, the obtained LES prediction is considered qualitatively good enough.

The windwise turbulence intensities at the inlet and behind the wind turbine are presented in Figure 4.4.6. As shown in Figure 4.4.6 and Table 4.4.5 the turbulence intensity obtained in the simulation at the inflow plane (inlet) differs by 22.7% from the one measured in the experiment because of the specific inflow conditions used in the experiment and simulation. The turbulence intensity may also be induced by the numerical noise from the

Table 4.4.4: Relative error for U prediction at upper, lower tip and hub height for the "best" case T1n4m4.

	2D	3D	5D	7D	10D	Inflow
$z = 0.4H$	0.3%	0.1%	-0.6%	-0.7%	1.1%	2.1%
$z = H$	0.2%	-2.6%	-5.2%	-5.1%	-5.2%	-0.8%
$z = 1.6H$	-1.7%	0.6%	-0.4%	-1.8%	0.1%	-1.4%

turbine. The turbulence intensity profile differs from the experimental one at $x = 2D$, most probably because of the coarse grid resolution ($D/\Delta x = 27$). Next, the LES overestimates the turbulence intensity at $x = 7D$ and $x = 10D$ downwind from the turbine, where the relative errors at the upper tip are 16% and 21.9%, respectively. The relative error at $x = 7D$ is very close to that at the inlet (22.7%). Thus, the LES overprediction of the turbulence intensities at other positions can be partly explained by the influence of the inflow. The other reason is the different velocity in the far-wake region (the wake overestimation in the rotor area at $x/D = 5, 7, 10$) and above the upper tip (the slight velocity overestimation at $x = 10D$ and $z > H + R(= 1.6H)$). Otherwise, the LES results follow the experimental profiles and the present LES predicts almost all peaks observed in the experiment for all downstream positions.

Table 4.4.5 shows the relative error for turbulence intensity prediction $(I^{LES} - I^{exp})/I^{exp}$ at the upper, lower tip, and hub heights. The largest relative errors are found to be at position $z = H$ (the maximum is equal to 31.4%) and the lowest ones are at $z = 0.4H$.

Table 4.4.5: Relative error for turbulence intensity prediction at upper, lower tip and hub height for the "best" case T1n4m4.

	2D	3D	5D	7D	10D	Inflow
$z = 0.4H$	-4.2%	-3.9%	-6.0%	1.2%	0.5%	-2.8%
$z = H$	-19.0%	2.7%	-6.0%	-3.2%	0.3%	10.7%
$z = 1.6H$	2.6%	2.3%	5.9%	16.0%	21.9%	22.7%

Figure 4.4.7 shows the comparison between the obtained and experimental vertical Reynolds shear-stress profiles ($-\langle u'w' \rangle /U_h^2$) at the inflow as well as at several downstream locations. As one can see, the computed LES prediction reasonably well matches the experimental data at the far wake. While at $x = 2D$ beyond the turbine, the LES predicts almost all peak locations from the experiment but strongly underestimates the magnitude of the vertical shear stress for them. Besides, the shape of the numerical result at $x/D = 3$ slightly differs from that observed in the experiment. The present LES predicts the shape of the experimental profile but underpredicts the magnitude of $-\langle u'w' \rangle /U_h^2$ at the upper tip at $x = 3D$ and $x = 5D$ and at the lower tip at $x = 3D$. However, the other LES study of the same case (Yang et al., 2014) overpredicts the experimental data for turbulence intensity and vertical shear stress at positions $x = 2D, x = 3D$ and $x = 5D$ downwind from the wind turbine on the refined grid. Then, at $x/D = 7$ and 10, the present simula-

tion overpredicts the magnitude of the vertical stress at both the upper and lower tip. The difference could be due to the turbine model defects (the absence of the tower model and tip-root corrections), as it is in the case of mean windwise velocity and turbulence intensity and therefore due to the difference in the wind speed itself (that is, the overestimation of the far wake). At almost all downstream positions ($x/D > 3$), LES agrees with the experiment relatively well.
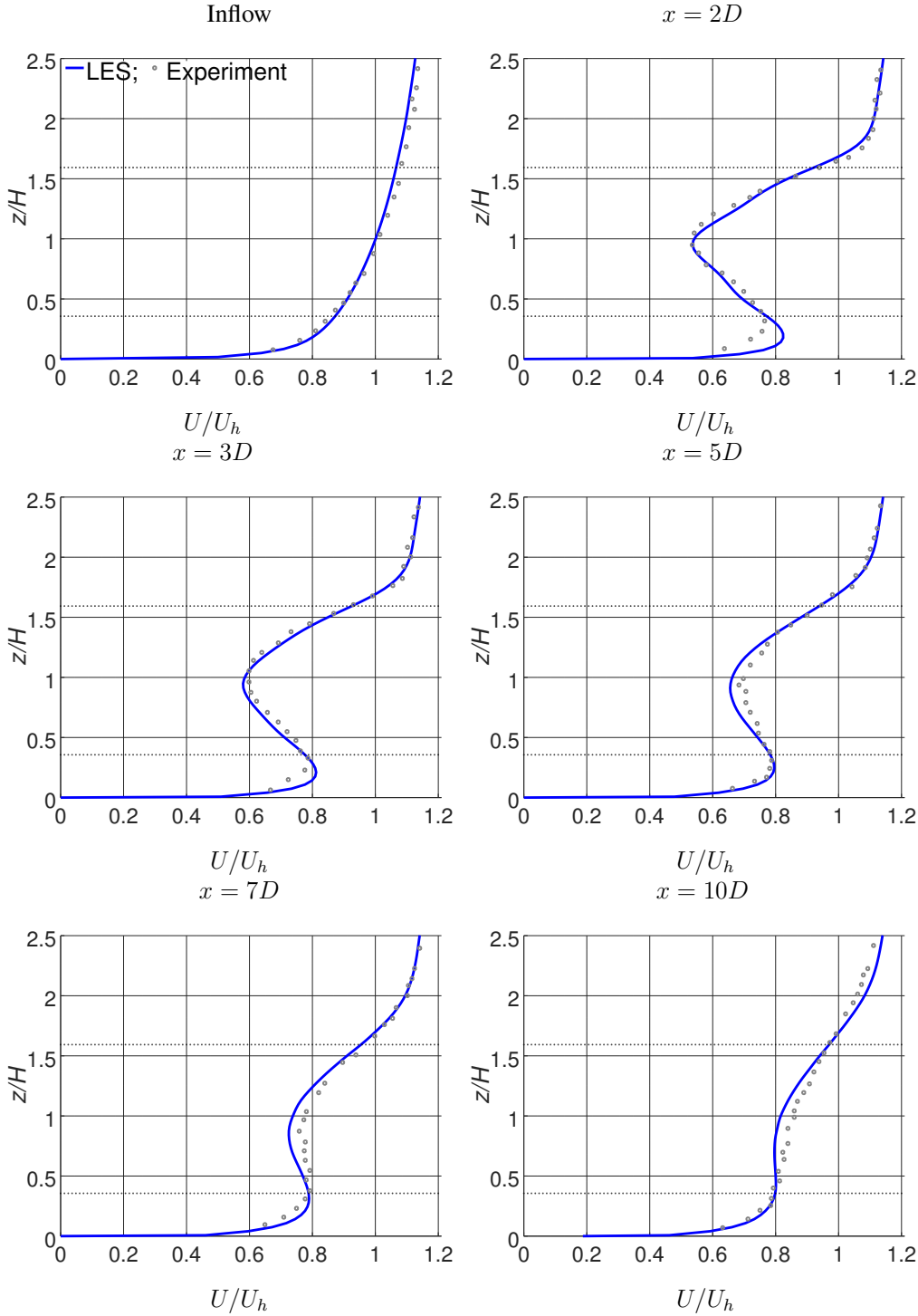
Figure 4.4.5: LES prediction vs experimental data for normalized mean-velocity U/U_h profiles at different windwise locations. The experimental data are digitally extracted from Chamorro and Porté-Agel (2009).
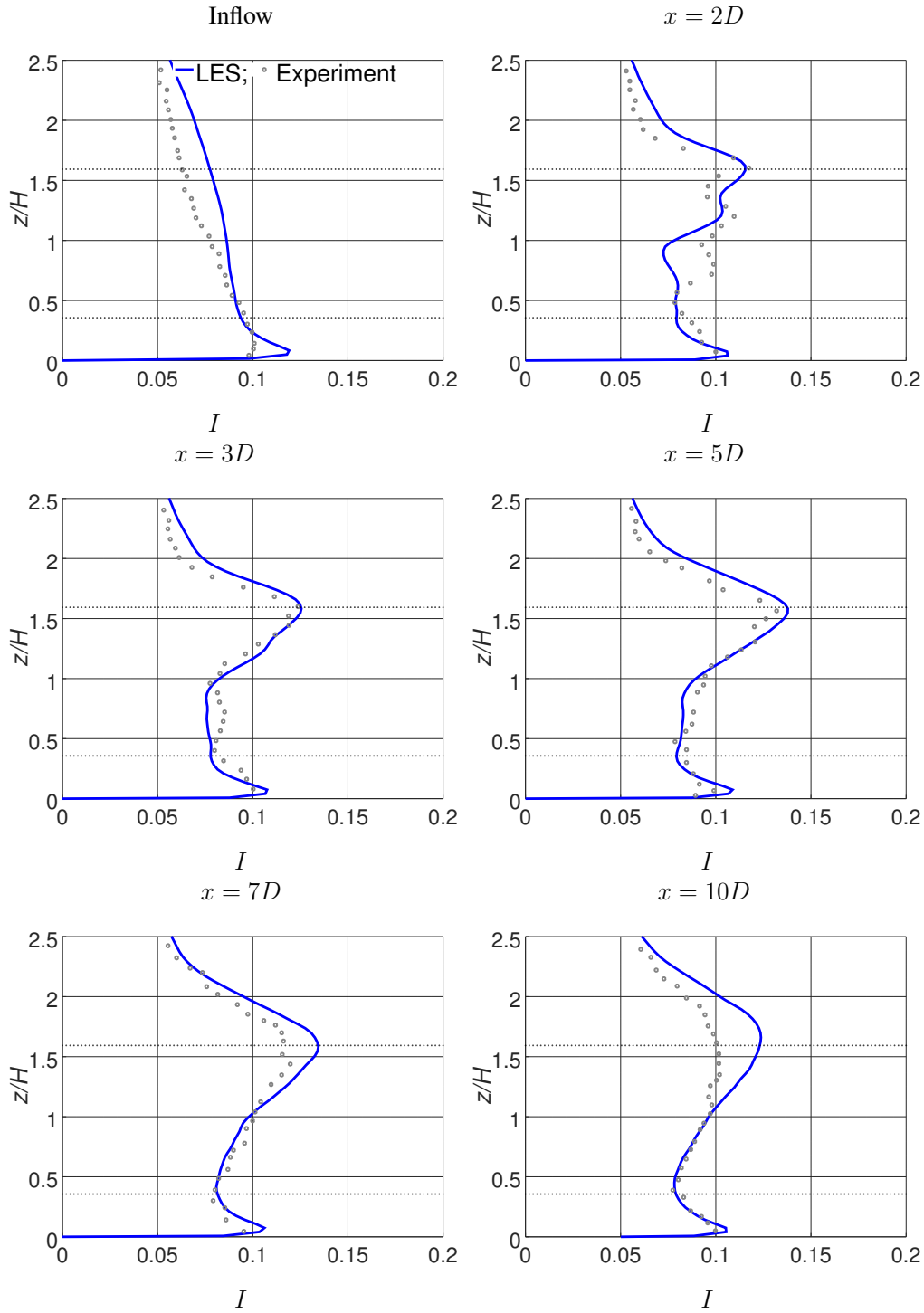
Figure 4.4.6: LES prediction vs experimental data for turbulence intensity I profiles at different windwise locations.
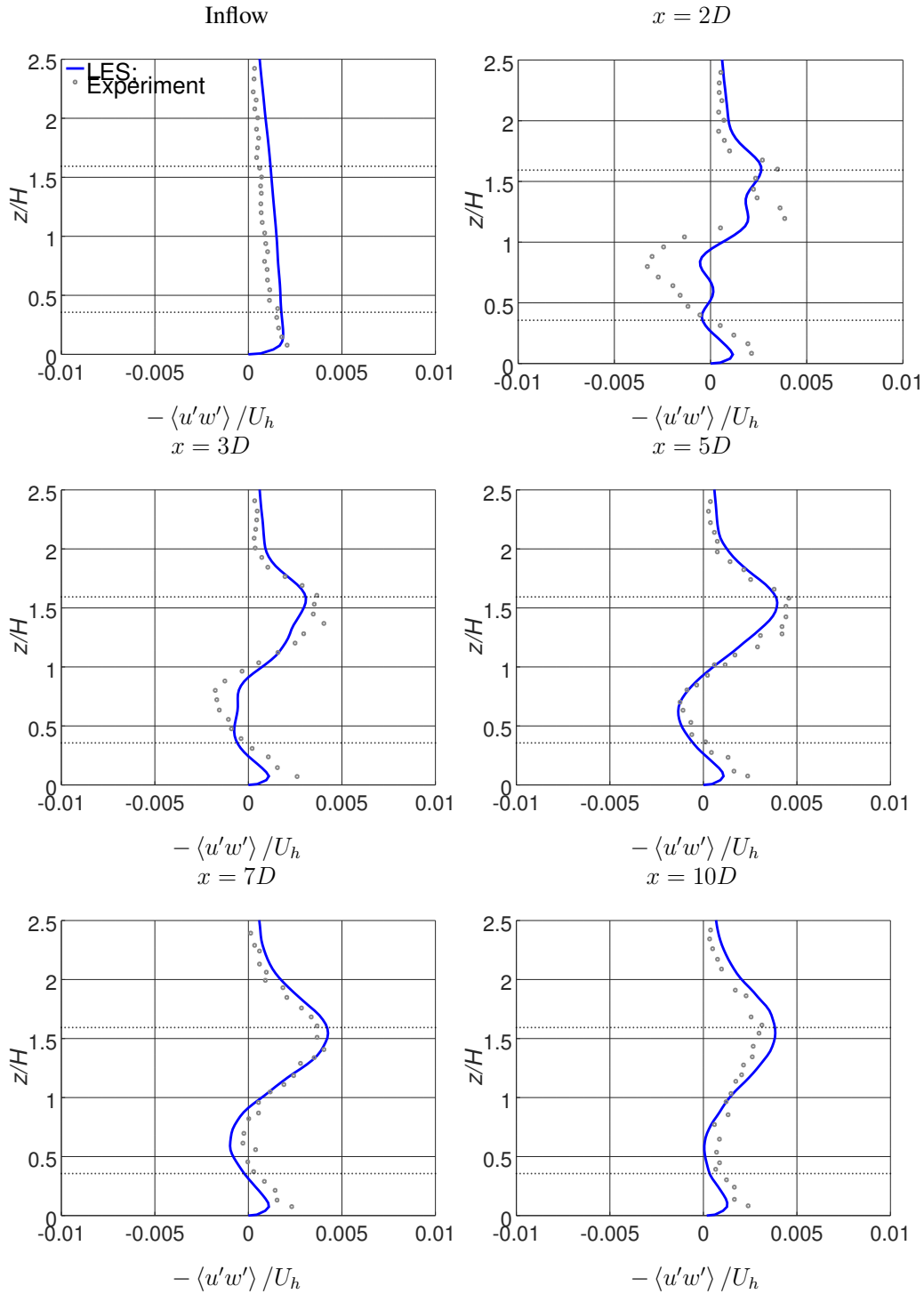
Figure 4.4.7: Numerical results for simulation vs. experimental data for vertical Reynolds shear-stress profiles at different downstream locations.

Figure 4.4.8 top and bottom both represent the top view of a contour plot of the mean windwise velocity (U) taken at the turbine hub height ($z = 90$ m). The top picture represents the flow over the full computational domain, but the bottom picture shows only the wake area. Here and below, the contours of the results obtained on the coarse (0.0056 m resolution, $D/\Delta x = 27$) grid are shown. As shown in Figure 4.4.8, the region with a very strong and moderately strong wake spreads up to $x = 2.5D$ and $x = 6D$, respectively. Furthermore, velocity is increasing approximately to $0.8U_h$ at $x = 10D$ downstream. Besides, the small areas of high wind speed ($U > U_h$) are generated right next to the turbine left/right tip positions ($y = \pm R$). It seems that the flow is fully developed and homogeneous in the horizontal plane. Hence, the domain size is correctly chosen.
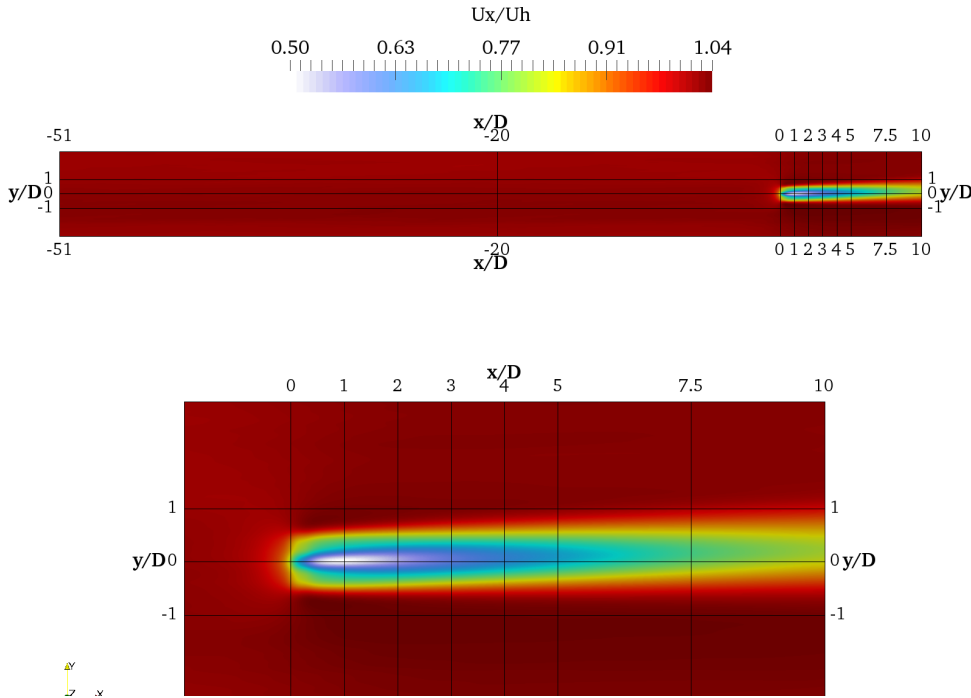
Figure 4.4.8: Top view at the turbine hub height ($z = 90$ m) of normalized mean windwise velocity. Top figure represents full domain. Bottom figure zooms into the turbine wake region.

Next, the obtained LES prediction is qualitatively compared with numerical results obtained for almost the same case and published in Yang et al. (2014) and with the experimental results of (Porté-Agel et al., 2011). Figure 4.4.9 shows the vertical cross-section at $y = 0$ of the LES prediction for normalized time-averaged windwise and crosswind velocity, turbulence intensity, and vertical Reynolds shear stress $-\langle u'w' \rangle$.

The present U_x prediction around the hub height ($z \simeq H$) differs from the ones pub-

lished in Yang et al. (2014) (see Figure 7 from Yang et al. (2014)), Chamorro and Porté-Agel (2009) (Figure 3) and Porté-Agel et al. (2011) (Figure 5) in the near-wake region ($x < 2D$). The area of decreased velocity around the hub height ($z \simeq H, x < 2D$) ($U = 0.4U_h$ in Yang et al. (2014) and $U = 0.46U_h$ in Porté-Agel et al. (2011)) exists in the present LES as well. However, the velocity ($U = 0.5U_h$) is slightly overestimated by the present LES. The difference could be induced by a different interpretation of turbine nacelle and tower. That is, the torus with a tiny inner radius is made by actuator lines in Yang et al. (2014). The miniature turbine from the wind-tunnel experiment (Chamorro and Porté-Agel, 2009) has the real nacelle. In the present study, the nacelle model proposed by Wu and Porté-Agel (2011) is used. That is, the drag coefficient is fixed to 0.85 in the nacelle area.

The area of increased turbulence intensity ($I = 0.105$) around (slightly above) the hub height ($z \simeq H, 0.5D < x < 3D$) is present in Figure 4.4.9, but the turbulence intensity is 1.5 times smaller than in Yang et al. (2014) and slightly shifted above the hub height ($z > H$). The other region of increased turbulence intensity (around upper tip position $z = 1.6H$ or $z = H + R$) persists in both, the present LES and the one performed by Yang et al. (2014), from $x = 1.5D$ and $x = 1D$ downstream to $x = 10D$ and $x = 9D$, respectively, and agrees with the measurements and simulations by Porté-Agel et al. (2011).

The present U_y prediction agrees with the one obtained by (Yang et al., 2014). The crosswind velocity U_y is essentially influenced by the turbine rotation, which continues to more than $x = 6D$ and disappears behind $x = 8D$ downstream from the wind turbine.

The contours of the primary Reynolds shear stress ($- \langle u'w' \rangle$) from Figure 4.4.9 show that there are two regions with a large magnitude of Reynolds shear stress and two with a medium magnitude. The large two reside at the upper and lower tips of the wind turbine ($z = H \pm R$) and maintained downwind to $x = 10D$. This investigation is in agreement with Yang et al. (2014). The secondary maxima (where $- \langle u'w' \rangle / U_h^2 = -0.0005$ and $- \langle u'w' \rangle / U_h^2 = 0.00015$) are located around the tower height ($z \simeq H$) and within $x < 2D$ downwind from the wind turbine. Nevertheless, the regions with a significantly large magnitude of the vertical Reynolds shear stresses ($- \langle u'w' \rangle / U_h^2 = -0.005$ and $- \langle u'w' \rangle / U_h^2 = 0.008$, respectively) were obtained in Yang et al. (2014). Therefore, the differences between the present LES, measurements by Porté-Agel et al. (2011) and other studies of similar cases (that is, Porté-Agel et al. (2011) and Yang et al. (2014)) occur in the hub height region, which could be due to the presence and absence of the nacelle model.
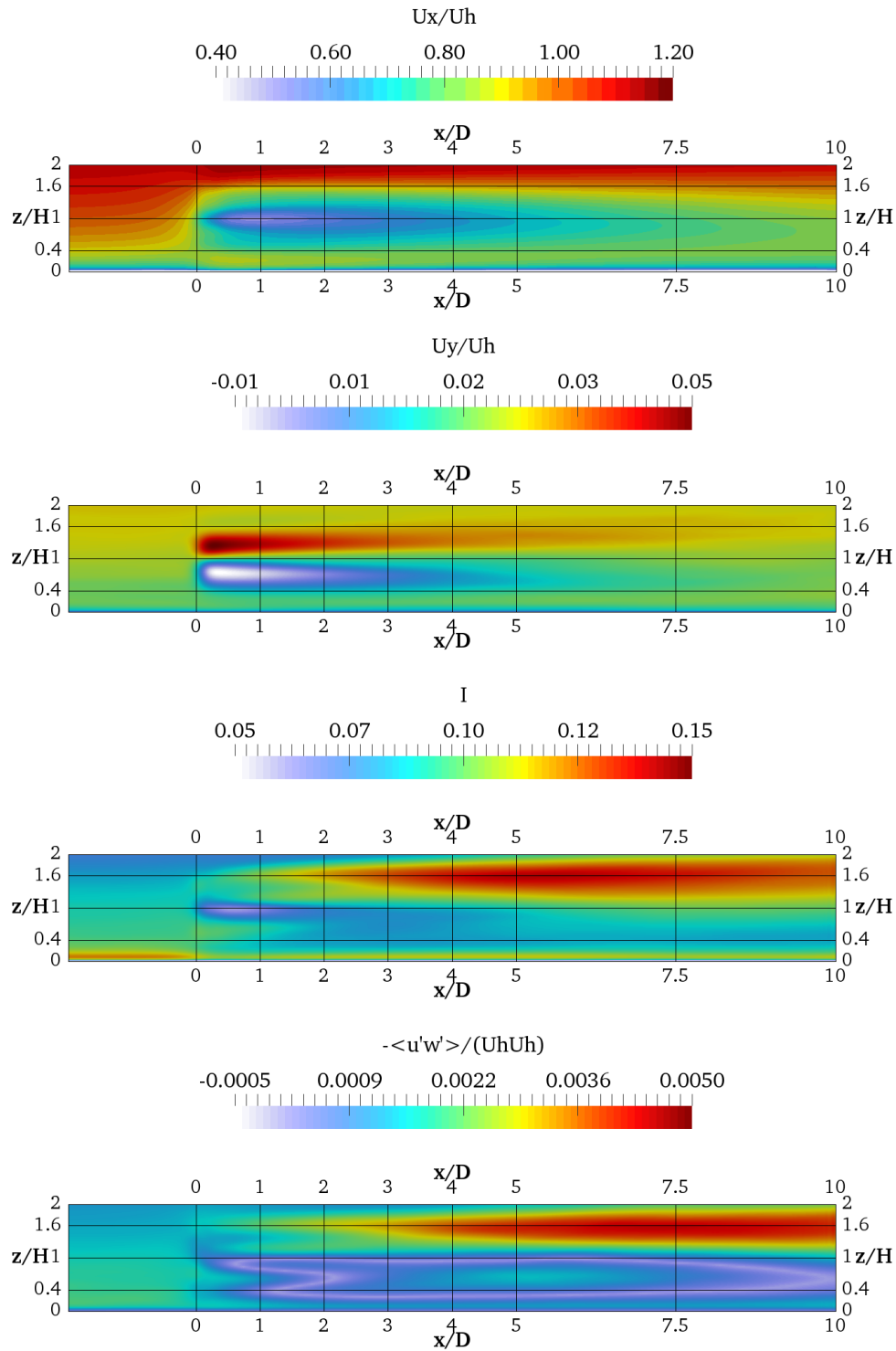
Figure 4.4.9: Vertical cross-section of LES prediction for normalized time-averaged wind-wise and crosswind velocity, turbulence intensity, and primary Reynolds shear stress $-\langle u'w'\rangle/U_h^2$.

In Addition to the cases described in Table 4.4.1, the LES simulations are performed on a very coarse grid in the cases described below in Table 4.4.6. The additional LES is performed in order to show how sensitive the ALM is to the airfoil type, the mounting pitch and the smearing coefficient. Figure 4.4.10 shows the LES prediction at a very coarse grid for different smearing coefficients ε vs experimental data for normalized mean-velocity deficit DU at the position $x = 2D$. As can be seen, the increase in smearing coefficient ε does not necessarily increase the length of the wake. For example in the case T0p8m8, where $\varepsilon = 8\Delta x$, the wake length, in contrast, decreased in comparison to the case T0p8m8 ($\varepsilon = 4\Delta x$). Therefore, ε should be chosen such that ε will not be much larger than half of the turbine radius R. Next, the mounting pitch influence on the wake is studied. It is seen in the figure that the flow is very sensitive to the pitch changes. For example, the case T0p8m4 with $\varphi = 0$ and flat-plate airfoil gives the second worst (after the case with $\varepsilon = 8\Delta x$) velocity deficit prediction at $x/D = 2$. The relative error obtained in that case at hub height is 34% at $x = 2D$. It is very similar to that from the study of Yang et al. (2014). The relative error estimated from the results of Yang et al. (2014) for the flat-plate case equals approximately 31% at $x = 2D$ and $z = H$. However, the result (Yang et al., 2014) was improved using the nacelle and tower models. Thus the relative error is 24%. It is found in the present study that decreasing the pitch from 0° to -10° increases the length of the wake. Since the airfoil type of the miniature turbine is not known exactly, the initial guess that the airfoil type may be unsymmetrical is checked. The airfoil data for a cambered flat-plate are extracted from Sunada et al. (1997). Finally, the case T0p8m4c gives the best agreement with the experiment(among all cases obtained at a 0.0112 m resolution grid).

Table 4.4.6: Description of the cases with one wind turbine performed on the very coarse grid (0.0112 m resolution, D/Δx = 13.5) using different parameters such as the mounting pitch, smearing coefficient, and lift and drag coefficients.

	$\varphi,^o$	ε	airfioil type
T10p8m4	-10	$4\Delta x$	symmetric
T5p8m4	-5	$4\Delta x$	symmetric
T0p8m4	0	$4\Delta x$	symmetric
T0p8m8	0	$8\Delta x$	symmetric
T0p8m4c	0	$4\Delta x$	cambered*

*The lift and drag coefficients used in that case corresponds to the cambered flat-plate from Sunada et al. (1997).

Thus, as described above, ALM is very sensitive to the choice of the physical parameters: the airfoil type and mounting pitch and the numerical parameter (i.e., the smearing coefficient). Based on the results of the present study, the parameter ε should be chosen in such a way that $\varepsilon \geq 2\Delta x$. However, ε should not be larger than half of the turbine radius R. In case of $D/\Delta x = 27$, the best choice so far is $\varepsilon = 4\Delta x$ ($\varepsilon/R = 0.3$). The study by Chamorro and Porté-Agel (2009) is not suggested to be further used as the
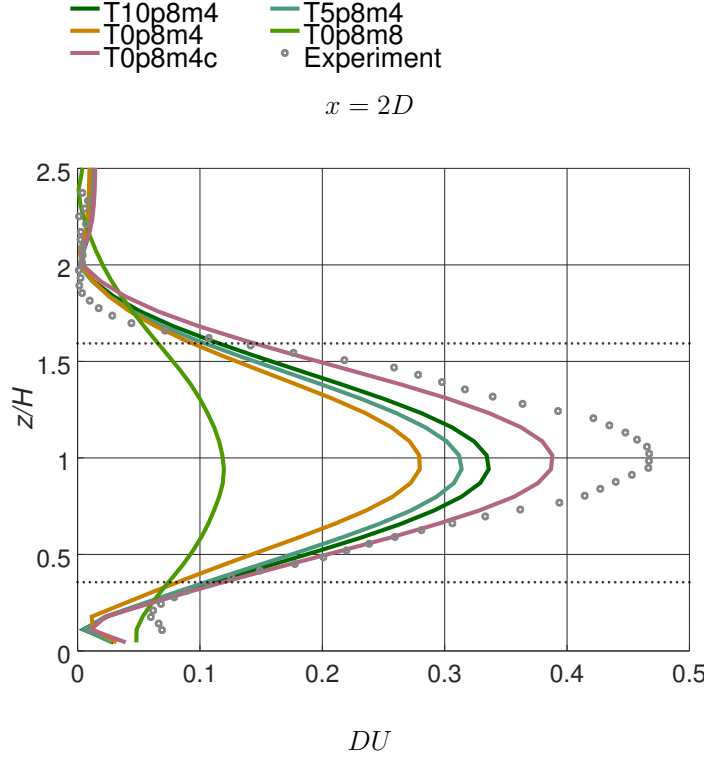
Figure 4.4.10: LES prediction at a very coarse grid for different smearing coefficients ε vs experimental data for normalized mean-velocity deficit DU at position $x = 2D$. The experimental data are digitally extracted from Chamorro and Porté-Agel (2009).

validation because of the unknown airfoil type and thus the absence of airfoil data. In the present study, good agreement with the experiment is achieved with the flat-plate airfoil by decreasing the mounting pitch. The results of the present study suggest that good agreement can be also achieved by using the cambered flat-plate or other cambered airfoil data available at a low Reynolds number. It was also found that the grid convergence study is not possible to make for the simulations with ALM because of the influence of ε. See Figures 4.4.3-4.4.4. Thus, the recommendation regarding the grid resolution (based on the grid convergence study) is not included in the present study. However, the grid resolution of at least $D/\Delta x = 27$ was found to be enough to get a good agreement with the experimental data.

4.5   Isolated wind turbine and two turbines in tandem

Next, a LES over an isolated wind turbine was performed on a real scale in order to use the real wind-turbine characteristics. Thus, the diameter (D) of the wind turbine from the experiment was scaled up to 108 m. The hub height (H) of the simulated wind turbine is 90 m. For reference, the wind turbines in Muukko (Alstom ECO 110) have a 110 m diameter, 90 m hub height and 3 MW rated power. The chord length and twist angle of the blade at different radial locations of the turbine blade are taken from Kim et al. (2011) for a real-scale designed 3 MW wind turbine with a similar diameter (see Figure 4.5.2). The airfoil type of blade in the Alstom ECO 110 wind turbines is not exactly known. Therefore, in this case (and in the further simulations of the present study), the blade is represented by a NACA0012 airfoil. Lift- and drag-coefficient curves used in the simulations are presented in Figure 4.5.2.
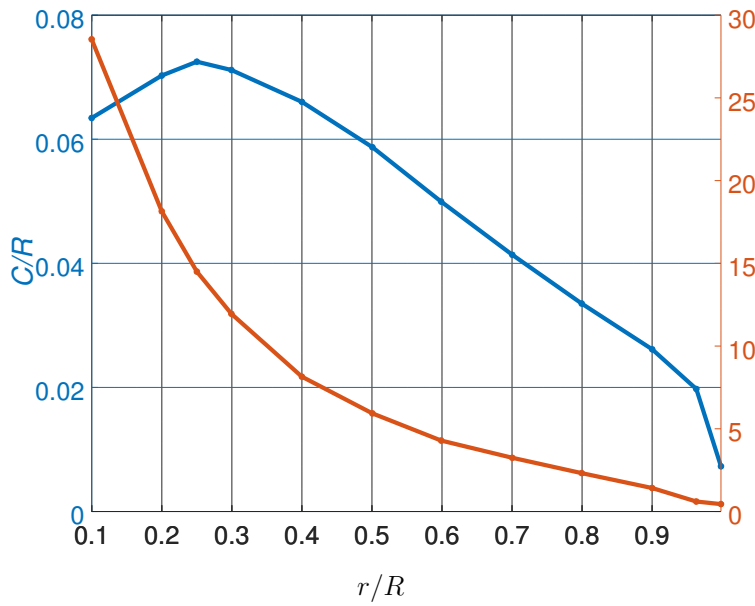
Figure 4.5.1: The chord length and twist angle distributions of a 3MW wind turbine are taken from Kim et al. (2011).

The inflow velocity at the hub height is approximately 10 m/s. The tip-speed ratio $\lambda = \Omega D/(2U_h)$ is about 4.3 and the rotational speed Ω is 7.5 rpm. The computational domain is extended upstream and downstream from the wind turbine location to $32D$ and $10D$, respectively. Height and width of the computational domain are $4D$. The turbine is located in the middle of the crosswind direction. The computational grid, created using the "blockMesh" utility in OpenFOAM®, consists of 1134, 108 and 124 hexahedral cells in the windwise, crosswind and vertical directions, respectively. The minimum con-

Figure 4.5.2: Aerodynamic force coefficients for NACA0012 blades. Lift and drag coefficients are taken from Sheldahl and Klimas (1981).

trol volume is 4 m×4 m×3 m and the maximum is 4 m×4 m×4 m. The grid nodes are uniformly distributed in windwise and crosswind directions. Thus, the number of grid cells per rotor diameter is approximately 27 cells. T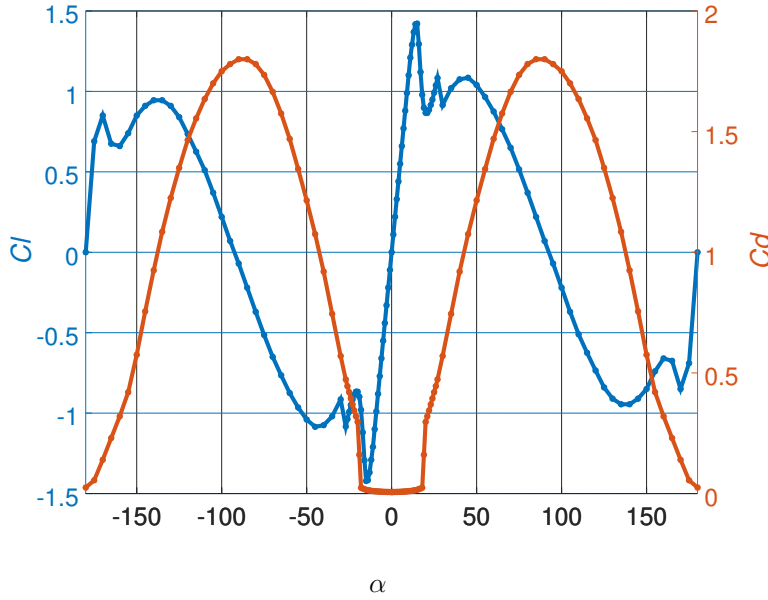he velocity boundary conditions at the inlet are mapped from the cross-section plane at $16D$ downstream using the recycling technique (Baba-Ahmadi and Tabor, 2009; Agafonova et al., 2014a,b; Chaudhari et al., 2014a; Chaudhari, 2014). The simple rough logarithmic atmospheric boundary layer (ABL) model is employed as the wall function model (see Chapter 2, Chaudhari (2014)). The case with the one and two wind turbines are named T1r4m3 and T2r4m3, respectively.

A simulation over two wind turbines is performed on the same 4 m resolution grid as in the case of the single wind turbine. The second wind turbine is located $5D$ downstream from the first one. Both turbines have the same aerodynamic characteristics as the turbine from the validation case. The aerodynamic forces calculated on virtual lines are distributed on the grid cells using 3D Gaussian distribution (see Equation 4.3.7) with smearing parameter $\varepsilon = 3dx$.

Below, in order to see the effects induced by the first turbine downstream to the output of the following wind turbine as well as the upstream influence from the second turbine to the first one, the case with two wind turbines case is compared to the case with a single turbine.

Figure 4.5.3 shows the LES prediction of deficit of windwise velocity at different wind-wise locations for the cases with the stand-alone wind turbine and the first of two wind turbines in row. As one can see, the inflow velocity prediction for two turbines slightly differs from the one obtained in the case of one turbine above the upper tip ($z > H + R$). A deeper investigation of this observation was performed. According to that, the difference in the velocity prediction is found to be a cause of insufficient distance between the recycling plane and the wind turbine (see chapter LES modelling). Applying the distance of $16D$, the inflow is slightly affected by the upstream noise generated by the turbine. In order to reduce the influence of the inflow on the downstream wakes, the deficit of the mean windwise velocity (DU) and turbulence intensity excess (DI) are presented in the following Figures 4.5.3 and 4.5.5, respectively. It can be seen from Figure 4.5.3 that the predictions for the single and the first wind turbine (of two in tandem) almost coincide at positions $x = 2D$ and $x = 3D$. It suggests that the wake development of the preceding wind turbine is not (or almost not) influenced by the upstream effects from rotation of the following turbine.

Figure 4.5.4 shows the difference in the wake behaviour of a stand-alone wind turbine and a turbine placed in the wake of the preceding one. It is clearly seen from Figure 4.5.4 that the wake of the second wind turbine is much larger than the wake of stand-alone wind turbine. The maximum relative difference $\left| DU^{2WT} - DU^{1WT} \right| / DU^{1WT}$ corresponds to 53% and 45% at positions $x = 2D$ and $x = 5D$ downwind from the turbine, respectively.

The difference in the excess of windwise turbulence intensity (DI) between cases with a single wind turbine and the first of the two turbines in tandem presented in Figure 4.5.5 is not significant, even though the inflow intensities (I) are different.

The difference in the windwise turbulence intensity behaviour of the stand-alone wind turbine and the turbine placed in the wake of the preceding one can be seen in Figure 4.5.6. The velocity beyond the second wind turbine is almost half of the velocity of the stand-alone wind turbine between $x = 2D$ and $x = 5D$ downwind. However, the turbulence intensity difference is even larger. For example, the turbulence intensity increase is tripled at $x = 2D$ and doubled at $x = 5D$.

The LES of the case T1r4m3 with one turbine and the case T2r4m3 with two turbines in tandem were performed and compared to each other above in the present section. First of all, the wake of the upwind turbine (the first of two) from the case T2r4m3 is compared to the reference wake of the single turbine (T1r4m3). The difference between the compared results for velocity deficit and turbulence intensity excess is not more than 10%. Therefore, there seems to be no physical upstream effect generated by the following turbine. The difference within 10% most probably is due to the numerical noise from the rotation of the downwind turbine and insufficient averaging time in the case T1r4m3. In the present simulations, the upstream noise generated by the wind-turbine rotation reaches up to $16D$, upwind and therefore it affects the mapping plane and inflow. It suggests that the present distance between the mapping plane and the turbine of $16D$ is not enough to

avoid any upstream influence from the turbine on the inflow condition. The length of the buffer zone was further increased to $20D$. Using the distance of $20D$ between the recycling region and the turbine, it is guaranteed to have no turbine effects at the inlet mean wind speed. However, it may be not enough long for the turbulence intensity. Next, the wake of the downwind turbine (the second of two) from the case T2r4m3 is compared to the reference wake of the single turbine (T1r4m3). Figures 4.5.4 and 4.5.6 show the doubled and tripled increase of the velocity deficit and turbulence intensity excess for the following wind turbine. Since the velocity deficit at the second turbine location ($x = 5D$) is 13%, then, the turbine located in the wake of the first one will produce approximately 34% less power than the first turbine or the isolated wind turbine. Next, an imaginary third turbine could produce 54% less power than the first one. Therefore, one should consider a distance larger than $5D$ between the turbines when planning a real wind farm.
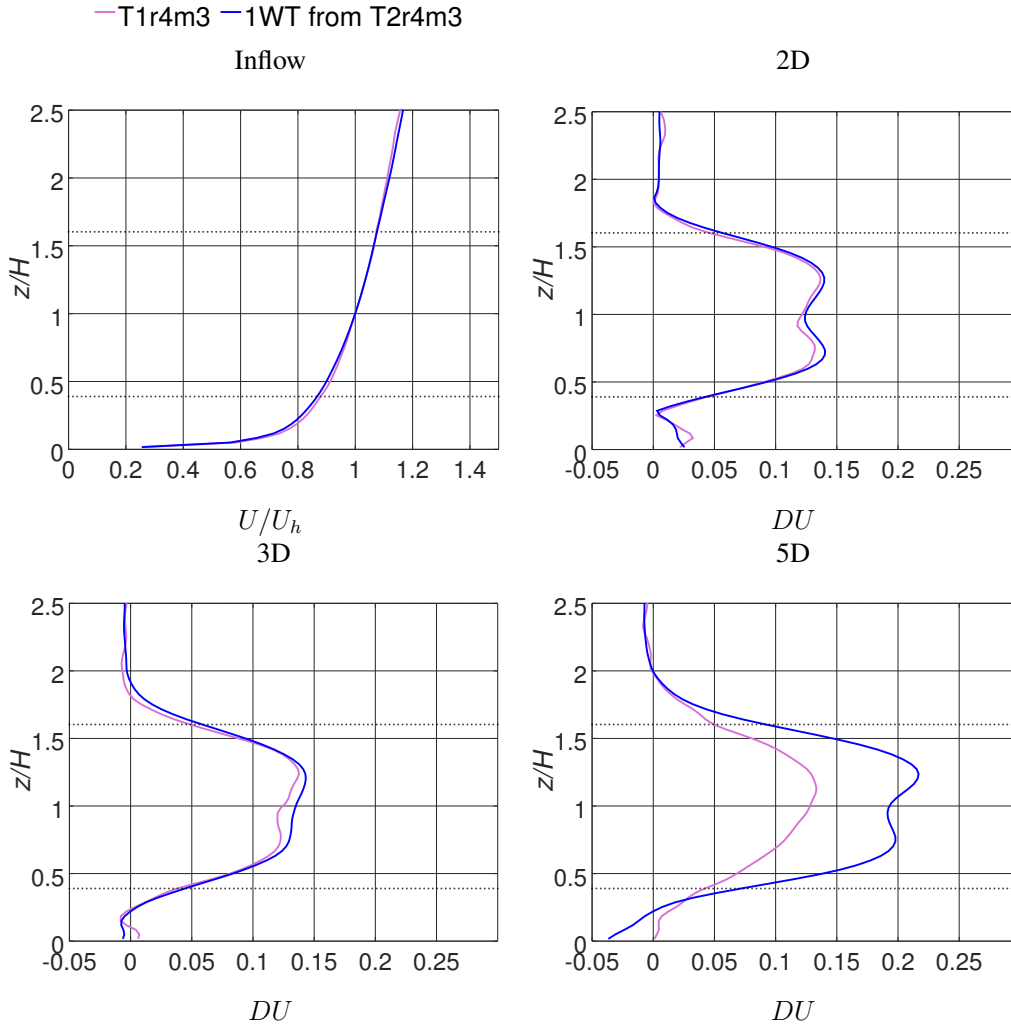
Figure 4.5.3: LES prediction for for normalized inflow windwise velocity (U/U_h) and deficit of windwise velocity $DU = (U^{inflow} - U^{wake})/U^{inflow}$ at different windwise locations in the cases with one and two wind turbines.
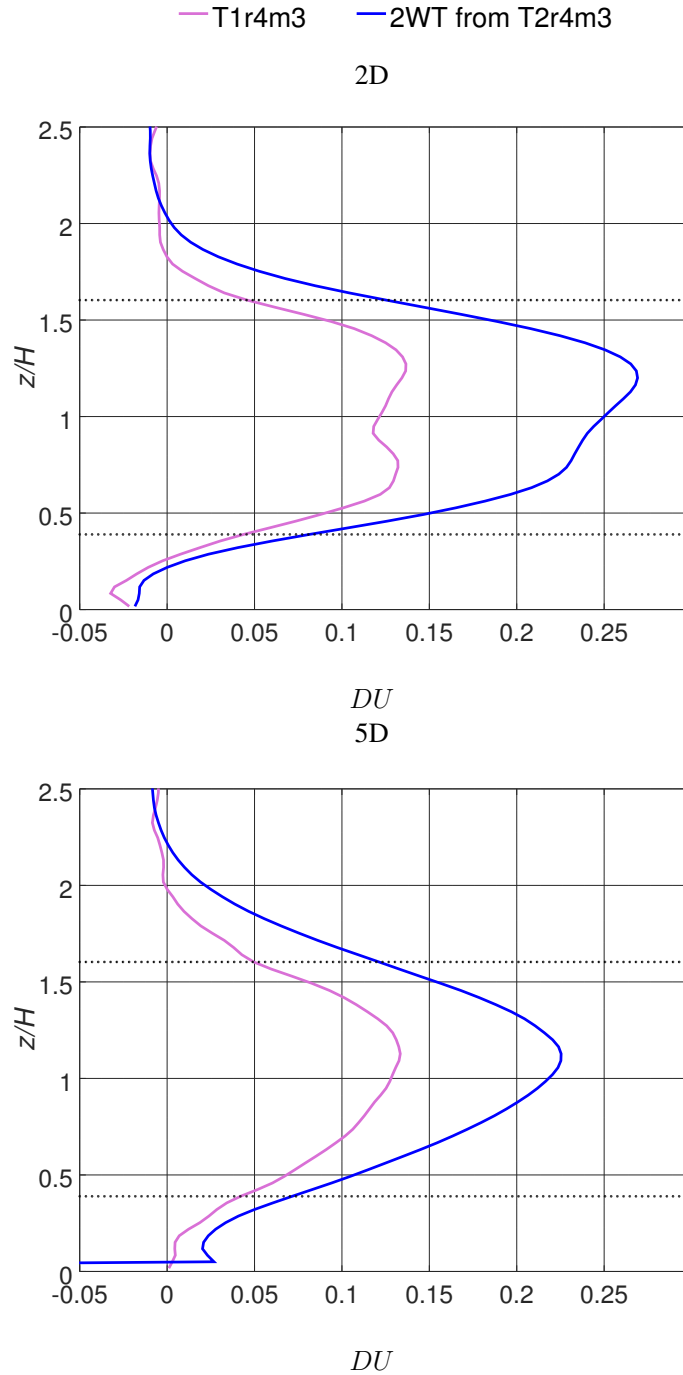
Figure 4.5.4: LES prediction of windwise velocity deficit (DU) for the second wind turbine (out of two turbines) at different windwise locations in comparison with the case with single wind turbine.

Figure 4.5.5: LES prediction for the inflow windwise turbulence intensity and an excess of windwise turbulence intensity $DI = (I^{wake} - I^{inflow})/I^{inflow}$ at different windwise locations in the cases with one turbine and the first of two wind turbines.

Figure 4.5.6: LES prediction of the windwise turbulence intensity excess (DI) for the second wind turbine (out of two turbines) at different windwise locations compared to the case with a single wind turbine.

Chapter 5

Results: LES with wind turbines and forest

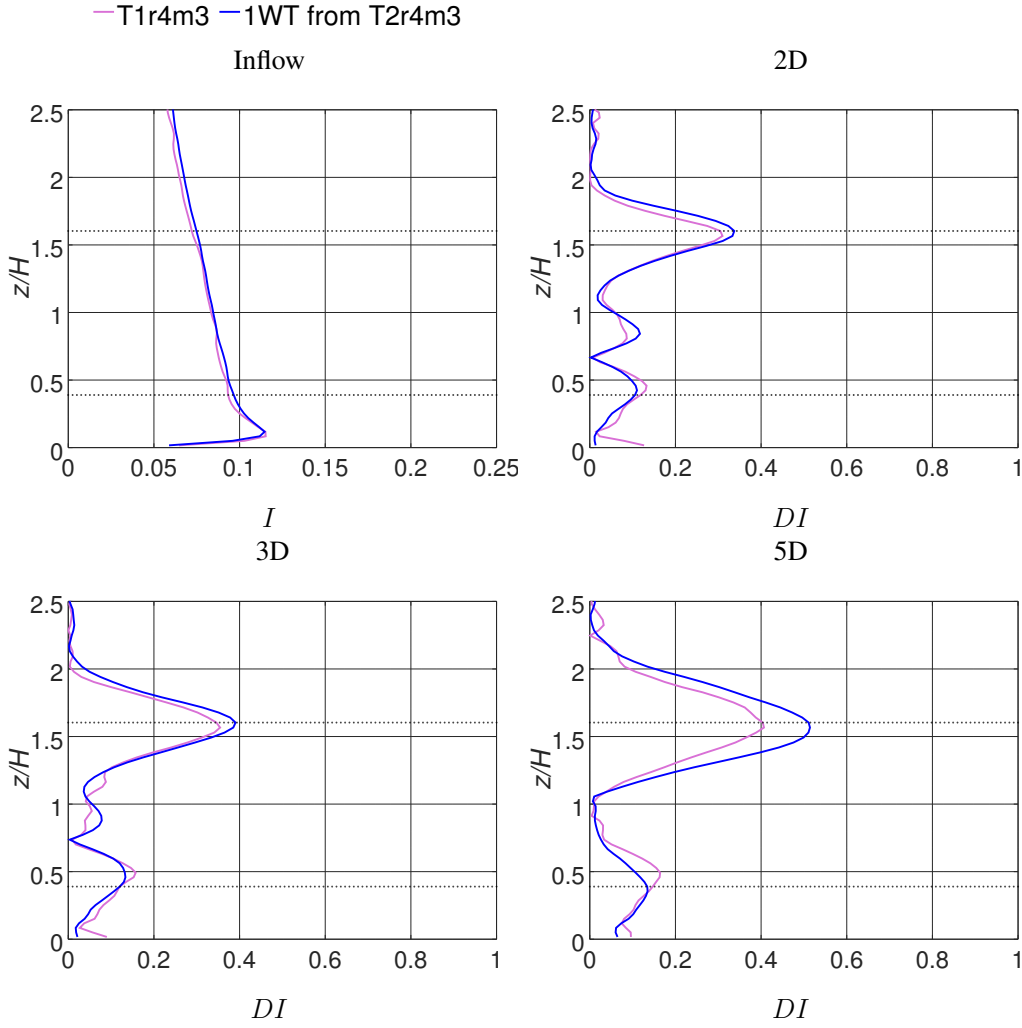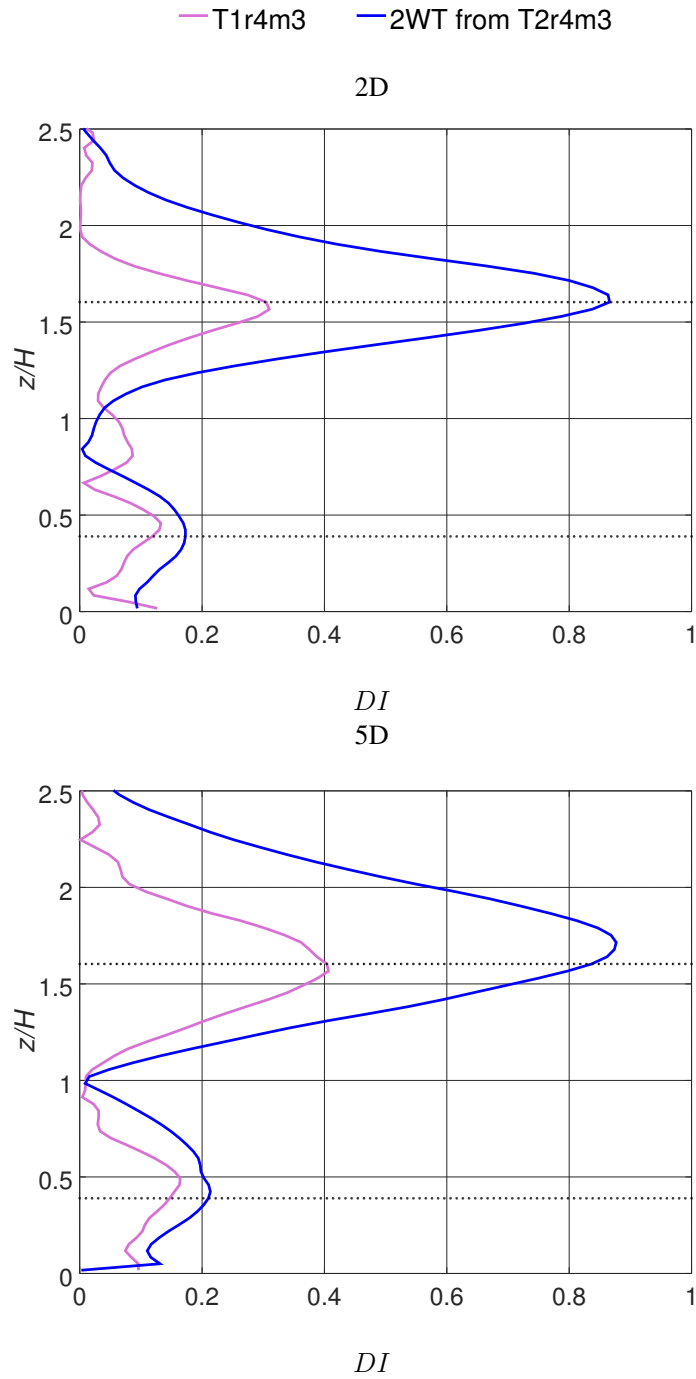In this chapter, mean wind behaviour, turbulence, power production and other results are considered for cases with and without forest. The cases have identical setups except for the presence of forest in one of them. Therefore, it is assumed that the differences in the results occur due to the forest canopy.

5.1 Two turbines in tandem

In the present section the effects on the mean wind speed, turbulence and power production due to the forest are discussed for the case with two wind turbines in tandem.

5.1.1 Numerical setup

Two wind turbines from the previous case (see Chapter 4) were placed in the pine forest, which is commonly found in Finland. The canopy characteristics, C_D=0.15 and $\alpha(z)$, are the same as in Chapter 3 and taken from Shaw and Schumann (1992). The height of the forest (H) is 20m. The velocity in the mapping zone is fixed to be equal to 10 m/s in the windwise direction, thus, the inflow velocity at hub height is calculated to be 7.8 m/s in the forest case. However, fixing the same 10 m/s velocity in the mapping zone in the case without forest gives U_h=8.96 m/s at hub height. First of all, a simulation with two wind turbines located in the forest was carried out on the same grid as before. But a numerical instability problem occurred in some cells close to the outlet boundary. At the beginning, it was thought to be a problem of a too large time-step. Thus, it was decided to decrease the time-step size in a way that the Courant number was equal to 0.01. (In the final simulations, the Courant number was increased to 0.25.) However, it did not guarantee a successful performance of the simulation. Furthermore, it was found that the problem is related to a flow recirculation above the forest and thus a local inflow on the outflow boundary. Finally, the stability was established by extending the computational domain (up to 33D behind the downwind turbine) with a smooth cut of the forest at 14D-17D
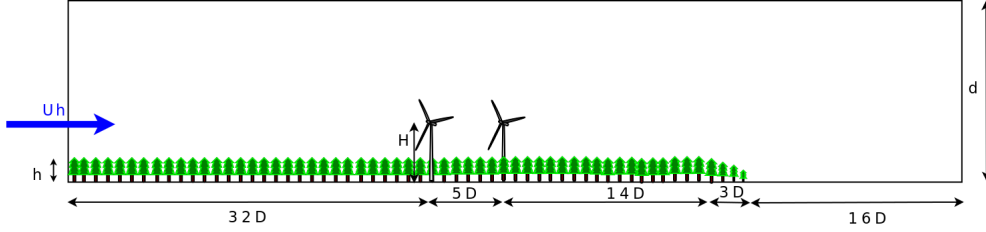
Figure 5.1.1: Side view of the computational domain in the forest case

behind the second turbine. The smooth cut means that the LAD was smoothly changed by 25% of the previous one at every D behind $14D$. The computational domain in the forest case with 2WTs can be seen in Figure 5.1.1. Therefore, the number of cells in the computational grid in the case of forest with respect to the non-forest case was increased by 67% to $25.3 \cdot 10^6$ finite volume cells.

5.1.2   Results and discussion

The top view of the normalized mean windwise velocity in the cases with and without forest is presented in Figure 5.1.2. One can see from Figure 5.1.2 that the wake above the forest is wider but shorter ($l_x < 3D$) than it is in the case without forest ($l_x > 4D$). The wake of the first turbine is weaker in front of the second turbine in the case of forest. At the same time, in the case without forest, the second turbine is located in the rather strong wake from the first turbine.

Figure 5.1.3 shows the contour plot of the side view taken at the middle of the domain ($y=0D$) without (top) and with (bottom) the forest. It can be seen from Figure 5.1.3 that the wake above the forest is not clearly visible. It seems to disappear within the forest. And, the forest is generating a rather high velocity gradient ($U \mid_{z=2H} = 1.31U_h$) above the wake, while in the case without forest, $U \mid_{z=2H} = 1.114U_h$.

Figure 5.1.4 presents the LES-predicted normalized mean windwise velocity U/U_h profiles at different windwise locations in the cases with and without forest in comparison to the reference (inflow) velocity. It is clearly seen from the figures that the forest wake has approximately the same strength as the non-forest wake at the first turbine location ($x = 0D$). Furthermore, it starts to grow rapidly thus the wake in the forest case becomes slightly stronger than the one in the non-forest case at positions $x = 1D$ and $x = 2D$. After that, at position $x = 3D$, the wake above the forest starts to decrease. However, the wake from the non-forest case is still developing at $x = 3D$ and $x = 4D$. The wakes from both cases (especially the one above the forest) were developed in length and, moreover, in height during their evolution.

$$U/U_h$$
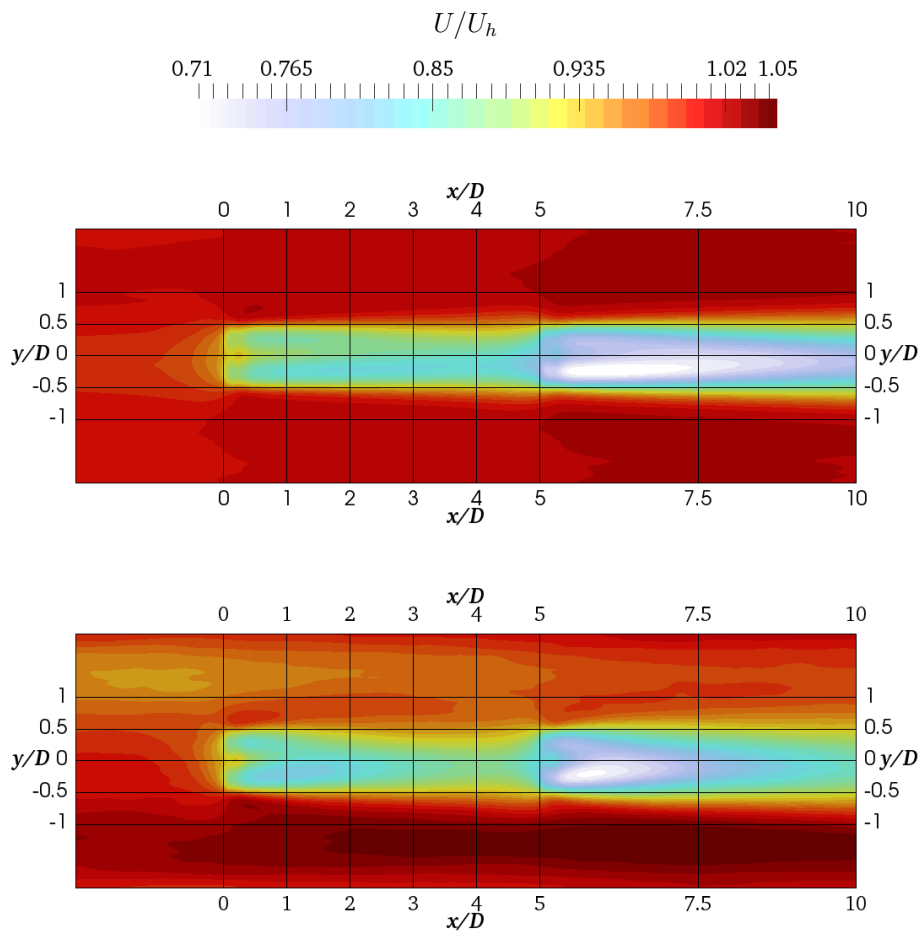
Figure 5.1.2: Top view of the normalized mean windwise velocity in the cases without (top) and with (bottom) the forest.

U/U_h
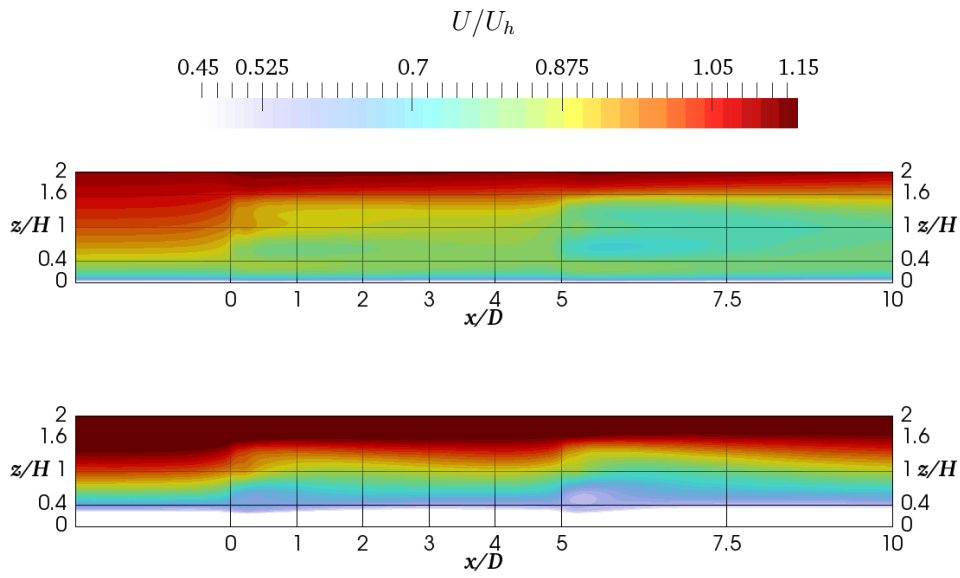
Figure 5.1.3: Side view of contours at $(y = 0)$ of normalized mean windwise velocity for the cases with forest (top) and without forest (bottom).
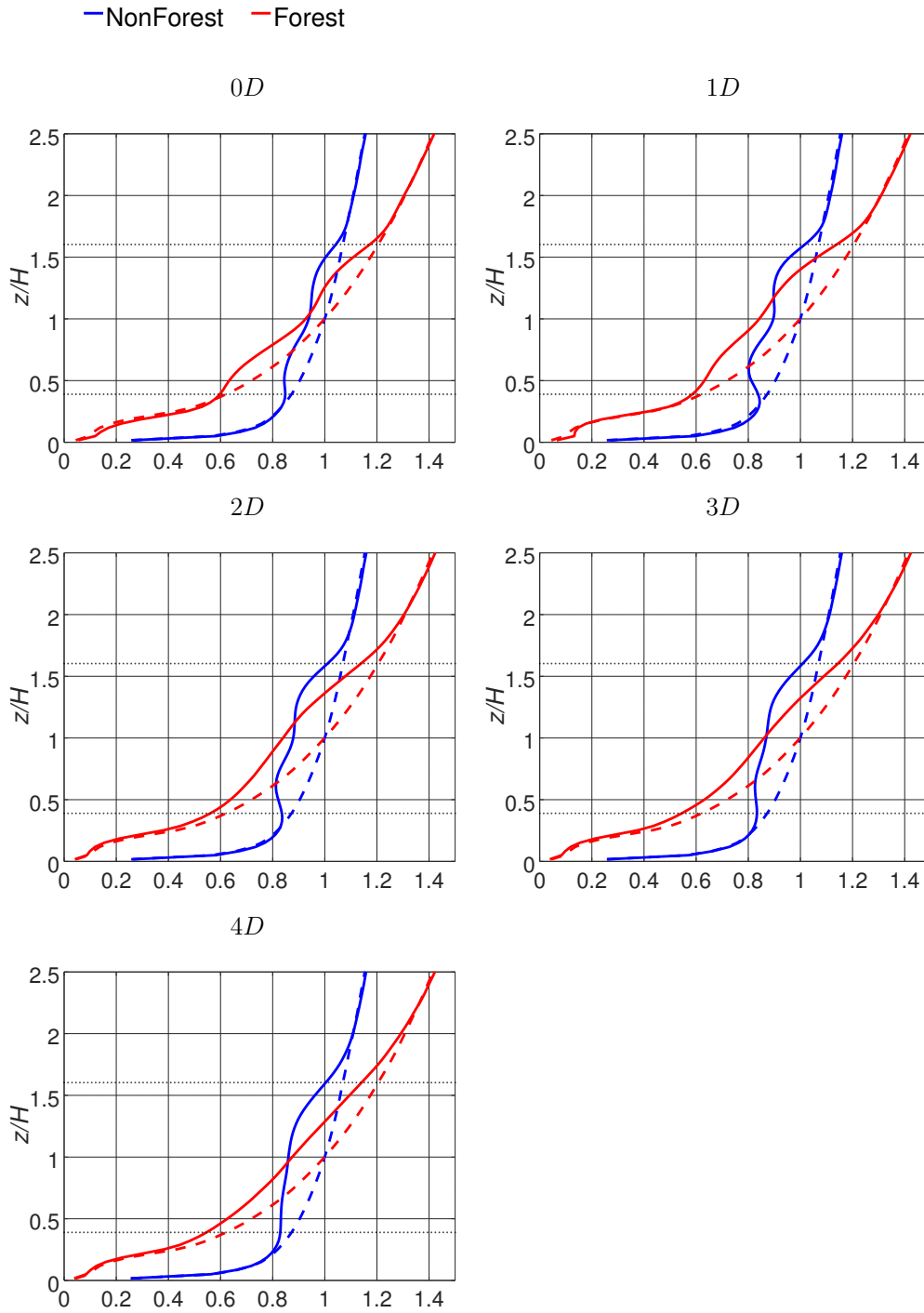
Figure 5.1.4: LES-predicted normalized mean velocity U/U_h profiles at different wind-wise locations ($0D \leq x \leq 4D$) in the cases with and without forest. Dashed lines represent the reference, which in the present case is the inflow velocity.

Figure 5.1.5 shows the evolution of the wake of the second turbine in the forest and non-forest cases compared to the wake of the first turbine. It could be seen from Figure 5.1.5 that the following wake above the forest is slightly stronger than the wake behind the previous turbine. However, in the case without forest, the difference is more than two times larger than in the forest case.
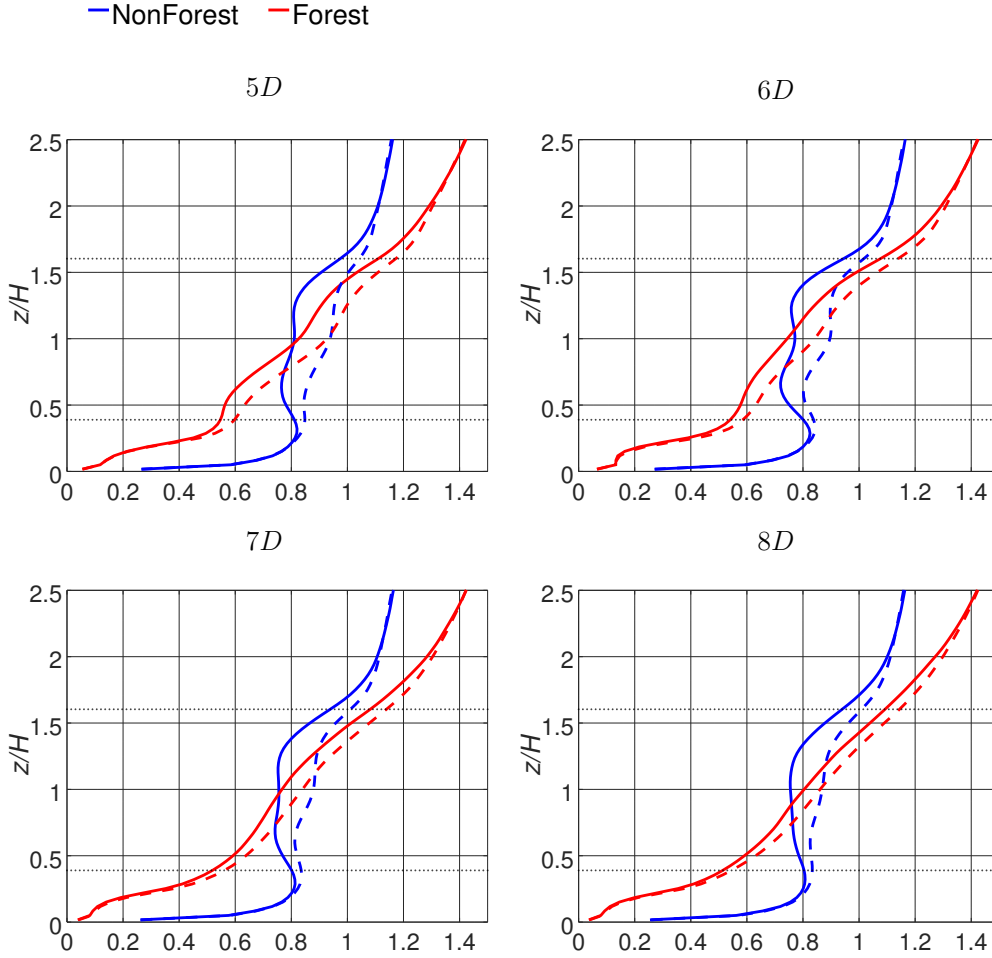
Figure 5.1.5: LES-predicted normalized mean windwise velocity U/U_h profiles at different downwind locations ($5 \leq x/D \leq 8$) in the cases with and without forest. Dashed lines represent the reference, which in the present figure the velocity is the wake of the first turbine.

Figure 5.1.6 shows the deficit between the inflow and wake DU for the cases with and without forest. It can be seen from the figures that at first the difference is larger for the forest case until $x = 2D$ downwind from the first turbine; then at $x = 3D$ it looks similar; DU is smaller at $x = 4D$. This indicates a faster wake recovery in the forest case for the upwind turbine. Similar results are present for the downwind turbine. But in that case, the wake recovery in the case with forest starts even earlier at $x = 7D$, which is $2D$ downwind from the second turbine.
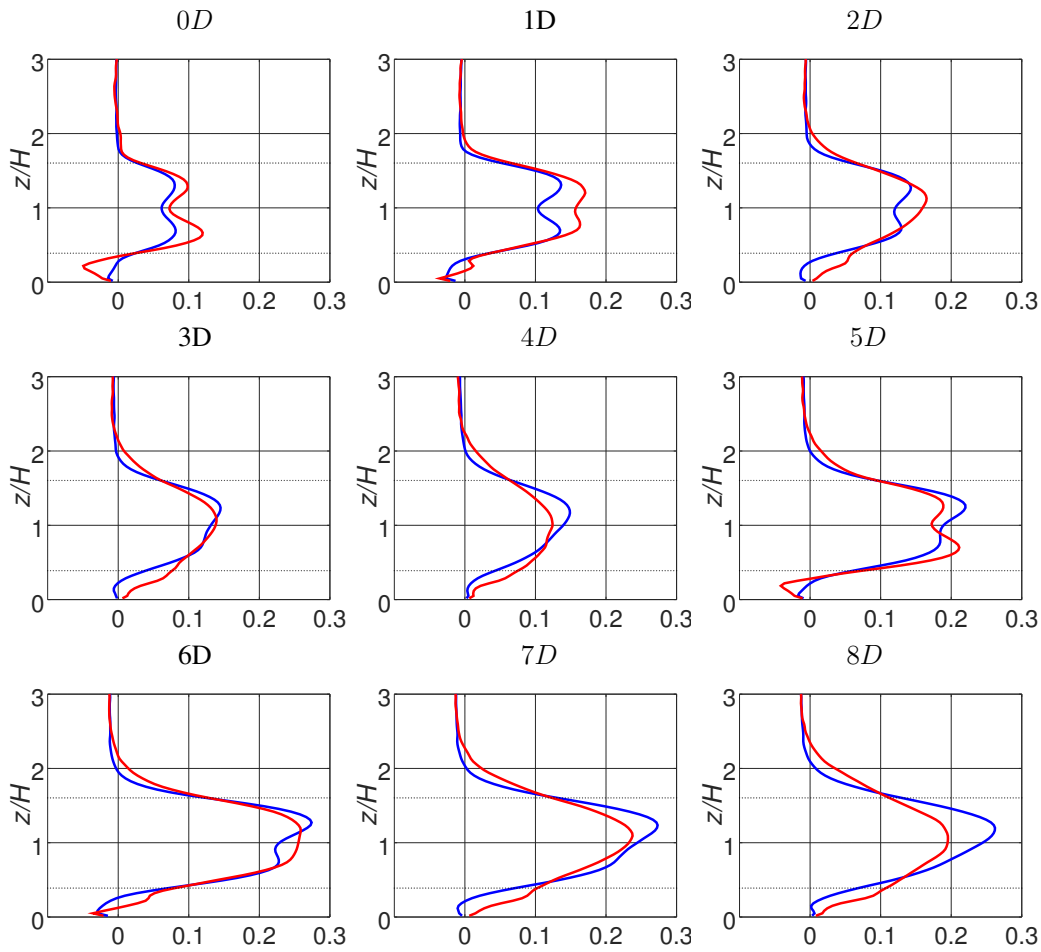
Figure 5.1.6: Velocity deficit DU between the wake and the inflow for the simulation with two wind turbines with and without forest for mean windwise velocity profiles at different downwind locations.

Figure 5.1.7 shows the evolution of the LES-predicted mean windwise velocity deficit and turbulence intensity excess at hub height. As found earlier from Figures 5.1.4 - 5.1.6, the velocity deficit ($\Delta U|_{x=2D} = 16\%$) in the wake of the first turbine is increasing more rapidly in the forest case than in the case without the presence of the forest ($\Delta U|_{x=2D} = 12\%$). Then, it starts to decrease behind $x = 2D$ in the forest case. That is, the wake behind the upwind turbine starts to recover but does not recover completely before it starts to be affected by the downwind turbine. Finally, the wake of the second turbine starts recovering $1D$ behind the downwind turbine. One can notice that the velocity deficit decreases almost linearly in the forest case. If this tendency continues, the wake seems to be fully recovered $16D$ behind the turbine in the forest case. However, the velocity deficit in the non-forest case continues growing in front of the second turbine and starts decreasing only $3D$ behind the second turbine ($x > 8D$). In the non-forest case, the wake seems to be fully recovered not earlier than behind the $20D$ downwind. This is in agreement with the LES study by Schröttle et al. (2016). In that study, the velocity deficit in the forest case almost disappears at $x = 15D$ behind the wind turbine. Similarly to the present study, the velocity deficit predicted by Schröttle et al. (2016) in the non-forest case continues to be high (50% of the highest value of the deficit).

The turbulence intensity excess is very high in the forest case in comparison to the non-forest case ($9\%=\max(\Delta I)=4.5\min(\Delta I)$). It has two peaks at $1D$ behind every turbine. After that, the excess is decreasing. However, in the case without forest the turbulence intensity excess is rather small (less than $3\%=\max(\Delta I)=3\min(\Delta I)$).
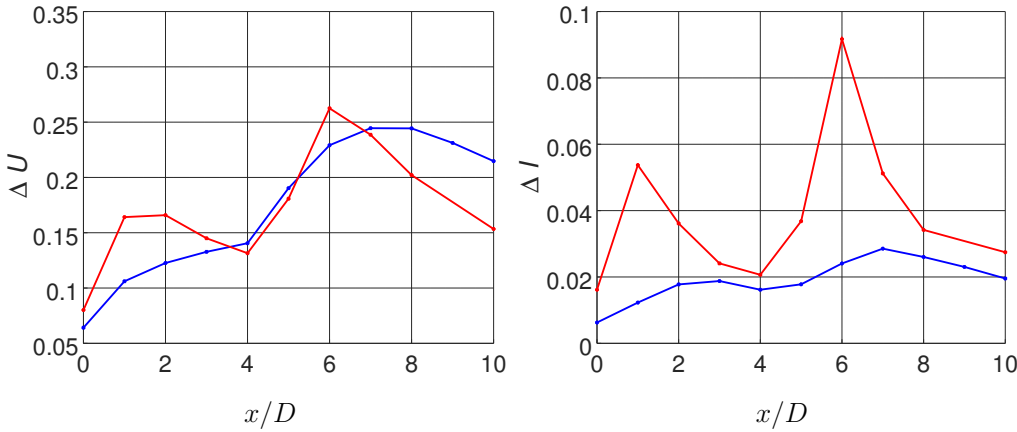
Figure 5.1.7: The LES predicted mean windwise velocity deficit ΔU and turbulence intensity excess ΔI profiles at hub height for different downwind locations ($0 \leq x/D \leq 10$) in the cases with and without forest.

Moreover, tables 5.1.1 and 5.1.2 show the hub-height velocity deficit due to the turbine wakes in comparison to the inflow $DU|_{z=H}$ and the velocity deficit due to the wake of the downwind turbine in comparison to the wake of the upwind turbine $\left|U_{up}^{wake} - U_{down}^{wake}\right|/U_{up}^{wake}$.

It is seen from Table 5.1.1 that the deficit starts to decrease already at $x = 3D$ in the forest case. However, without the presence of a forest, the deficit continuously increases in front of the following turbine. Similar results can be seen in Table 5.1.2 for $\left| U_{up}^{wake} - U_{down}^{wake} \right| / U_{up}^{wake}$. This clearly indicates an earlier wake recovery in the forest case.

Table 5.1.1: Velocity deficit in the wake of the first turbine compared to the inflow at hub height.

	0D	1D	2D	3D	4D
forest	8%	16 %	16.5%	14.5%	13.5%
nonForest	6.3%	10.5%	12.2%	13.2 %	14.1%

Table 5.1.2: Velocity deficit in the wake of the second turbine compared with the first turbine at hub height.

	5D	6D	7D	8D
forest	10.6%	11.5%	8.6%	6.5%
nonForest	13.8%	14.1%	14.2%	13.3%

Following Odemark and Segalini (2014), the local turbulence intensity is defined as:

$$I^{loc} = \frac{\langle u'^2 \rangle^{1/2}}{U_h^{local}},$$

(5.1.1)

where u' is the velocity fluctuations in the windwise direction, $U_h^{local}(x)$ is the local wake velocity taken at $z = H$ (different at every x, unlike in the definition of I from Equation 4.4.3), and the brackets $\langle \rangle$ denote time-averaging.

The local windwise turbulence intensity is presented in Figure 5.1.8 for the forest and non-forest cases. The local turbulence intensity excess due to the forest is shown in Table 5.1.3. The local turbulence intensity is more than two times higher in the forest case. The turbulence intensity prediction from the forest has a similar shape as the intensity in the non-forest case in position $x = 1D$. The difference between minimum and maximum intensity in the swept area of the rotor is approximately the same. Otherwise, in positions further downstream, the intensity above the forest has a smoother shape, probably because the wake in the forest case starts to recover earlier.
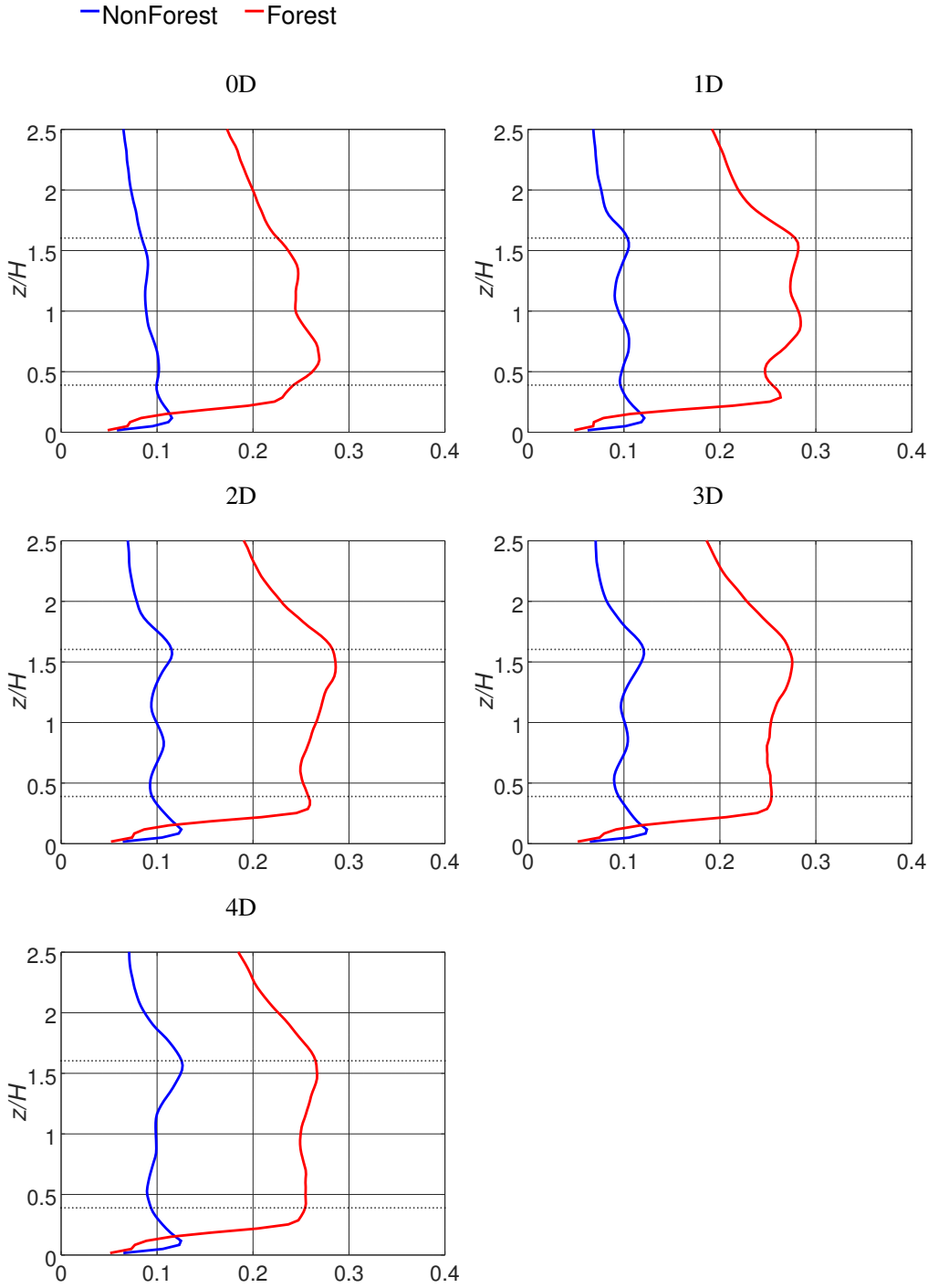
Figure 5.1.8: LES predicted local normalized turbulence intensity I^{loc} profiles at different downwind locations in the cases with and without forest.

Table 5.1.3: Local turbulence intensity excess due to the forest

	0D	1D	2D	3D	4D	5D	6D	7D	8D	10D
I^{loc} excess	176%	201%	171%	154%	154%	164%	201%	155%	142%	147%

The normalized Reynolds shear stress $-\langle u'w' \rangle /U_h^2$ (Figure 5.1.9) obtained in the forest case is extremely high and approximately 10 times higher than the one obtained in the non-forest case. However, in the cases without turbines (see Chapter 3), the difference in the Reynolds shear stresses between forest and non-forest is 7-8 times. That is, the Reynolds shear stress which is already increased by the forest (7-8 times) is also increased by the presence of the turbine in the forest. In contrast to the turbulence intensity, the difference between the minimum and maximum stress in the rotor area is much higher in the case with forest than without forest.

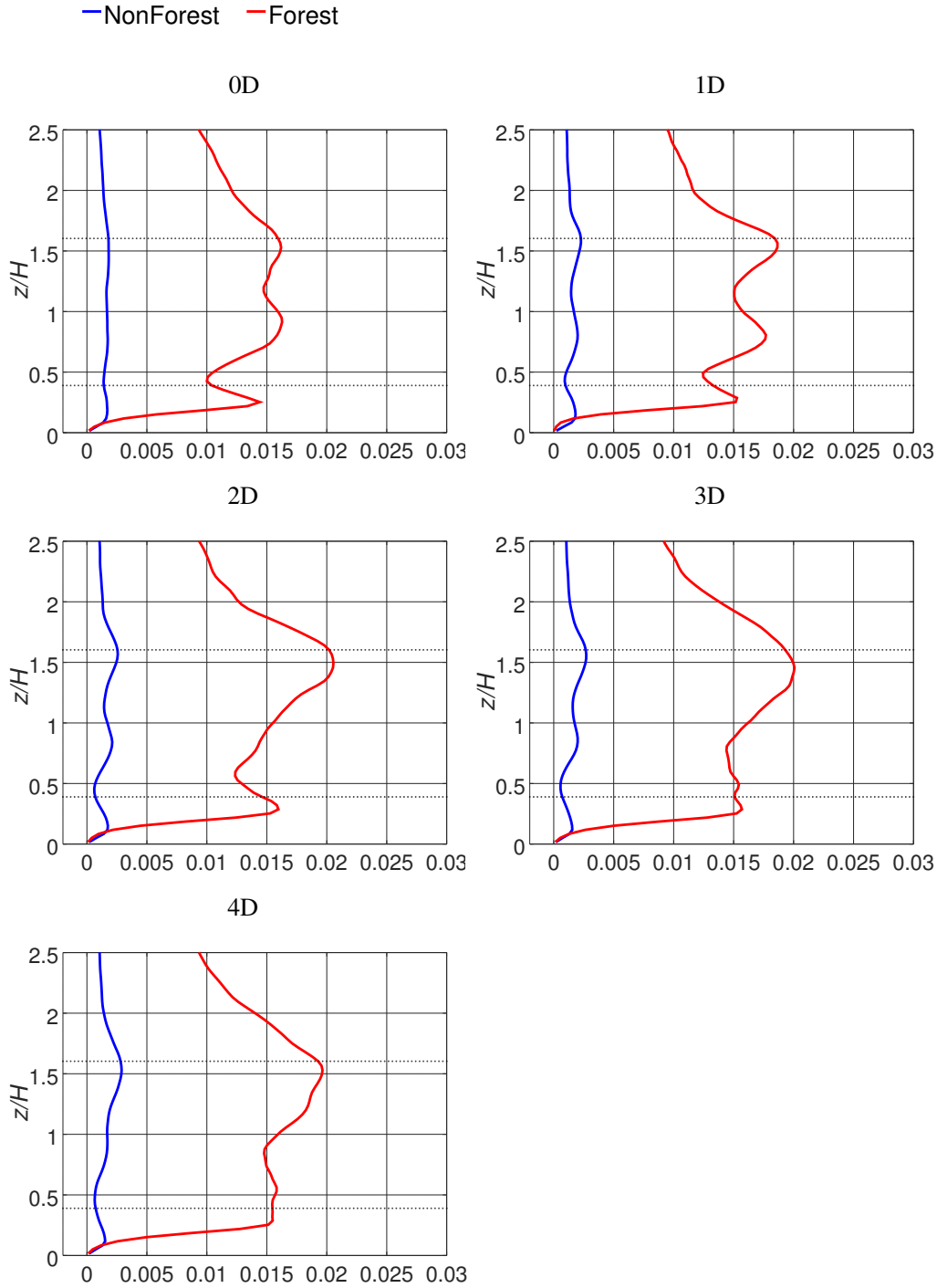Figure 5.1.9: LES predicted normalized vertical Reynolds shear stress $-\langle u'w' \rangle /U_h^2$ profiles at different downwind locations in the cases of with and without forest.

Let us define the deficit of mass flow, energy and power, correspondingly:

$$\Delta \dot{m} = \frac{\int_{-\infty}^{\infty} \int_{-\infty}^{\infty} \left(U_i - U_w \right) dydz}{\int_D U_i dydz} = \frac{\int_{-\infty}^{\infty} \int_{-\infty}^{\infty} \left(U_i - U_w \right) dydz}{\int_{z_h-R}^{z_h+R} \int_{y_h-R}^{y_h+R} U_i dydz}, \tag{5.1.2}$$

$$\Delta E = \frac{\int_{-\infty}^{\infty} \int_{-\infty}^{\infty} \left(U_i^2 - U_w^2 \right) dydz}{\int_D U_i^2 dydz}, \tag{5.1.3}$$

$$\Delta P = \frac{\int_{-\infty}^{\infty} \int_{-\infty}^{\infty} \left(U_i^3 - U_w^3 \right) dydz}{\int_D U_i^3 dydz}, \tag{5.1.4}$$

where U_i is the mean windwise inflow velocity, and U_w is the velocity in the wake regions.

Table 5.1.4: The deficit of mass flow, energy and power for non-forest and forest cases

	0D	1D	2D	3D	4D	5D	6D	7D	8D	9D
$\Delta \dot{m}$	5.0%	8.1%	8.6%	8.6%	9.0%	13.7%	16.9%	16.9%	16.3%	15.5%
$\Delta \dot{m} F$	5.9%	9.9%	9.9%	9.6%	9.7%	14.4%	18.1%	17.2%	16.0%	14.6%
ΔE	9.7%	15.4%	16.2%	16.4%	17.2%	25.3%	30.6%	30.9%	30.1%	29.0%
ΔEF	11.7%	18.7%	18.2%	17.6%	17.8%	26.8%	32.7%	31.1%	29.2%	27.0%
ΔP	14.1%	21.8%	23.1%	23.5%	24.7%	35.3%	41.8%	42.6%	41.9%	40.9%
ΔPF	16.9%	26.0%	25.6%	24.7%	25.2%	37.5%	44.9%	43.5%	41.3%	38.7%

Table 5.1.4 shows the deficit of mass flow, energy and power. As one can see from Table 5.1.4, the deficit of mass flow, energy and power from the inflow is larger in the forest case at almost every position except the last two where $x = 8D$ and $x = 9D$. This can be due to the earlier wake recovery in the forest case.

Figure 5.1.10 presents the wind shear α for both cases. Wind shear is calculated from the formula:

$$\frac{U}{U_h} = \left(\frac{z}{H} \right)^{\alpha}. \tag{5.1.5}$$

In the figure, the dashed line denotes profiles of "local" shear α estimated using following equation:

$$\alpha = \frac{H}{U_h} \left(\frac{\partial U}{\partial z} \right). \tag{5.1.6}$$

To calculate the value of so-called "global" shear (across the rotor disk area, dotted values), the equation below is used:

$$\alpha = \frac{H}{U_h} \left(\frac{U_{tip}^{up} - U_{tip}^{low}}{z_{tip}^{up} - z_{tip}^{low}} \right). \tag{5.1.7}$$

As one can see from the figure, the wind shear (both "local" and "global") in the forest case is larger than in the case without forest. The global value of shear for the downwind turbine (α=0.57) is slightly higher than for the upwind one (α=0.52) in the forest case.
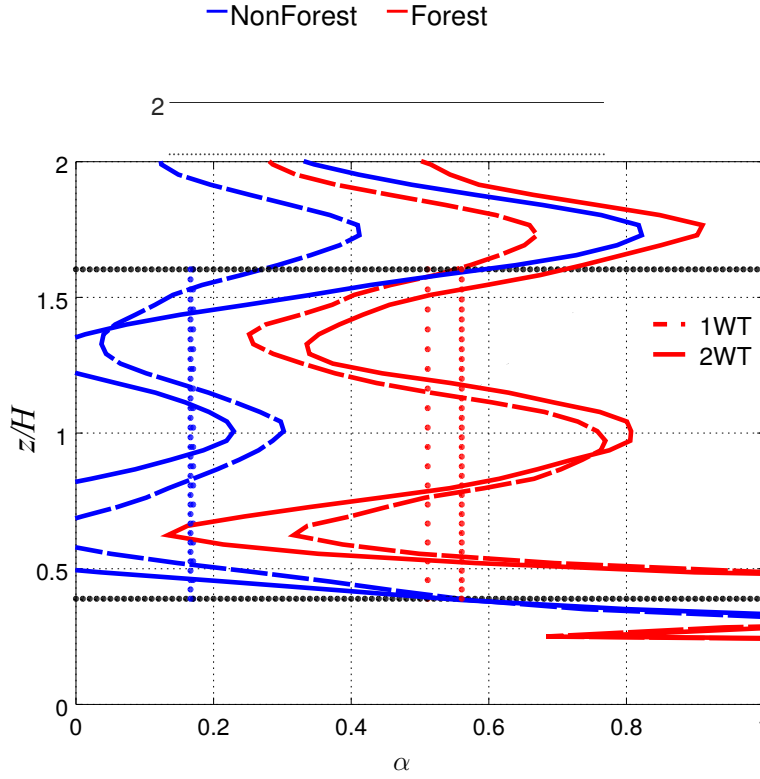
Figure 5.1.10: Shear α for the cases with and without forest. Solid lines represent the profiles of "local" shear for downwind WT, and broken lines ($\cdot\cdot$) represent upwind turbines. Dotted vertical lines (sparse and dense) represent the "global" wind shear for the 1WT and 2WT, respectively.

However, in case without forest the values are equal (α=0.165). The shear obtained in the case without a wind turbine is α=0.14 and α=0.48, respectively, for non-forest and forest cases. Thus, the wind shear is slightly influenced by the presence of the wind turbines.

The time-dependent power coefficient C_P is the ratio of the shaft power produced by the wind turbine divided by the available wind power into the turbine (P_{avail}). Overall turbine efficiency (C_P) is defined as a product of aerodynamic (or turbine), mechanical and electrical efficiencies (η_t, η_m and η_e, respectively). The efficiency with which the blades convert available wind power into mechanical shaft power (P_{actual}, which could be predicted by the ALM) is called the aerodynamic efficiency. Loss in the aerodynamic efficiency is the largest among all three efficiencies. At the same time, the aerodynamic efficiency is the only one predictable by the ALM and the only efficiency that can be affected by the forest. Thus, for simplification, a system close to ideal (that is, mechanically and electrically efficient with only aerodynamic power loss) is considered in this paper. Therefore, the equation for time-dependent power coefficient yields:

$$C_P(t) = \frac{P_{actual}(t)}{P_{avail}}. \tag{5.1.8}$$

P_{avail} is the total available wind power:

$$P_{avail} = \frac{1}{2}\rho\pi R^2 U_{avail}^3, \tag{5.1.9}$$

where U_{avail}^3 is defined according to the equation below:

$$U_{avail}^3 = \frac{1}{2R}\int_{H-R}^{H+R} U^3(z)dz, \tag{5.1.10}$$

where R is the radius of the rotor, $R = D/2$.

P_{actual} is the actual mechanical shaft power produced by one turbine. It is calculated as a mean of $P_{actual}(t)$ for more than 1000 turbine rotations. The time series of the power curve of P_{actual} and power coefficient C_P can be seen in Figures 5.1.11 and 5.1.12. It is seen from the figure that the available power is non-stationary for the forest. However, in the simulation the flow is already fully developed after 7000 s. The uncertainty in the power can happen, for example, due to the too-short buffer zone. The figures show that the power produced by the turbine in the case without forest is bigger than in case with forest, which is obvious because of the slightly higher velocity at hub height in the case without forest (8.96 m/s in the non-forest case compared to 7.8 m/s in the forest case) . At the same time, the power coefficient is estimated to be 0.22 (0.28 for the downwind turbine) and 0.31 (0.37) in the non-forest case and forest case, respectively. It was also found in the wind-tunnel experiment by Odemark and Segalini (2014) that C_P in the case forest case is slightly higher.
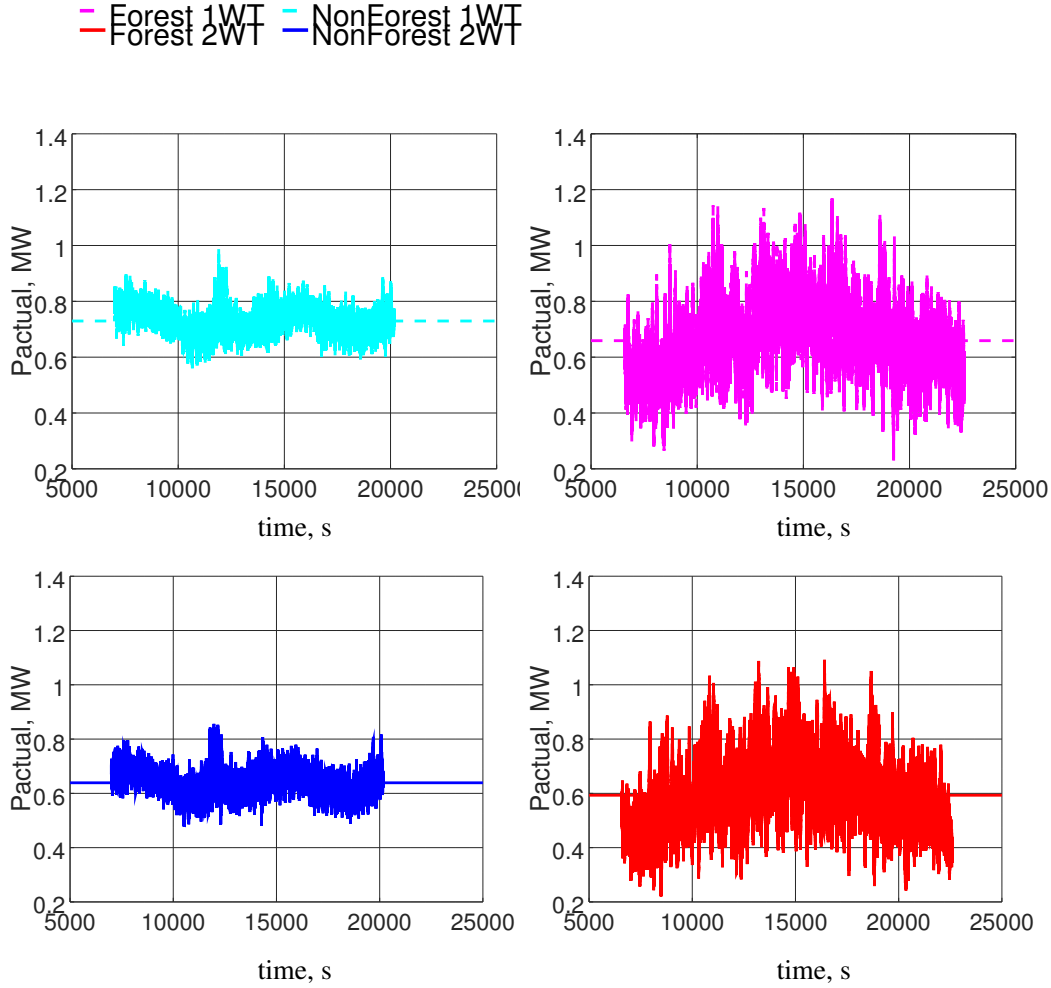
Figure 5.1.11: Time series for actual mechanical shaft power produced by the turbines for cases without (left) and with forest (right). The horizontal lines show $P_{actual} = \text{mean}(P_{actual}(t))$.
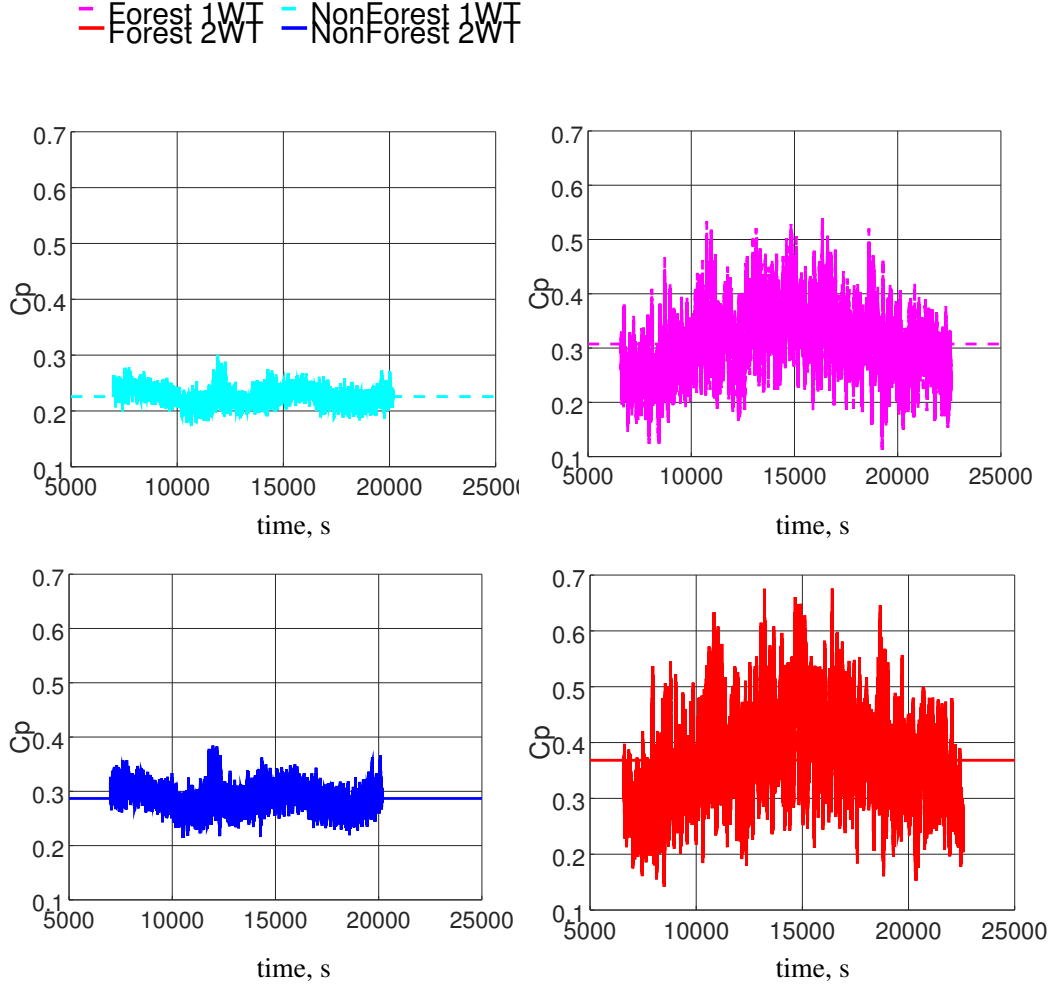
Figure 5.1.12: Time series for the power coefficient for cases without (left) and with (right) forest. The horizontal lines show $C_P =$mean$(C_P(t))$.

However, the difference between the power coefficients in the cases with and without forest is decreasing if U^3_{avail} is calculated as follows:

$$U^3_{avail} = \frac{1}{4R^2} \int_{H-R}^{H+R} \int_{y_{hub}-R}^{y_{hub}+R} U^3(y,z)dydz, \qquad (5.1.11)$$

where y_{hub} is the crosswind coordinate of wind turbine location.

The available power calculated in this way is equal to $P_{avail} = 3.57$ MW and $P_{avail} = 2.76$ MW for the first and following turbine, respectively, in the non-forest case. The available power in the forest case is $P_{avail} = 2.36$ MW and $P_{avail} = 1.9$ MW for the first and following turbine, respectively. Therefore, the power coefficient, which is obtained

by the total available power in the swept area of the rotor, is 0.2 (0.23 for downwind WT) and 0.29 (0.32) for the non-forest and forest cases, respectively.

Let us define the following quantities:
power loss due to forest

$$\left| \frac{P^{forest} - P^{nonForest}}{P^{nonForest}} \right| * 100\% \tag{5.1.12}$$

aerodynamic (turbine) power loss

$$\left| \frac{P_{actual} - P_{avail}}{P_{avail}} \right| * 100\% \tag{5.1.13}$$

Table 5.1.5: Comparison of power obtained in cases with and without forest. Aerodynamic power loss and power losses due to the forest.

	forest	forest	non-forest	non-forest	power due to	losses forest
	1WT	2WT	1WT	2WT	1WT	2WT
P_{avail}	2.14 MW	1.61 MW	3.23 MW	2.22 MW	34%	28 %
P_{actual}	0.66 MW	0.59 MW	0.73 MW	0.64 MW	9.7%	7.2%
aerodynamic power loss	69%	63 %	78%	72%		

The comparison of power obtained in the non-forest and forest cases, aerodynamic power losses and power losses due to the forest for upwind and downwind turbines are represented in Table 5.1.5. This table shows that aerodynamic loss in the case without forest is bigger than in the case with forest. Loss of actual shaft power due to the forest consists of only 9.7% for the upwind and 7.2% for the downwind turbine while the loss of available power due to the forest is nearly 30%.

5.1.3   Conclusion

A comparison of the results obtained in the case with two wind turbines in tandem and with and without forest is shown. In order to perform such a LES with wind turbines and forest, a longer computational domain and smaller time-step than in the non-forest case are used. First of all, the wake starts recovering earlier in the forest case than in the non-forest case. This can be useful in a closer placing of the wind turbines in a forested wind park in comparison to a non-forest one. The wake above the forest is shorter but wider. Thus, wind turbines can be placed closer in the windwise direction. The forest generates a rather high velocity above the turbine upper tip (and slightly higher than the hub-height velocity behind the wake in the crosswind direction) than it is in the non-forest case. The turbulence intensity (25-28%) is very high in the forested wind park. The vertical Reynolds shear stress is extremely higher (10 times) than in the case without

forest. The high turbulence intensity probably helps in the faster wake recovery in the forest case. The wind shear ($\alpha > 0.52$) is very strong in the forest case. For the reference, the wind shear is equal to 0.16 in the non-forest case. The most recent safety standards (IEC, 2005) are given so far for the wind above flat terrain without forest. That suggests that if such a wind turbine is located in the forested wind park, then it can most probably be broken earlier. Unfortunately, the performed cases have slightly different velocity at hub height. That is, the power produced in the forest case is smaller than in the non-forest case. However, the power coefficient is significantly higher most probably because of the stronger wind shear in the forest case and also because of a faster wake recovery in the forest case. The power losses due to the forest for the downwind turbine (7.2%) is smaller than for the upwind turbine (9%). This suggests that for an infinite wind park, the power loss can be even smaller. And a wind turbine located far downwind in an infinite wind park may produce almost the same power as it does without a forest.

5.2   Large wind turbine array

In this section, the effects on the mean wind speed, turbulence and power production due to the forest are discussed for an infinitely large wind farm.

5.2.1   Numerical setups

In the present simulations, the same wind turbine as above has been modelled (the tower height H is 90 m and the turbine rotor diameter (D) is 108 m). The airfoil type of the reference turbine blade is not known. Therefore, for simplification in this work the blade is represented by a NACA0012 airfoil. The average velocity calculated at the hub height (for any position x) $\mathrm{mean}|_x(U_h^{loc})$ is 8.73 m/s in the non-forest case. The rotational speed Ω is 7.5 rpm. In the current forest simulation, canopy characteristics (the same forest-canopy as before), such as canopy drag coefficient C_D =0.15 and LAD $\alpha(z)$, are taken from Shaw and Schumann (1992). The leaf-area index (LAI) in that case is equal to 2. The height of the forest (h) is 20 m.

The Reynolds number ($Re_D = U_h * D/\nu$) based on the rotor diameter D and the incoming velocity at hub height U_h is 6.0×10^7. The computational domain is a rectangular block with a height of $4D$. The length and width of the computational domain are $15D$ and $10D$, respectively. The simulation over six wind turbines is performed on a 4 m resolution grid. The computational grid, created using the "blockMesh" utility in OpenFoam, consists of $56\,424\,600$ finite element cells. Local refinement of the grid (up to 2 m) at the bottom part ($z < 2H$) of the computational domain is applied. The distance between the turbines in the array is set to $5D$ in the windwise and crosswind directions. The simulation is performed with periodic inlet-outlet boundary conditions in OpenFoam by fixing the momentum source term g. In order to get approximately the same velocity at hub height U_h as in the case without forest, g is chosen to be 0.004 $\mathrm{m/s}^2$ ($\mathrm{mean}(U_h^{loc}) = 7.86$) and 0.0013 $\mathrm{m/s}^2$ ($\mathrm{mean}(U_h^{loc}) = 8.73$) for cases with and without forest, respectively. The simple rough logarithmic ABL model is employed as the wall function model. (For detail see Chapter 2.)

In both simulations, the automatic time step by fixing the Courant number in the entire domain to 0.1 is used. Therefore, the time step is approximately equal to 0.025 s in the non-forest case and 0.019 s in the forest case. The flow is fully developed and averaged over more than 4.5 hours, which is the equivalent of approximately 2000 turbine rotations.

5.2.2   Results and discussion

In the present section, LES is performed over six turbines located on flat terrain without forest and with forest separately in order to identify the effects created by the forest. In fact, due to the periodic boundary conditions an infinitely large wind farm is simulated .

In contrast to the 2WT cases, some of the profiles are normalized by the local hub height velocity because of the absence of the inflow. The reference cases (the same domain but without turbines) were also performed; however they do not give zero velocity deficit $(U^{ref} - U^{wake})/U^{ref}$ at a rather high z as it is in the case of 2WT. Thus, the results of the reference cases are not present in the figures. However, the hub-height velocity from the reference cases (the approximate $U_h^{ref} = U_h$=8.9 m/s for the non-forest case and U_h=8 m/s for the forest case) is sometimes used in order to compare results of the present cases with 2WT cases. Figure 5.2.1 shows the contour plot of mean velocity on the horizontal $x - y$ plane (top view) at the turbine hub height ($z = H$) in the case without forest (top) and with forest (bottom).
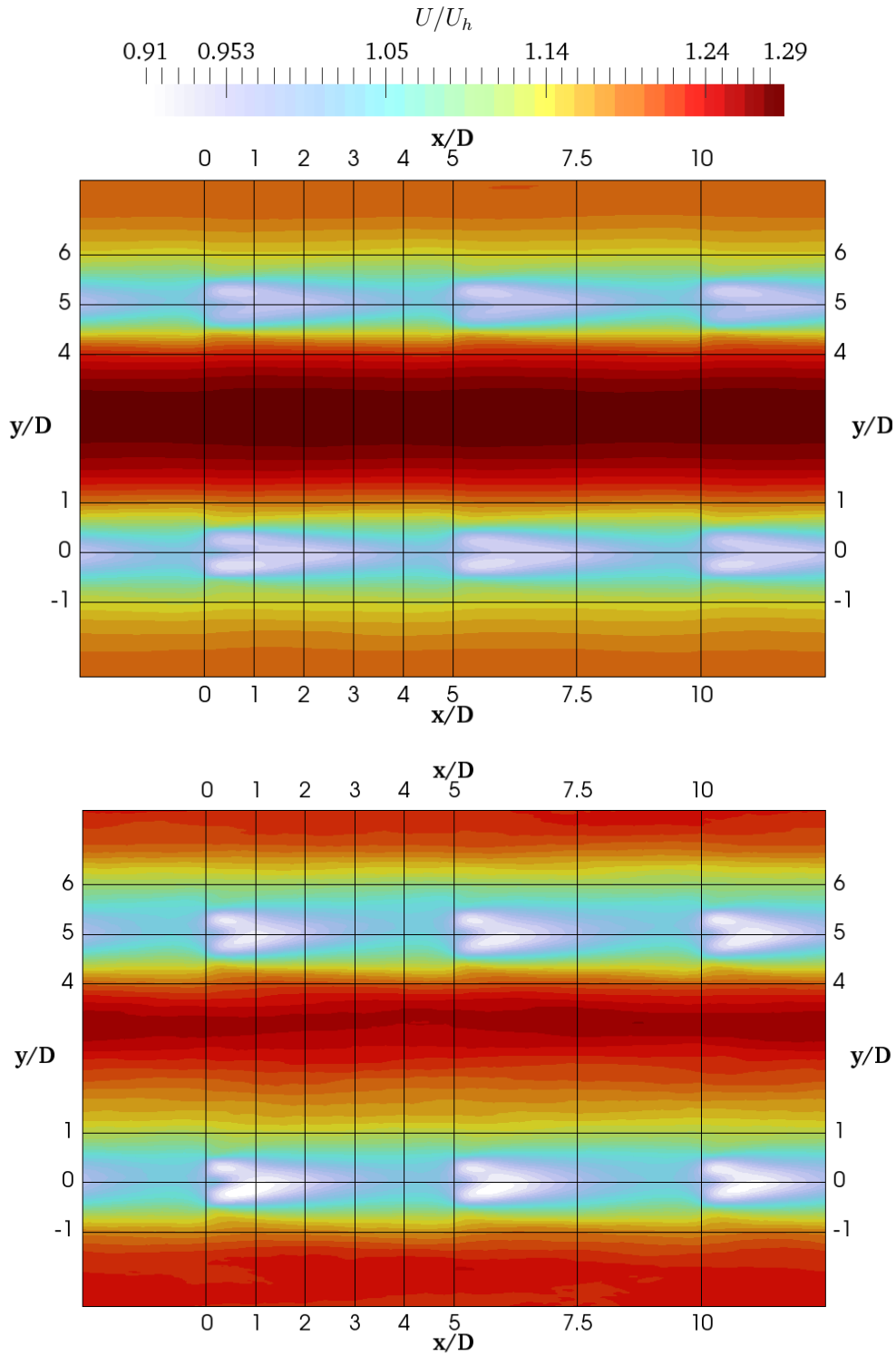
Figure 5.2.1: Top view of the normalized mean windwise velocity in the cases without (top) and with forest (bottom).

In both cases, the mean velocity U is normalized by the hub height mean velocity (U_h). Here and below, U should be understood as the mean velocity in the windwise direction. From the illustrations in this figure, one can observe that the wake starts recovering earlier in the forest case. The wake is already weak at $x = 3D$ behind the turbine in the forest case and becomes very weak after $x = 4D$ just in front of the following turbine, while in the non-forest case, the wake does not disappear in front of the next turbine. This observation is in line with Barlas et al. (2016). It can also be seen from Figure 5.2.1 that the wake in the forest case is wider in the crosswind direction than in the non-forest case.

Figure 5.2.2 represents the contour plot of the vertical $x-z$ side view taken at the first row of turbines ($y = 0$) without (top) and with (bottom) forest. It indicates similar results as in Figure 5.2.1. The wake above the forest is not clearly seen in the picture. It apparently disappears in the visualization within the rather strong forest-generated mean wind shear.
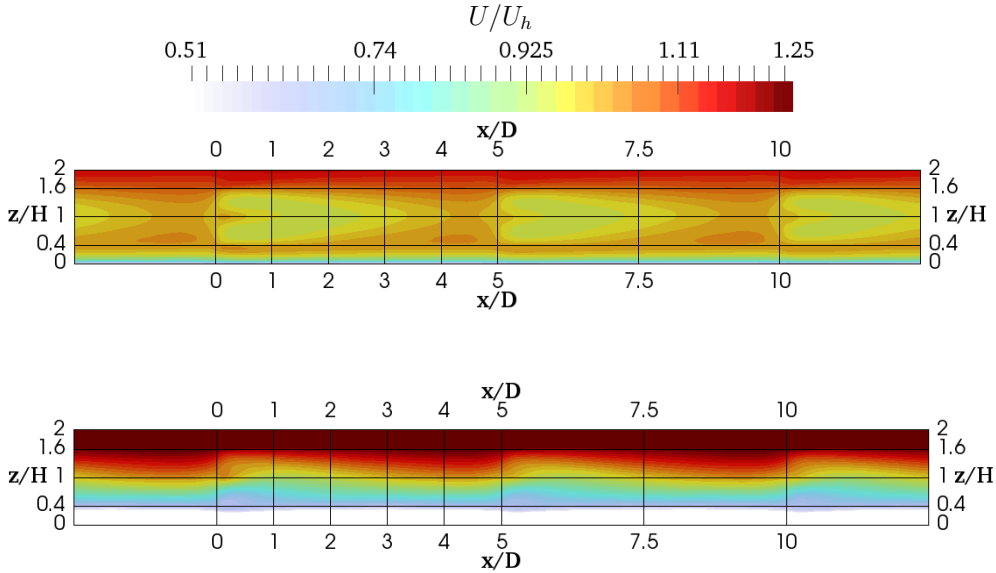
Figure 5.2.2: Side view of contours at the first row of turbines ($y = 0$) of normalized mean windwise velocity for the cases without (top) and with forest (bottom).

The vertical profiles of the mean velocity normalized by local hub height velocity (U_h^{loc}) at different windwise locations after a turbine are presented in Figure 5.2.3. The recovery of the wake velocity is faster in the forest case, which proves the results described above. High wind shear in the forest case and small one in the non-forest case are seen from the figure.

Figure 5.2.4 and Table 5.2.1 show the turbulence intensity excess due to the forest effects $\left| I_{z=H}^{loc,forest} - I_{z=H}^{loc,nonForest} \right| / I_{z=H}^{loc,nonForest} * 100\%$. Generally speaking, I^{loc} is much higher

in the forest case, reaching more than double in 3 out of 5 locations compared to the non-forest case. The calculated value is smaller than the one reported in Nebenführ and Davidson (2014), where the turbulence intensity of the windwise velocity component reaches 19.2% in the forest and 8.6% (or 131% of the deficit) without forest at the hub height of an imaginary turbine. At the same time, the obtained values of I^{loc} (25-27%) at the turbine location ($x/D = 0$) in the forest case are almost two times higher than the maximum value (16%) suggested by IEC for wind turbine design (Nebenführ and Davidson, 2014).

Table 5.2.1: Turbulence intensity excess due to the forest at turbine hub height ($z = H$) for different downstream positions from $x = 0D$ to $x = 4D$

	0D	1D	2D	3D	4D
I^{loc} excess	105%	135%	57%	100%	45%

Figure 5.2.3: LES-predicted normalized mean velocity U/U_h^{loc} profiles at different wind-wise locations in the cases without and with forest. The profiles are also averaged at each respective locations for all six turbines. The black dotted lines denote the top ($z = H + D/2 = 1.6H$) and bottom tip ($z = H - D/2 = 0.4H$) of the wind turbine.
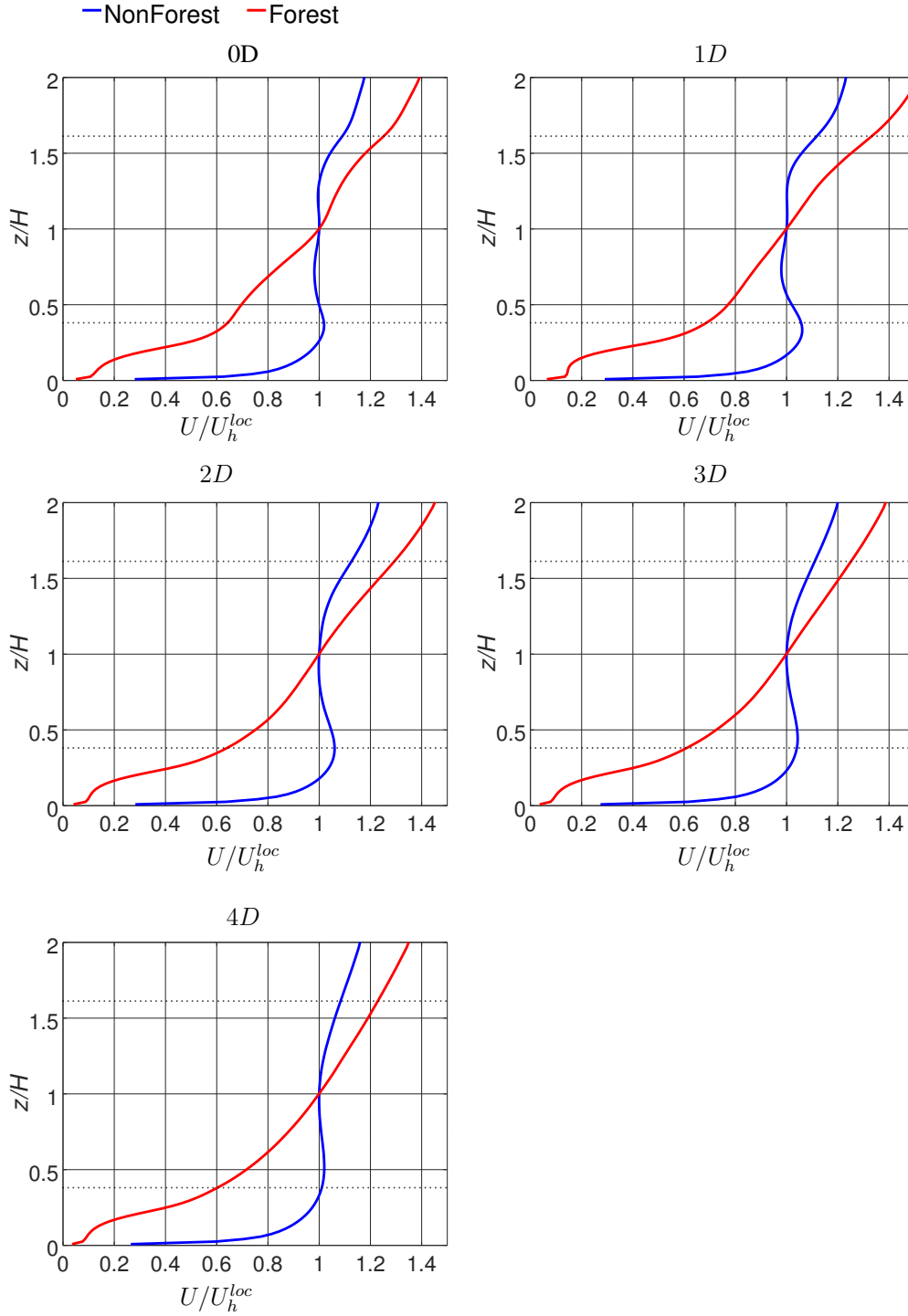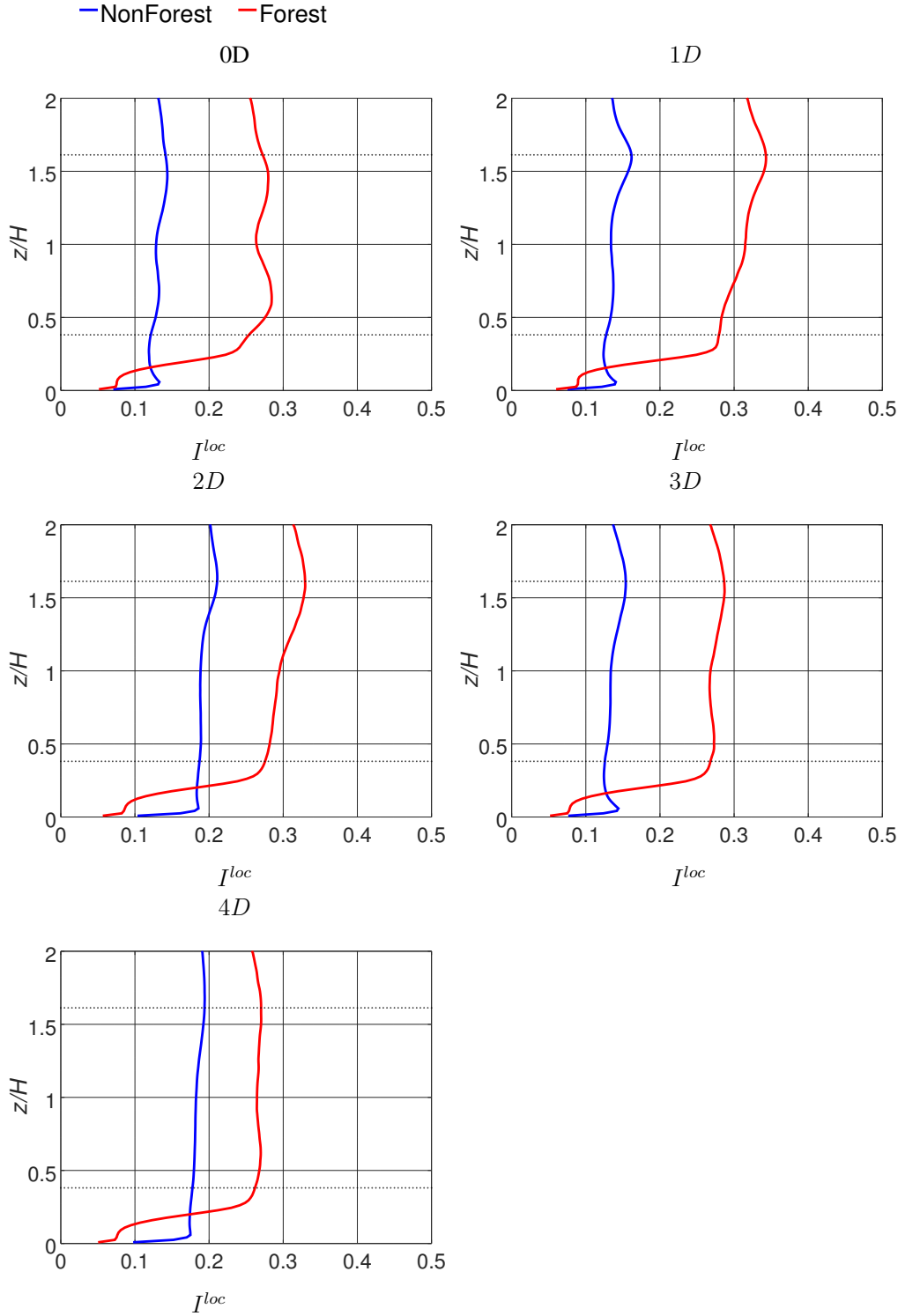
Figure 5.2.4: LES-predicted normalized turbulence intensity I^{loc} profiles at different windwise locations in the cases without and with a forest. The profiles are also averaged at each respective locations for all six turbines.

The global wind shear $\alpha = 0.53$ obtained in the forest case is ten times higher than the non-forest value. The value obtained in the forest case agrees very well with the value estimated at hub height by Odemark and Segalini (2014) ($\alpha = 0.5$). The shear in the present case with a forest (an infinitely large wind farm) is close to the value obtained in the case of 2WT and forest for the upwind turbine ($\alpha = 0.52$, upwind turbine) but slightly smaller than the one obtained for the downwind turbine ($\alpha = 0.57$, downwind turbine). However, the value in the non-forest case ($\alpha = 0.054$) is approximately three to four times smaller than in the ones obtained in the non-forest case without turbines ($\alpha = 0.14$), 2WT ($\alpha = 0.165$) and by Nebenführ and Davidson (2014) ($\alpha = 0.19$). This seems to be due to the infinite turbine wake that extends much higher in the forest case. The wake was not considered in the above-mentioned LES study by Nebenführ and Davidson (2014).

The actual mechanical shaft power P_{actual} is calculated as a mean of $P_{actual}(t)$ for more than 550 turbine rotations. The time history of the power coefficient and actual power can be seen in Figure 5.2.5. Figures show power produced by the turbine in the case without forest is larger than in case with forest which is because of slightly higher wind speed (especially, in lower part $z < H$) in the non-forest case than in the forest. At the same time, the mean power coefficient is estimated to be 0.24 and 0.2 in the case with and without forest, respectively. In the wind-tunnel experiment by Odemark and Segalini (2014), the C_P in the forest case is slightly larger (by 3%). It is assumed in Odemark and Segalini (2014) that the increase in C_P, as compared to the case without canopy, could be because of the increased turbulence, mean wind shear, or a combination of both. The fact that the present LES, performed on a real scale with a much higher Reynolds number, also gives a similar increase in C_P in the forest case, suggesting that the high wind shear might be the main reason for the increase.

Figure 5.2.6 shows the comparison between the averaging of the available power calculated in a different time from the instantaneous windwise velocity ($\langle P_{avail}(u,t) \rangle$) and the mean available power calculated from the mean windwise velocity. The relative difference between these two values is only 5% which shows that the power coefficient C_P in the forest case is larger than in the non-forest case and not because of the higher level of turbulence in the forest case.

Table 5.2.2: Comparison of power obtained in the non-forest and forest cases. Turbine losses for the forest and non-forest cases and power losses due to the forest for available and actual power.

	forest	nonForest	losses due to forest
P_avail	2.78 MW	4.03 MW	31 %
P_actual	0.68 MW	0.82 MW	18 %
aerodynamic losses	76 %	80%	

The comparison of power obtained in the non-forest and forest cases, aerodynamic power

losses and power losses due to the forest are represented in Table 5.2.2. This table shows that aerodynamic loss in the non-forest case is higher than in the case with forest. The loss of actual shaft power due to the forest consists of only 18%, while the loss of available power due to the forest is 31%.
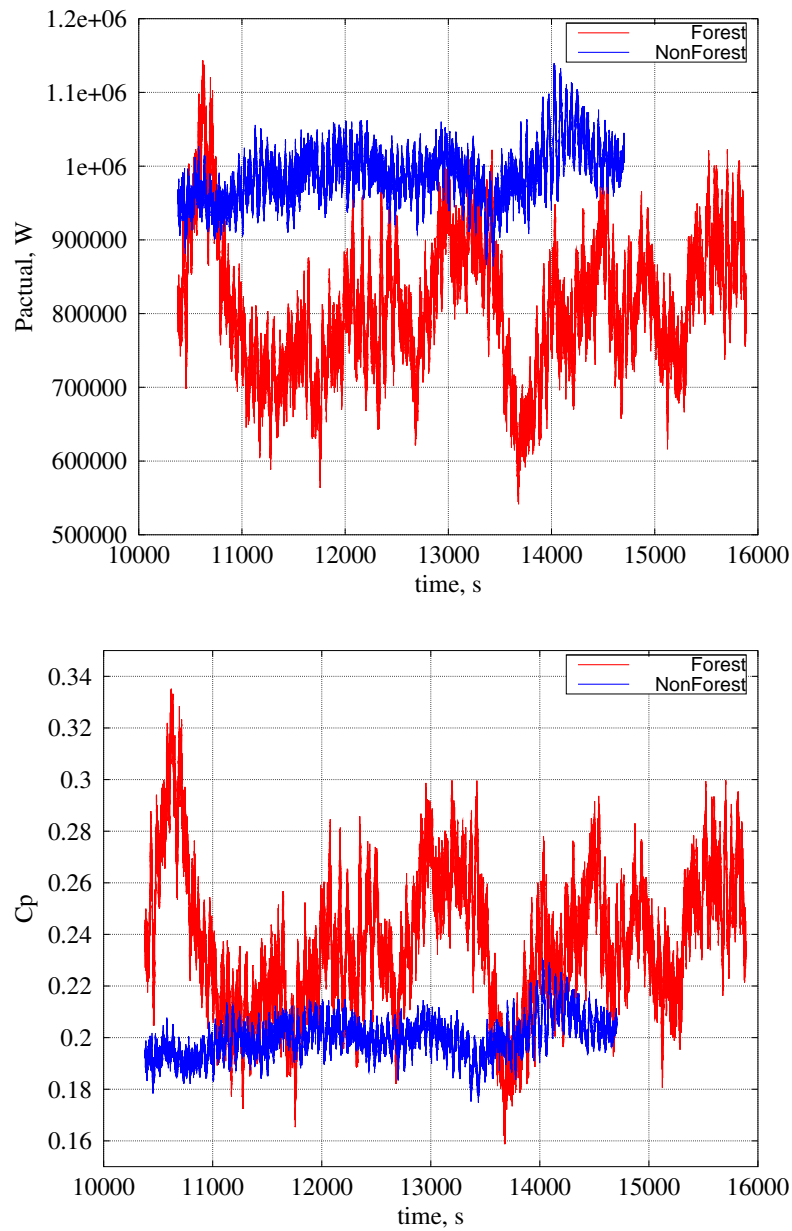
Figure 5.2.5: Time series for actual shaft power produced by the turbine (top) and power coefficient (bottom) for cases without and with the forest
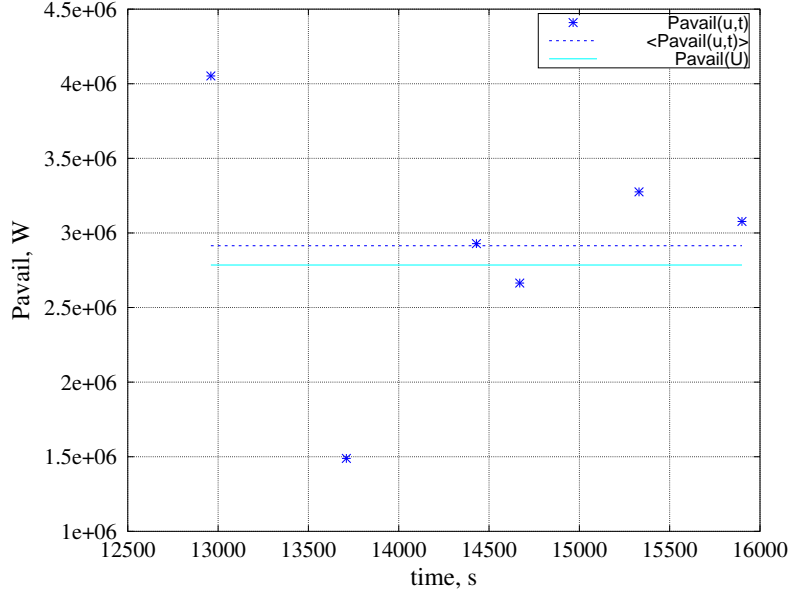
Figure 5.2.6: Available power $P_{avail}(u,t)$ calculated at different times, which is represented as blue (*), average of $P_{avail}(u,t)$ (blue broken line) and mean (total) available power $_{Pavail}(U)$ (cyan line) for the case with forest.

5.3 Forest effect on the blade angle of attack

In the final section of this thesis, one practical application of the present research is considered. As shown in Chapter 5, forest has a large impact on the wind flow and kinetic energy, which is then converted to mechanical shaft power by turbine blades and further to electrical power. It was noticed previously that when a turbine blade reaches the lower part of the domain ($z < H$), the forest has the largest effect on the power production. Let us take a deeper look into the mechanisms of power production from the wind. It is known that the power is created by the torque (azimuthal force (f_a^θ)) and the azimuthal force is generated by the lift and drag forces which force the blades to rotate : $f_a^\theta = L\sin(\phi) - D\cos(\phi)$. It is obvious that the maximum azimuthal force is reached when the first term is large and the second one is small. The lift and drag forces are created by the velocity relative to the blades which is a combination of the incoming wind speed and the angular velocity of the blades (see Figure 4.3.1). The lift and drag forces are functions of relative velocity, chord length and the lift $C_l(\alpha)$ and drag $C_d(\alpha)$ coefficients, respectively, where α is the angle of attack. It can be seen from Figure 5.3.1 that the azimuthal aerodynamic force is optimal in this case when $10 < \alpha < 15$ so that the lift coefficient $1.1 < C_l < 1.5$ and at the same time C_d is small.
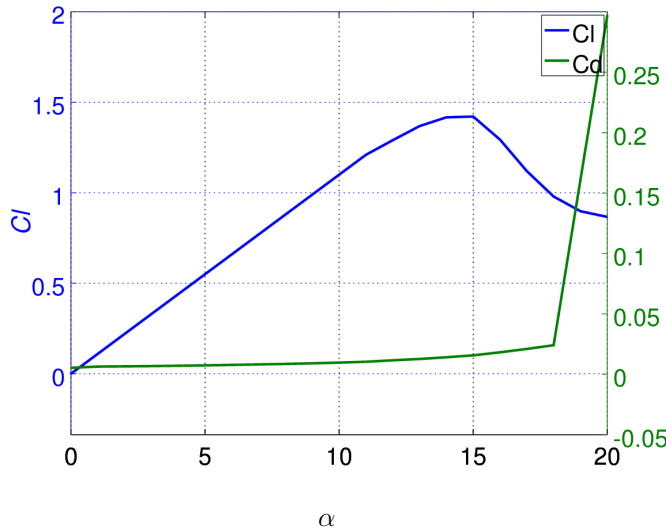
Figure 5.3.1: Aerodynamic force coefficients of the NACA0012 airfoil.

Figures 5.3.2 and 5.3.3 show the instantaneous angle of attack at two different azimuthal angles ($\theta = 240^o$ and $\theta = 300^o$, respectively) for the non-forest and forest cases. It can be seen from the figures that the angle of attack is different for different blades in the forest case, and it is almost the same for all three blades in the non-forest case. The main interest is the area of the blade where $10 < \alpha < 15$, thus $25 < r < 55$. In the forest case, at $r > 35$ the values of angle of attack are below 10°.
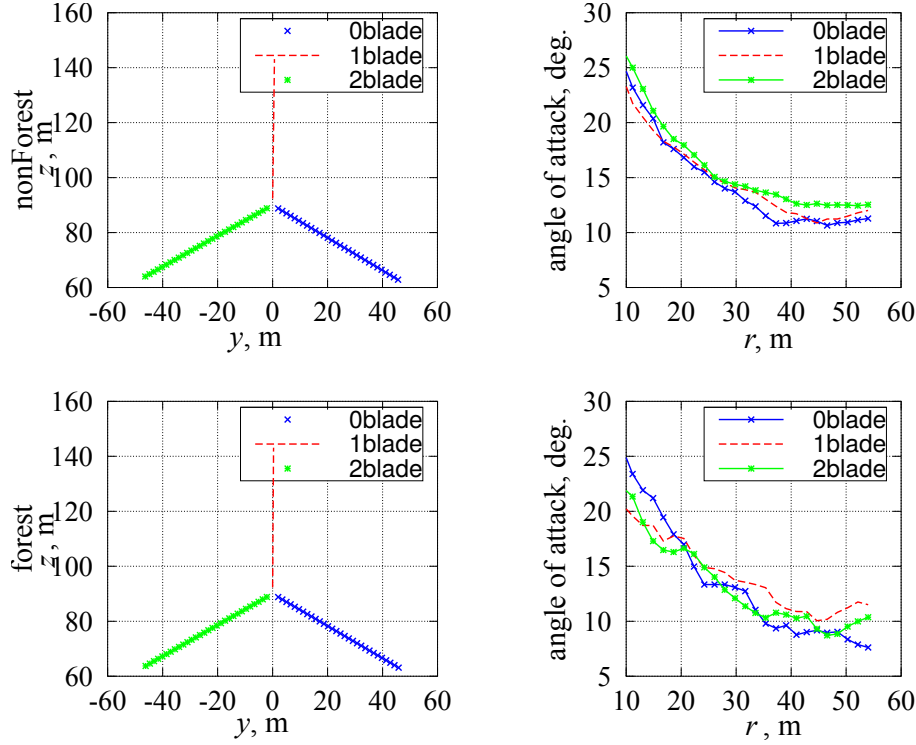
Figure 5.3.2: Blade positions (left) and angle of attack at azimuth = 240° (right).

It can also be seen from Figure 5.3.4 that the angle of attack is optimal only for radial positions of the blade close to the tip $r = 35$ and at the tip $r = 54$ in the non-forest case. However, in the forest case α has much larger variations in comparison to the non-forest case, especially near the tip. The angle of attack in the forest case is no longer optimal at $r = 35$ m and $r = 54$ m. α decreases below 10° because of large variations. It is assumed that α drops below 10° when at least one of the blades is located in the lower part of the area swept by the blades ($z < H$). (See Figures 5.3.2 and 5.3.3.)

It was investigated in the previous section that loss of actual power due to the forest in comparison to the non-forest case consists of 17.7% (in the case of a large wind turbine array). It is shown above in this section that the non-optimal angle of attack is responsible for the loss. Remember that the angle of attack $\alpha = \phi - \gamma$, where ϕ is the flow angle and γ denotes the collective angle which is the sum of the local mounting pitch (φ) and the design twist ($\psi(r)$) angles. The last equation brings up the idea of possible changes of α by an active control of pitch φ. At the moment, the pitch in real turbines is set for different (reference) mean-wind speeds to some constant value. It is only changed in order to shut down the turbine if extremely high wind is expected.
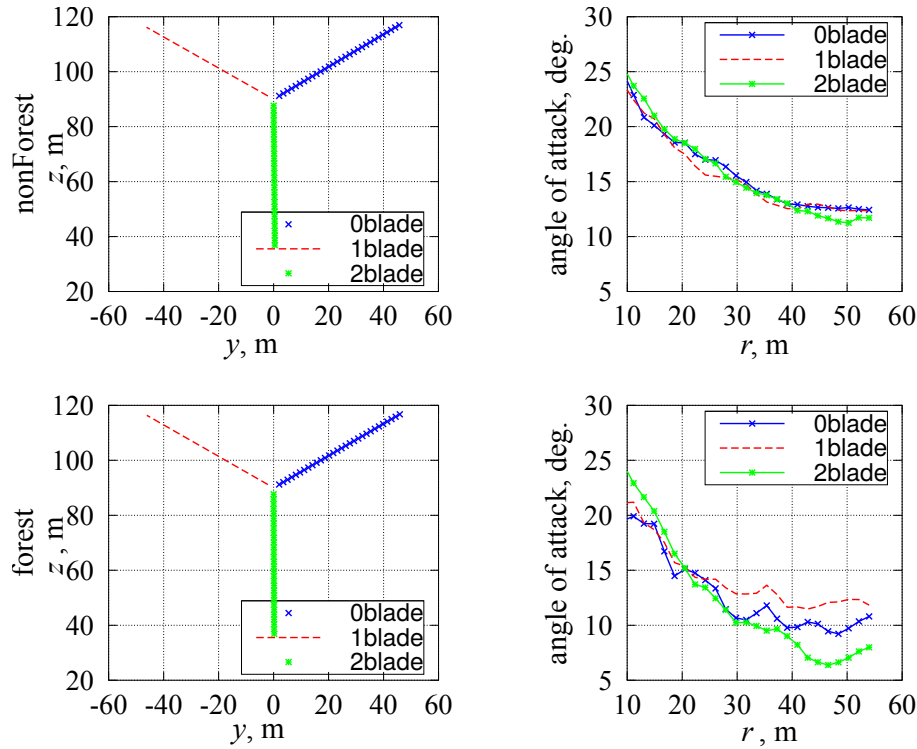
Figure 5.3.3: Blade positions (left) and angle of attack at azimuth = 300°.

The main idea of the active pitch control is not to try to control the pitch angle according to the turbulent fluctuations in the approaching wind as a function of time. It seems to be very expensive and difficult to arrange suitable continuous wind speed measurements slightly upstream of the turbine for all wind directions. However, the idea is to try to implement the pitch control as a function of azimuthal angle in order to follow the variation of the mean wind speed arising from the strong vertical wind shear. As shown in Figure 5.3.4, the pitch in the forest case becomes non-optimal especially when the closest points to the tip ($r > 35$) are located in the lower-part of the rotor-swept area (for example, below 60 m). That is, the azimuth at which the pitch is non-optimal is known. Moreover, it is supposed that the power used to change the pitch is much less than the increase in total power produced by the turbine.

The simulations, from which the results are presented here, were performed between 2015 and the beginning of 2017. At the beginning of the work, the research question was directed to the investigation of the forest effects on wake development. For that purpose

and in this time limit, the task was simplified so that no control (as torque, tip-speed ratio or pitch) was included in the ALM. The simplification was also made because the control system of the wind turbine should not significantly affect the wake development behind the turbine. Therefore, the results of the simulations are obtained with the constant (rated) rotational rotor speed ($\Omega = 7.5$ rpm); this corresponds to the so-called "21/2" torque-control regime (see (Jonkman et al., 2009)). However, it was decided to study the effects of the forest on the power production and the angle of attack at the latest stage of the dissertation process when there was no time to run new simulations, but it was possible to further postprocess the existing simulations. This simplification is not harmful in the non-forest case because the turbine performs at the wind speed close to the rated one, although the results in the forest case can be partly spoiled by the high angular rotor speed at low wind speed. Further investigation of the forest influences on the angle of attack and power production for a more realistic turbine with a controlled tip-speed ratio, torque and pitch is planned for the near future.
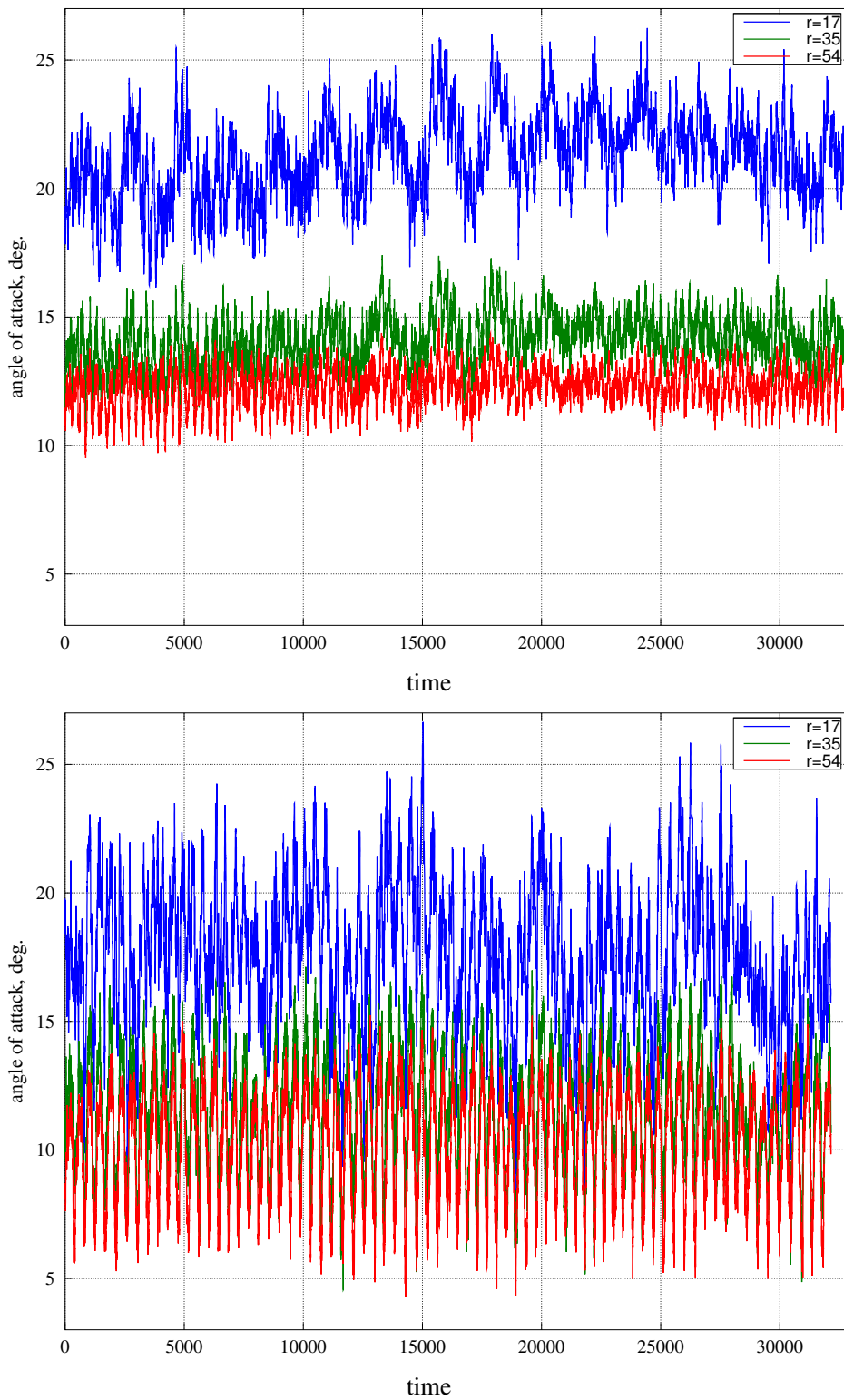
Figure 5.3.4: Time series of angle of attack of one blade at different radial coordinates for the non-forest (top) and forest (bottom) case.

Chapter 6

Summary

The main goal of the present study is to find the forest influence on wind turbines. For this purpose, several LES over a flat terrain coupled with forest and turbine models were carried out in the OpenFOAM environment (OpenCFD Ltd (ESI Group), 2004-2017) to model the flow behaviour in identical cases with and without a forest. The wind turbine is modelled by the Actuator Line Model (ALM). The depth of the Atmospheric Boundary Layer (ABL) considered in the simulations covered four rotor diameters in most of the cases. (ABL equals the height of the domain in the present study.) At first, the numerical methods, forest and turbine models are evaluated theoretically and validated using other LES studies, experimental and field measurements.

Initially, the standard ABL flow was simulated in a domain with a length of four ABL depths. However, it turned out that it is too short to prevent the "locking effect" seen as the non-physical elongated crosswind inhomogeneities (Munters et al., 2016). It is especially important to avoid the "locking effect" (non zero spatial autocorrelation Ruu_x at large r_x mainly) when the turbulence length scales are studied. According to Munters et al. (2016), the windwise autocorrelation decreases to zero when the domain length is approximately 38 ABL depths ($12\pi d$). However, 38 ABL depths ($L_x = 12\pi d$) is not yet long enough to prevent the "locking effect". Finally, Fang and Porté-Agel (2015) simulated the case in a significantly large domain, which size is $100d \times 13d \times d$ (or $32\pi d \times 4\pi d \times d$). They reported that Ruu_x drops below zero at $r_x/d = 10$ in that case. A similar achievement was obtained by Munters et al. (2016) in the case ($L_x/d = 12$, shifted) with shifted periodic conditions (introduced by Munters et al. (2016)) as well as in the present LES in the case of the long domain ($L_x/d = 12$) with the turning approach. The domain turning approach is described in Chapter 3. The present LES results with the turning approach agree very well with Munters et al. (2016). Therefore, the turning domain approach is highly recommended to use in the periodic simulations and in the precursor simulation for non-periodic simulations.

Next, the current forest-canopy model implementation is validated using the study of Shaw and Schumann (1992). The LES with two different forest canopies (one is from Nebenführ and Davidson (2014) and the other is from Shaw and Schumann (1992)) were

performed and compared with the existing field measurements (Bergström et al., 2013). In both forest canopy cases, the velocities and turbulence intensities are within the one-standard deviation intervals. This indicates the correct choice of the flow properties for both present LES. However, the profiles of the case with a lower Leaf-Area Index (LAI) better corresponds to the measurements. The Leaf-Area Density (LAD) profile for the lower LAI is adopted from Shaw and Schumann (1992). The LAD profile for the higher LAI is adopted from Nebenführ and Davidson (2014). The LAD profile from Shaw and Schumann (1992) seems to model the Swedish forest from a field near Ryningsnäs better than the LAD from Nebenführ and Davidson (2014). The present LES agrees very well with the field measurements and Nebenführ and Davidson (2014).

Further, the ALM implemented in the NREL SOWFA library (Churchfield et al., 2012a) for the OpenFOAM environment is used as a turbine model in the simulations. The ALM is validated using wind-tunnel measurements by Chamorro and Porté-Agel (2009). According to the obtained results, ALM is found to be very sensitive to the choice of the two physical parameters - the airfoil type and mounting pitch - and one numerical parameter - the smearing coefficient ε which is applied to distribute the aerodynamic forces from the virtual blade nodes to the actual finite volume cell centres. Based on the results of the present study, ε should be chosen in such a way that $\varepsilon \geq 2\Delta x$. However, ε should not be larger than half of the turbine radius (R). In the case of $D/\Delta x = 27$, the best choice for ε was observed to be $\varepsilon = 4\Delta x$ ($\varepsilon/R = 0.3$). The study by Chamorro and Porté-Agel (2009) is not suggested to be further used for validation because of the unknown airfoil type and thus the absence of airfoil data. In the present study a good agreement with this experiment is achieved with a flat-plate airfoil by decreasing the mounting pitch. The results of the present study suggest that a good agreement can also be achieved by using the cambered flat-plate or other cambered airfoil data available at a low Reynolds number.

After the validation part, the effects created by the canopy are studied:

- over flat terrain without turbines;

- in case of two turbines in tandem (2WT);

- in case of a large wind farm with six (3 × 2) wind turbines modelled and periodic conditions applied (6WT).

Results of the simulations show that the wake structure above/in the forest differs from the case without a forest. The wakes in the forest case (in both 2WT and infinite wind farm cases) are wider in the crosswind (as well as vertically) but shorter in windwise directions than wakes in the non-forest case. Taking into account these effects, the wind turbines above/in the forest can possibly be placed closer to each other than in the unforested site. It is also seen from the side view of the normalized mean windwise velocity that the wake in the case without forest is nearly symmetric in the vertical direction over the hub height. At the same time, the wake from the forest case is not symmetric (visually, as if the wake moves into the forest), which inherently means that the turbine is operating in very different wind conditions. It is also found that the shape of the wake in the infinite wind

farm case differs from the one in the 2WT case. In contrast to the 2WT cases, the velocity deficit calculated between the reference flow (the periodic flow performed in the same domain without turbines) and the wake flow does not drop to zero at $z > 2H$.

The global wind shear α in the cases with forest is approximately three to four times larger than the values obtained in the non-forest cases. α in the forest cases without wind turbines is smaller than the values obtained in the cases with turbines. The wind shear obtained in the 2WT case with forest for the upwind turbine is smaller by 10% than the one obtained for the downwind turbine. The wind shear for an infinite wind park is very similar to the one obtained for the upwind turbine in the 2WT case with forest. In general, the wind shear obtained in the forest cases agrees with the values estimated at hub height by Odemark and Segalini (2014) ($\alpha = 0.5$) and Nebenführ and Davidson (2014) ($\alpha = 0.52$). However, α obtained in the 2WT case without forest for upwind and downwind turbines are equal to each other. And the value obtained in the large wind farm (non-forest case) is much smaller (approximately zero) than it is in the 2WT case and even in the case without wind turbines and without forest. In general, the wind shear obtained in the cases without forest (with and without WTs) is slightly smaller than it was calculated by Nebenführ and Davidson (2014) in the non-forest case without wind turbines ($\alpha = 0.19$).

The maximum of turbulence intensity (in the rotor area of a virtual turbine) calculated in the cases without turbines is 11% and 23% in the non-forest and forest cases, respectively. The presence of the turbines even further increases the turbulence intensity for the forest and non-forest cases. The maximum of the vertical Reynolds shear stress (in the rotor area of a virtual turbine) calculated in the cases with forest and without turbines is seven to eight times higher than in the case without forest. However, the maximum of the vertical Reynolds shear stress calculated in the 2WT cases with forest is about ten times higher than in the case without forest. Thus, the presence of the forest increases the vertical shear stress as it is known. Moreover, the presence of the turbines itself further increases the vertical shear stress.

The maximum values of wind shear and turbulence intensity, given by international safety standards in 2005 (IEC, 2005) for the strongest turbine class, are $\alpha = 0.2$ and $I = I_u = 16\%$, respectively. The values predicted by LES in the forest case are much larger than the given safety limits. The increased turbulence and high wind shear can be harmful for the turbines which are designed according to IEC (2005). Thus, the placement of the turbines, not designed for the forest wind conditions, in a forest-covered terrain may lead to a shortened turbine life cycle.

The turbulence integral length scale Lu in the case with forest is smaller than without forest (without turbines, see Chapter 3). As the forest makes the integral length scale smaller, it is clear that for a given mean wind speed, the time scale of the dominant turbulent structures also becomes smaller. Therefore, the dominant aerodynamic loads on the blades not only increase in magnitude but also occur at higher frequencies. The ratio between the integral length scale at the lower and upper tip $Lu|_{z/H=1.6}/Lu|_{z/H=0.4}$ is

approximately 2 in the forest case. However, in the case without forest, the ratio is close to one ($Lu|_{z/H=1.6}/Lu|_{z/H=0.4}$=0.8). This indicates that the turbulence structures in the forest case are very different across the rotor disk. Therefore, the frequency of the loads also varies over the rotor area.

Hence, the much stronger mean shear, much higher turbulence intensity and the smaller turbulent length scale, which were obtained in the current study for the case with forest in comparison to the non-forest case, can be harmful to the turbine and can reduce its life cycle. Based on the results discussed above, design safety standards should be created for wind turbines to be installed on forested sites.

In both cases (2WT and 6WT), the available and produced (actual) power in the forest case is smaller than in the non-forest case because of the slightly different wind conditions over the rotor disk area in these cases ($U_h = 8$ m/s and $U_h = 8.9$ m/s, respectively). The velocity in the wakes, wind shear and turbulence intensity are slightly different in the case with two turbines in tandem and a large wind turbine array. This may be a reason why the loss of actual shaft power due to the forest is higher in the 6WT case than in the 2WT case. On the other hand, the aerodynamic power loss (in both cases, 2WT and 6WT) in the forest case is smaller and the power coefficient is larger than in the case without forest. This indicates that performance of the turbine located in the forest may be better, mainly because of the higher mean velocity through the upper half of the rotor disk owing to the strong mean wind shear.

Moreover, it was shown that the blade angle of attack varies much more in the forest case than in the non-forest case due to both the increased mean shear and the increased turbulence. Therefore, blades are likely to operate much more in off-design conditions in the forest case. A possible active pitch control is proposed in the present study to be considered by manufacturers in order to increase power production and minimize fatigue loads on turbines in forest conditions.

The next steps after this project should include the following. First of all, the pitch control should be implemented in the ALM in order to study how much the angle of attack variation in the forest case could be reduced by the pitch control. The variation can be reduced based on the blade azimuth angle. On the other hand, the control could additionally be based on turbulent velocity variations. The numerical results should be compared with field measurements from a forested site. Furthermore, the influence of forest cut should be studied in order to see how far the forest edge should be brought away from the turbine to prevent the harmful forest effects on the turbine.

Bibliography

Abedi, H. (2013). *Development of vortex filament method for aerodynamic loads on rotor blades*. Licentiate thesis. Chalmers University of Technology.

Agafonova, O., Avramenko, A., Chaudhari, A., and Hellsten, A. (2016a). The effects of the canopy created velocity inflection in the wake development. *AIP Conference Proceedings*, 1738(1): 480082. doi:http://dx.doi.org/10.1063/1.4952318, url: `http://scitation.aip.org/content/aip/proceeding/aipcp/10.1063/1.4952318`.

Agafonova, O., Avramenko, A., Chaudhari, A., and Hellsten, A. (2016b). Effects of the canopy created velocity inflection in the wake development in a large wind turbine array. *Journal of Physics: Conference Series*, 753(3), p. 032001. url: `http://stacks.iop.org/1742-6596/753/i=3/a=032001`.

Agafonova, O., et al. (2012). Experimental and Computational Study of a Flow over a Hill Covered with Forest. In: *9th International ERCOFTAC Symposium on Engineering Turbulence Modelling and Measurements (ETMM9), Thessaloniki, Greece*.

Agafonova, O. (2011). *Experimental and Computational Study of a Flow over a Hill Covered with Forest*. Master's thesis. Lappeenranta University of Technology, Finland.

Agafonova, O., et al. (2014a). Limits of WAsP modelling in comparison with CFD for wind flow over two-dimensional hills. In: *Europe's premier wind energy conference and exhibition (EWEA2014), Barcelona, Spain*.

Agafonova, O., et al. (2014b). Numerical Modelling of Wind Flow Over Hills. In: *The 18th European Conference on Mathematics for Industry (ECMI2014), Taormina, Italy*.

Allaerts, D. and Meyers, J. (2015). Large eddy simulation of a large wind-turbine array in a conventionally neutral atmospheric boundary layer. *Physics of Fluids*, 27(6): 065108. doi:http://dx.doi.org/10.1063/1.4922339, url: `http://scitation.aip.org/content/aip/journal/pof2/27/6/10.1063/1.4922339`.

Allen, Jr., L.H. (1968). Turbulence and Wind Speed Spectra within a Japanese Larch Plantation. *Journal of Applied Meteorology*, 7, pp. 73–78. doi:10.1175/1520-0450(1968) 007⟨0073:TAWSSW⟩2.0.CO;2.

Baba-Ahmadi, M. and Tabor, G. (2009). Inlet conditions for {LES} using mapping and feedback control. *"Computers and Fluids "*, 38(6), pp. 1299 – 1311. ISSN 0045-7930, doi:https://doi.org/10.1016/j.compfluid.2009.02.001, url: `http://www.sciencedirect.com/science/article/pii/S004579300900022X`.

Bailey, B. and Stoll, R. (2013). Turbulence in Sparse, Organized Vegetative Canopies: A Large-Eddy Simulation Study. *Boundary-Layer Meteorology*, 147(3), pp. 369–400. doi:10.1007/s10546-012-9796-4.

Baldocchi, D.D. and Meyers, T.P. (1988). Turbulence structure in a deciduous forest. *Boundary-Layer Meteorology*, 43(4), pp. 345–364. ISSN 1573-1472, doi:10.1007/BF00121712, url: `http://dx.doi.org/10.1007/BF00121712`.

Barlas, E., Buckingham, S., and van Beeck, J. (2016). Roughness Effects on Wind-Turbine Wake Dynamics in a Boundary-Layer Wind Tunnel. *Boundary-Layer Meteorology*, 158(1), pp. 27–42. ISSN 0006-8314, doi:10.1007/s10546-015-0083-z.

Bergström, H., et al. (2013). *Wind power in forests: Winds and effects on loads. Elforsk. (Elforsk rapport; No. 13:09)*. Technical report.

Brunet, Y., Finnigan, J.J., and Raupach, M.R. (1994). A wind tunnel study of air flow in waving wheat: Single-point velocity statistics. *Boundary-Layer Meteorology*, 70(1), pp. 95–132. ISSN 1573-1472, doi:10.1007/BF00712525, url: `http://dx.doi.org/10.1007/BF00712525`.

Calaf, M., Meneveau, C., and Meyers, J. (2010). Large eddy simulations of fully developed wind-turbine array boundary layers. *Phys. Fluids*, 22.

Chamorro, L.P. and Porté-Agel, F. (2010). Effects of Thermal Stability and Incoming Boundary-Layer Flow Characteristics on Wind-Turbine Wakes: A Wind-Tunnel Study. *Boundary-Layer Meteorology*, 136(3), pp. 515–533. ISSN 1573-1472, doi:10.1007/s10546-010-9512-1, url: `http://dx.doi.org/10.1007/s10546-010-9512-1`.

Chamorro, L.P. and Porté-Agel, F. (2011). Turbulent Flow Inside and Above a Wind Farm: A Wind-Tunnel Study. *Energies*, 4(11), p. 1916. ISSN 1996-1073, doi:10.3390/en4111916, url: `http://www.mdpi.com/1996-1073/4/11/1916`.

Chamorro, L. and Porté-Agel, F. (2009). A wind-tunnel investigation of wind-turbine wakes: boundary-layer turbulence effects. *Boundary-layer meteorology*, 132, pp. 129–149.

Chaudhari, A. (2014). *Large-eddy simulation of wind flows over complex terrains for wind energy applications*. Ph.D. thesis. Lappeenranta University of Technology.

Chaudhari, A., et al. (2014a). Large eddy simulation of atmospheric flows over the Bolund hill. In: *6th International Symposium on Computational Wind Engineering (CWE2014), Hamburg, Germany*.

Chaudhari, A., et al. (2014b). Large-eddy simulations for atmospheric boundary layer flows over complex terrains with applications in wind energy. In: *Proceedings of the 11th World Congress on Computational Mechanics (WCCM XI), Barcelona, Spain*, pp. 5205–5216.

Churchfield, M.J., Lee, S., and Moriarty, P.J. (2012a). *Overview of the Simulator fOr Wind Farm Application (SOWFA)*. Technical report. Also available at `http://nwtc.nrel.gov/SOWFA`.

Churchfield, M.J., et al. (2012b). A Large-Eddy Simulation of Wind-Plant Aerodynamics. In: *The 50th AIAA Aerospace Sciences Meeting Nashville, Tennessee*.

Churchfield, M.J., Lee, S., Michalakes, J., and Moriarty, P.J. (2012c). A numerical study of the effects of atmospheric and wake turbulence on wind turbine dynamics. *Journal of Turbulence*, 13, p. N14. doi:10.1080/14685248.2012.668191, url: `http://dx.doi.org/10.1080/14685248.2012.668191`.

Cionco, R. (1979). A summary of an analysis of canopy flow coupling for a variety of canopy types. In: *14th Conference on Agricultural and Forest Meteorology and 4th Conference of Biometeorology, Minneapolis, MN, Amer. Meteo. Soc., Boston, MA. Google Scholar*.

Counihan, J. (1975). Adiabatic atmospheric boundary layers, A review and analysis of data from the period 1880-1970. *Atmos. Envir.* doi:10.1016/0004-6981(75)90088-8.

Dupont, S. and Brunet, Y. (2008a). Impact of forest edge shape on tree stability: a large-eddy simulation study. *Forestry*, 81, pp. 299–315.

Dupont, S. and Brunet, Y. (2009). Coherent structures in canopy edge flow: a large-eddy simulation study. 630, pp. 93–128. doi:10.1017/S0022112009006739.

Dupont, S. and Brunet, Y. (2008b). Edge Flow and Canopy Structure: A Large-Eddy Simulation Study. *Boundary-Layer Meteorology*, 126(1), pp. 51–71. ISSN 1573-1472, doi:10.1007/s10546-007-9216-3, url: `http://dx.doi.org/10.1007/s10546-007-9216-3`.

Dupont, S. and Patton, E.G. (2012). Influence of stability and seasonal canopy changes on micrometeorology within and above an orchard canopy: The {CHATS} experiment. *Agricultural and Forest Meteorology*, 157, pp. 11 – 29. ISSN 0168-1923, doi:http://dx.doi.org/10.1016/j.agrformet.2012.01.011, url: `http://www.sciencedirect.com/science/article/pii/S016819231200041X`.

Fang, J. and Porté-Agel, F. (2015). Large-Eddy Simulation of Very-Large-Scale Motions in the Neutrally Stratified Atmospheric Boundary Layer. *Boundary-Layer Meteorology*, 155, pp. 397–416. doi:10.1007/s10546-015-0006-z.

Finnigan, J.J. (1979). Turbulence in waving wheat. *Boundary-Layer Meteorology*, 16(2), pp. 213–236. ISSN 1573-1472, doi:10.1007/BF02350512, url: `http://dx.doi.org/10.1007/BF02350512`.

Finnish Energy Report (2016). *Energy Year 2015. Electricity Report*. Technical report. Finnish Energy.

Froude, W. (1878). On the Elementary Relation between Pitch, Slip and Propulsive Efficiency. 19, pp. 22–33.

Germano, M., Piomelli, U., Moin, P., and Cabot, W. (1991). A dynamic subgrid-scale eddy viscosity model. *Physics of Fluids A: Fluid Dynamics*, 3(7), pp. 1760–1765. doi: 10.1063/1.857955, url: `http://dx.doi.org/10.1063/1.857955`.

IEC (2005). *IEC 61400-1 Wind Turbines Part1: Design Requirements*. Technical report. Geneva: International Electrotechnical Commission.

Issa, R. (1986). Solution of the implicitly discretised fluid flow equations by operator-splitting. *Journal of Computational Physics*, 62(1), pp. 40 – 65. ISSN 0021-9991, doi:http://dx.doi.org/10.1016/0021-9991(86)90099-9, url: `http://www.sciencedirect.com/science/article/pii/0021999186900999`.

Jin, W. (2013). *Numerical Simulation of Wind Turbine Wakes based on Actuator Line Method in NEK5000*. Master's thesis. Royal Institute of Technology, Sweden.

Jonkman, J., Butterfield, S., Musial, W., and Scott, G. (2009). *Definition of a 5 MW Reference Wind Turbine for Offshore System Development*. Technical report. NREL, USA.

Kaimal, J. and Finnigan, J. (1994). Atmospheric boundary layer flows:their structure and measurement. *Oxford University press*, p. 289.

Kanda, M. and Hino, M. (1994). Organized structures in developing turbulent flow within and above a plant canopy, using a Large Eddy Simulation. *Boundary-Layer Meteorology*, 68(3), pp. 237–257. ISSN 1573-1472, doi:10.1007/BF00705599, url: `http://dx.doi.org/10.1007/BF00705599`.

Kim, B., Kim, W., Park, J., and Kim, M. (2011). Aerodynamic design and performance analysis of multi-MW class wind turbine blade. *Journal of Mechanical Science and Technology*, 25(8), pp. 1995–2002.

Lalic, B. and Mihailovic, D.T. (2004). An Empirical Relation Describing Leaf-Area Density inside the Forest for Environmental Modeling. *Journal of Applied Meteorology*, 43(4), pp. 641–645. doi:10.1175/1520-0450(2004)043⟨0641:AERDLD⟩2.0. CO;2, url: `http://dx.doi.org/10.1175/1520-0450(2004)043<0641:AERDLD>2.0.CO;2`.

Launiainen, S., et al. (2007). Vertical variability and effect of stability on turbulence characteristics down to the floor of a pine forest. *Tellus B*, 59(5), pp. 919–936. ISSN 1600-0889, doi:10.1111/j.1600-0889.2007.00313.x, url: `http://dx.doi.org/10.1111/j.1600-0889.2007.00313.x`.

Martinez-Tossas, L., Churchfield, M., and Meneveau, C. (2015). Large Eddy Simulation of wind turbine wakes: detailed comparisons of two codes focusing on effects of numerics and subgrid modeling. *Journal of Physics: Conference Series*, 625(1), p. 012024. url: `http://stacks.iop.org/1742-6596/625/i=1/a=012024`.

Ministry of Foreign Affairs of Denmark (2014). *Finland: Wind Energy. Sector Analysis*. Technical report. Ministry of Foreign Affairs of Denmark.

Monin, A. and Obukhov, A. (1954). Basic laws of turbulence mixing in the surface layer of the atmosphere. *Tr. Geofiz. Inst., Akad. Nauk SSSR*, 24, pp. 163–187.

Müller, D. and Davidson, L. (2000). Comparison of different subgrid turbulence models and boundary conditions for large-eddy-simulations of room air flows. In: *7TH INTERNATIONAL CONFERENCE ON AIR DISTRIBUTION IN ROOMS, ROOMVENT*, pp. 301–306.

Munters, W., Meneveau, C., and Meyers, J. (2016). Shifted periodic boundary conditions for simulations of wall-bounded turbulent flows. *Physics of Fluids*, 28(2): 025112. doi: 10.1063/1.4941912.

Nebenführ, B. and Davidson, L. (2014). Influence of a forest canopy on the neutral atmospheric boudary layer - A LES study. In: *ETMM10: 10th International ERCOFTAC Symposium on Turbulence Modelling and Measurements*.

Nilsen, K.M. (2014). *Numerical and experimental investigation of turbulence and transport in mixing geometries*. Ph.D. thesis. Iowa State University.

Odemark, Y. and Segalini, A. (2014). The effects of a model forest canopy on the outputs of a wind turbine model. *Journal of Physics, Conference Series*, 555(1). Updated from manuscript to article in journal.QC 20150213.

OpenCFD Ltd (ESI Group) (2004-2017). *OpenFOAM The open source CFD toolbox*. url: `http://www.openfoam.com/`. [Online; accessed 18-January-2017].

Panjwani, B., et al. (2014). OffWindSolver: Wind farm design tool based on actuator line/actuator disk concept in OpenFoam architecture. *ITM Web of Conferences*, 2, p. 04001. doi:10.1051/itmconf/20140204001, url: `https://doi.org/10.1051/itmconf/20140204001`.

Patton, E. (1991). *Large-Eddy Simulation of Turbulent Flow Above and Withina Plant Canopy*. Ph.D. thesis. University of California Davis.

Perfilev, D. (2013). *Methodology for wind turbine blade geometry optimization*. Ph.D. thesis. Lappeenranta University of Technology.

Perfilev, D., Kosmacheva, A., Backman, J., and Hämäläinen, J. (2013). Semi Automated Improvement of Wind Blade Design. In: *10th European Conference on Turbomachinery Fluid dynamics and Thermodynamics ETC10, Lappeenranta, Finland.*

Porté-Agel, F., Wu, Y.T., Lu, H., and Conzemius, R.J. (2011). Large-eddy simulation of atmospheric boundary layer flow through wind turbines and wind farms. *Journal of Wind Engineering and Industrial Aerodynamics*, 99(4), pp. 154 – 168. ISSN 0167-6105, doi:http://dx.doi.org/10.1016/j.jweia.2011.01.011, url: `http://www.sciencedirect.com/science/article/pii/S0167610511000134`. The Fifth International Symposium on Computational Wind Engineering.

Raupach, M.R., Coppin, P.A., and Legg, B.J. (1986). Experiments on scalar dispersion within a model plant canopy part I: The turbulence structure. *Boundary-Layer Meteorology*, 35(1), pp. 21–52. ISSN 1573-1472, doi:10.1007/BF00117300, url: `http://dx.doi.org/10.1007/BF00117300`.

Schlegel, F., et al. (2012). Large-Eddy Simulation of Inhomogeneous Canopy Flows Using High Resolution Terrestrial Laser Scanning Data. *Boundary-Layer Meteorology*, 142(2), pp. 223–243. ISSN 1573-1472, doi:10.1007/s10546-011-9678-1, url: `http://dx.doi.org/10.1007/s10546-011-9678-1`.

Schröttle, J., et al. (2016). Wind turbine wakes in forest and neutral plane wall boundary layer large-eddy simulations. *Journal of Physics: Conference Series*, 753: 032058. doi:http://dx.doi.org/10.1088/1742-6596/753/3/032058.

Shaw, R.H., Brunet, Y., Finnigan, J.J., and Raupach, M.R. (1995). A wind tunnel study of air flow in waving wheat: Two-point velocity statistics. *Boundary-Layer Meteorology*, 76(4), pp. 349–376. ISSN 1573-1472, doi:10.1007/BF00709238, url: `http://dx.doi.org/10.1007/BF00709238`.

Shaw, R., Den Hartog, G., and Neumann, H. (1988). Influence of foliar density and thermal stability on profiles of Reynolds stress and turbulence intensity in a deciduous forest. *Boundary-Layer Meteorology*, 45(4), pp. 391–409. ISSN 1573-1472, doi:10.1007/BF00124010, url: `http://dx.doi.org/10.1007/BF00124010`.

Shaw, R.H. and Patton, E.G. (2003). Canopy element influences on resolved and subgrid-scale energy within a large-eddy simulation. *AGRICULTURAL AND FOREST METEOROLOGY*, 115(1-2), pp. 5–17.

Shaw, R.H. and Schumann, U. (1992). Large-eddy simulation of turbulent flow above and within a forest. *Boundary-Layer Meteorology*, 61(1-2), pp. 47–64.

Sheldahl, R. and Klimas, P. (1981). *Aerodynamic Characteristics of Seven Symmetrical Airfoil Sections Through 180-Degree Angle of Attack for Use in Aerodynamic Analysis of Vertical Axis Wind Turbines*. Technical report. Sandia National Laboratories.

Smagorinsky, J. (1963). General circulation experiments with the primitive equations, I. The basic experiment. *Monthly Weather Review*, 91(3), pp. 99–164.

Sørensen, J.N. and Kock, C.W. (1995). A model for unsteady rotor aerodynamics. *Journal of Wind Engineering and Industrial Aerodynamics*, 58(3), pp. 259 – 275. ISSN 0167-6105, doi:http://dx.doi.org/10.1016/0167-6105(95)00027-5, url: `http://www.sciencedirect.com/science/article/pii/0167610595000275`.

Sørensen, J.N. and Shen, W.Z. (2002). Numerical modeling of wind turbine wakes. *Journal of fluids engineering*, 124(2), pp. 393–399.

Sunada, S., Sakaguchi, A., and Kawachi, K. (1997). Airfoil Section Characteristics at a Low Reynolds Number. *Journal of Fluids Engineering*, 119(1), pp. 129–135. doi: 10.1115/1.2819098[doi], url: `http://dx.doi.org/10.1115/1.2819098`.

Svenning, E. (2010). *Implementation of an actuator disk in OpenFOAM*. Technical report. Chalmers University of Technology.

Troldborg, N., Sørensen, J.N., and Mikkelsen, R. (2007). Actuator line simulation of wake of wind turbine operating in turbulent inflow. In: *Journal of physics: conference series*, vol. 75, 1, p. 012063.

Troldborg, N., Sørensen, J.N., and Mikkelsen, R. (2008). *Actuator line modeling of wind turbine wakes*. Ph.D. thesis. Technical University of Denmark, Department of Energy Engineering.

Vermeer, L., Sørensen, J., and Crespo, A. (2003). Wind turbine wake aerodynamics. *Progress in Aerospace Sciences*, 39(6-7), pp. 467 – 510. ISSN 0376-0421, doi:http://dx.doi.org/10.1016/S0376-0421(03)00078-2, url: `http://www.sciencedirect.com/science/article/pii/S0376042103000782`.

de Villiers, E. (2006). *The Potential of Large Eddy Simulation for the Modeling of Wall Bounded Flows*. Ph.D. thesis. Imperial College of Science, Technology and Medicine.

Vuorinen, V., Keskinen, J.P., Duwig, C., and Boersma, B. (2014). On the implementation of low-dissipative Runge-Kutta projection methods for time dependent flows using OpenFOAM. *Computational Fluids*, 93, pp. 153–163.

Vuorinen, V., et al. (2012). A low-dissipative, scale-selective discretization scheme for the Navier-Stokes equations. *Computational Fluids*, 70, pp. 195–205.

Wilcox, D. (2006). *Turbulence Modeling for CFD. Third edition*. DCW Industries, Incorporated. ISBN 978-1-928729-08-2.

Witha, B., Steinfeld, G., Dörenkämper, M., and Heinemann, D. (2014). Large-eddy simu-
lation of multiple wakes in offshore wind farms. *Journal of Physics: Conference Series*,
555(1), p. 012108. url: `http://stacks.iop.org/1742-6596/555/i=1/a=`
`012108`.

Wu, Y.T. and Porté-Agel, F. (2011). Large-Eddy Simulation of Wind-Turbine Wakes:
Evaluation of Turbine Parametrisations. *Boundary-Layer Meteorology*, 138(3), pp.
345–366. ISSN 1573-1472, doi:10.1007/s10546-010-9569-x, url: `http://dx.`
`doi.org/10.1007/s10546-010-9569-x`.

Wu, Y.T. and Porté-Agel, F. (2012). Atmospheric Turbulence Effects on Wind-Turbine
Wakes: An LES Study. *Energies*, 5(12), p. 5340. ISSN 1996-1073, doi:10.3390/
en5125340, url: `http://www.mdpi.com/1996-1073/5/12/5340`.

Wu, Y.T. and Porté-Agel, F. (2013). Simulation of Turbulent Flow Inside and Above Wind
Farms: Model Validation and Layout Effects. *Boundary-Layer Meteorology*, 146(2),
pp. 181–205. ISSN 1573-1472, doi:10.1007/s10546-012-9757-y, url: `http://dx.`
`doi.org/10.1007/s10546-012-9757-y`.

Yang, X., et al. (2014). Large-eddy simulation of turbulent flow past wind turbines/farms:
the Virtual Wind Simulator (VWiS). *Wind Energy*.

Yoshizawa, A. (1985). A statistically-derived subgrid-scale kinetic energy model for the
large-eddy simulation of turbulent flows. *Journal of the Physical Society of Japan*,
54(8), pp. 2834–2839.

ACTA UNIVERSITATIS LAPPEENRANTAENSIS

719. OVASKA, SAMI-SEPPO. Oil and grease barrier properties of converted dispersion-coated paperboards. 2016. Diss.

720. MAROCHKIN, VLADISLAV. Novel solutions for improving solid-state photon detector performance and manufacturing. 2016. Diss.

721. SERMYAGINA, EKATERINA. Modelling of torrefaction and hydrothermal carbonization and heat integration of torrefaction with a CHP plant. 2016. Diss.

722. KOTISALO, KAISA. Assessment of process safety performance in Seveso establishments. 2016. Diss.

723. LAINE, IGOR. Institution-based view of entrepreneurial internationalization. 2016. Diss.

724. MONTECINOS, WERNER EDUARDO JARA. Axial flux permanent magnet machines – development of optimal design strategies. 2016. Diss.

725. MULTAHARJU, SIRPA. Managing sustainability-related risks in supply chains. 2016. Diss.

726. HANNONEN, JANNE. Application of an embedded control system for aging detection of power converter components. 2016. Diss.

727. PARKKILA, JANNE. Connecting video games as a solution for the growing video game markets. 2016. Diss.

728. RINKINEN, SATU. Clusters, innovation systems and ecosystems: Studies on innovation policy's concept evolution and approaches for regional renewal. 2016. Diss.

729. VANADZINA, EVGENIA. Capacity market in Russia: addressing the energy trilemma. 2016. Diss.

730. KUOKKANEN, ANNA. Understanding complex system change for a sustainable food system. 2016. Diss.

731. SAVOLAINEN, JYRKI. Analyzing the profitability of metal mining investments with system dynamic modeling and real option analysis. 2016. Diss.

732. LAMPINEN, MATTI. Development of hydrometallurgical reactor leaching for recovery of zinc and gold. 2016. Diss.

733. SUHOLA, TIMO. Asiakaslähtöisyys ja monialainen yhteistyö oppilashuollossa: oppilashuoltoprosessi systeemisenä palvelukokonaisuutena. 2017. Diss.

734. SPODNIAK, PETR. Long-term transmission rights in the Nordic electricity markets: An empirical appraisal of transmission risk management and hedging. 2017. Diss.

735. MONTONEN, JUHO. Integrated hub gear motor for heavy-duty off-road working machines – Interdisciplinary design. 2017. Diss.

736. ALMANASRAH, MOHAMMAD. Hot water extraction and membrane filtration processes in fractionation and recovery of value-added compounds from wood and plant residues. 2017. Diss.

737. TOIVANEN, JENNI. Systematic complaint data analysis in a supply chain network context to recognise the quality targets of welding production. 2017. Diss.

738. PATEL, GITESHKUMAR. Computational fluid dynamics analysis of steam condensation in nuclear power plant applications. 2017. Diss.

739. MATTHEWS, SAMI. Novel process development in post-forming of an extruded wood plastic composite sheet. 2017. Diss.

740. KÄHKÖNEN, TOMMI. Understanding and managing enterprise systems integration. 2017. Diss.

741. YLI-HUUMO, JESSE. The role of technical dept in software development. 2017. Diss.

742. LAYUS, PAVEL. Usability of the submerged arc welding (SAW) process for thick high strength steel plates for Arctic shipbuilding applications. 2017. Diss.

743. KHAN, RAKHSHANDA. The contribution of socially driven businesses and innovations to social sustainability. 2017. Diss.

744. BIBOV, ALEKSANDER. Low-memory filtering for large-scale data assimilation. 2017. Diss.

745. ROTICH, NICOLUS KIBET. Development and application of coupled discrete and continuum models in solid particles classification. 2017. Diss.

746. GAST, JOHANNA. The coopetition-innovation nexus: Investigating the role of coopetition for innovation in SMEs. 2017. Diss.

747. KAPOOR, RAHUL. Competition and disputes in the patent life cycle. 2017. Diss.

748. ALI-MARTTILA, MAAREN. Towards successful maintenance service networks – capturing different value creation strategies. 2017. Diss.

749. KASHANI, HAMED TASALLOTI. On dissimilar welding: a new approach for enhanced decision-making. 2017. Diss.

750. MVOLA BELINGA, ERIC MARTIAL. Effects of adaptive GMAW processes: performance and dissimilar weld quality. 2017. Diss.

751. KARTTUNEN, JUSSI. Current harmonic compensation in dual three-phase permanent magnet synchronous machines. 2017. Diss.

752. SHI, SHANSHUANG. Development of the EAST articulated maintenance arm and an algorithm study of deflection prediction and error compensation. 2017. Diss.

753. CHEN, JIE. Institutions, social entrepreneurship, and internationalization. 2017. Diss.

754. HUOTARI, PONTUS. Strategic interaction in platform-based markets: An agent-based simulation approach. 2017. Diss.

755. QU, BIN. Water chemistry and greenhouse gases emissions in the rivers of the "Third Pole" / Water Tower of Asia". 2017. Diss.

756. KARHU, PÄIVI. Cognitive ambidexterity: Examination of the cognitive dimension in decision-making dualities. 2017. Diss.